Universidade de São Paulo
Instituto de Astronomia, Geofísica e Ciências Atmosféricas
Departamento de Ciências Atmosféricas

João Augusto Hackerott

Momentum fluxes in the Marine Atmospheric Surface Layer: a study on the Southwestern Atlantic Ocean

"Fluxos de momentum na Camada Limite Superficial Atmosférica Marítima: um estudo para o Oceano Atlântico Sudoeste"

São Paulo
2018

João Augusto Hackerott

Momentum fluxes in the Marine Atmospheric Surface Layer: a study on the Southwestern Atlantic Ocean

"Fluxos de momentum na Camada Limite Superficial Atmosférica Marítima: um estudo para o Oceano Atlântico Sudoeste"

Thesis submitted in partial fulfillment of the requirements for the degree of Doctor of Sciences in the Institute of Astronomy, Geophysics and Atmospheric Sciences

Major field: Meteorology
Advisor: Prof. Dr. Ricardo Camargo
Co-advisor: Prof. Dr. Luciano P. Pezzi

Versão Corrigida. O original encontra-se disponível na Unidade

São Paulo
2018

To Vivian Maria, Maria Mercedes, Fernando Ricardo,
José Afonso and Maria Altimira

Acknowledgements

I would like to first offer profound thanks to my advisors, Prof. Dr. Ricardo Camargo and Prof. Dr. Luciano Ponzi Pezzi, for their continuous support of my Ph.D study, motivating guidance, endless patience, advice and friendship. It has been almost five years working together and during this period I have improved my skills as a scientist having you two as great examples to follow.

My sincere thanks also goes to Prof. Dr. Joachen Reuder for welcoming and supervising me at Univeritetet i Bergen, in Norway. It was not only your support and advices but also the way you taught me how to do science.

I also would like to express my gratitude to Prof. Dr. Amauri Pereira de Oliveira. Without your precious support and teaching about boundary-layer meteorology, it would not be possible to conduct this research.

I would like to thank Prof. Dr. Otávio Costa Acevedo, Prof. Dr. Haroldo Fraga de Campos Velho, Prof. Dr. Maria Assunção Faus da Silva Dias, Prof. Dr. Joachen Reuder, and Prof. Dr. Ricardo Camargo for the productive conversation and helpful feedback during my defense which will undoubtedly help me in my future research in this field.

In particular, I also thank my friend and co-author in the two papers that have been submitted so far from this research, Dr. Mostafa Bakhoday Paskyabi. You are a brilliant scientist. You say you are very tough, but it makes you special and I am very grateful for your enormous attention and support.

I wish to also particularly acknowledge Dr. Michel dos Santos Mesquita. Because of you I was introduced to Prof. Dr. Joachen Reuder, which resulted in my stay in Norway. As a co-author in the first publication of this thesis, you helped a lot with deep discussions. As a friend, you introduced me to the advanced world of the WRF modeling.

My special thanks are also extended to Prof. Dr. Ronald Buss de Souza, Prof. Dr. Edson Pereira Marques Filho and Stephan Kral, who helped me with co-authorship and discussions in publications derived from this work.

I also thank the researchers from NCAR Dr. Jimy Dudhia, Dr. Wei Wang, Dr. Cindy Bruyere, Dr. David Gill and Dr. Michael Duda for the great help with the WRF model.

As a PhD student in three institutions, at Geofysisk Institutt (GFI-UiB), Instituto de Astronomia, Geofísica e Ciências Atmosféricas (IAG-USP) and Laboratório de Estudos de Oceano e da Atmosfera (LOA-INPE), I have been surrounded by great collegues, for whom I wish to highlight:

Natália Pillar, Carolina Gramcianinov, Leonardo Domingues, Francisco Vasconcelos Júnior, Júlio Moraes, Pamela Dominutti, Sameh Abou Rafee, Luis Mendes, Jorge Santana, Angel Vela, Tailine Santos , Rubinei Machado, Cristiano Prestrelo, Mercel Santos, Glauber Camponogara, Tássio Costa, Renato Braghiere, Gustavo Beneduzi, Emilia Brasilio, Fabíola Souza, Thiago Degola from IAG-USP.

Omar El Guernaoui, Yongbiao Weng, Lusha Yu, Lucas Höppler, Susana Reuder, Line Baserud, Valerie Kumer and Ólafur Rögnvaldsson from GFI-UiB.

Marcelo Santini, Regiane Moura, Leilane Gonçalves, Ueslei Sutil, Daniela Faggiani Dias and Luís Mendonça from LOA-INPE.

The staff of these three institutions also deserve my profound thanks. I highlight the great support related to computer issues by Djalma, Sebastião and Samuel, related to department bureaucracy and procedures by Elisabete, Ana and Sônia, Maisa, Marcel and Thiago, and related to library consulting by Sandra and Célia.

I'm also grateful for all professors from the IAG-USP, with whom I have been learning since March 2007, especially for Dr. Rita Ynoue, Dr. Ricardo Hallak and Dr. Amauri Oliveira, who participated in the qualification exam of this PhD.

Finally, I would like to thank my family: my parents Ceda and Ricki, my brother Zé, my sister Mi, and my dear lovely lady Vivi, for supporting me throughout this work and my life in general, always encouraging me to achieve my goals.

Last but, not the least, I thanks for all those who I have failed to mention but supported me during my PhD.

This thesis is a result of larger project that have been funded by many institutions and

supporting programs listed as follows:

The PhD project was funded by the Comissão de Paerfeiçoamento de Pessoal do Nível Superior (CAPES) and the Conselho Nacional de Desenvolvimento Científico e Tecnológico (CNPq).

The scholarship for the student exchange program at the University of Bergen was awarded by the International Cooperation Program CAPES/COFECUB, financed by CAPES - Brazilian Federal Agency for Support and Evaluation of Graduate Education within the Ministry of Education of Brazil.

The BLLAST field experiment was made possible thanks to the contribution of several institutions and funding sources: INSU-CNRS (Institut National des Sciences de l'Univers, Centre national de la Recherche Scientifique, LEFE-IDAO program), Météo-France, Observatoire Midi-Pyrénées (University of Toulouse), EUFAR (EUropean Facility for Airborne Research) and COST ES0802 (European Cooperation in Science and Technology).

The INTERCONF cruises have made possible thanks to the Brazilian Ministry of Science, Technology, Innovation and Communication (MCTIC). I thank the financial support of the Brazilian funding agencies CNPq to project ACEx (558108/2009â1). This is also a contribution to projects Advanced Studies in Medium and High Latitudes Oceanography (CAPES 23038.004304/ 2014-28) and National Institute of Science and Technology of the Cryosphere, from where the INTERCONF is funded (CNPq/PROANTAR 704222/2009).

"*Se perder o leme nunca perca o rumo.*"

Fritz Herman Sheidt

"*Nenhum vento sopra a favor de quem não sabe pra onde ir.*"

Sêneca

Resumo

Nesta tese são apresentados os resultados do estudo dos processos turbulentos que modulam os fluxos de momentum na Camada Limite Superficial Atmosférica Marítima. A análise se dá no âmbito da teoria da similaridade de Monin-Obukhov e da lei do espectro de Kolmogorov, que são aplicadas para avaliar os diferentes termos da equação do balanço de energia cinética turbulenta. O conjunto de dados inclui 187 segmentos de temperatura e velocidade do vento amostrados em alta frequência, cuidadosamente selecionados e corrigidos com respeito ao balanço do navio, coletados durante o projeto Interação Oceano-Atmosfera na Região da Confluência Brasil-Malvinas, que foi realizado no Oceano Atlântico sudoeste em outubro de 2013, 2014 e 2015. Os resultados mostraram que o fluxo de momentum é significativamente modulado pela rugosidade do mar. O conjunto de dados indicou a ocorrência de transporte ascendente de energia cinética turbulenta, principalmente durante condições estáveis, embora seus padrões gerais de transporte e dissipação foram semelhantes às observações feitas em terra firme. Também foi encontrado um comportamento particular do coeficiente de arrasto, com uma tendência negativa da velocidade do vento de calma até 10 m s^{-1} durante condições com alturas de onda inferiores a 2,5 m, e contínua diminuição do coeficiente de arrasto com o aumento da velocidade do vento para altura significativa das ondas superiores a 2,5 m. Este fenômeno foi explicado pela influência do swell, que faz com que as ondas ajam como elementos de rugosidade, induzindo um deslocamento do plano zero na ordem de 0,1 a 1 m e sugerindo a presença de uma camada de rugosidade induzida pelas ondas. Além disso, simulações numéricas utilizando modelos regionais foram realizadas, com resultados indicando a inabilidade de simularem satisfatoriamente a influência do arrasto nos fluxos de momentum, subestimando a velocidade de fricção e, consequentemente, superestimando o vento próximo da superfície

em condições com ondas altas.

Palavras-chave: Confluência Brasil–Malvinas, Camada Limite Superficial Marítima, Camada de rugosidade induzida pelas ondas, Coeficiente de arrasto, Energia cinética tubulenta.

Abstract

This thesis presents the results of the study about the turbulent processes that modulate the momentum fluxes within the Marine Atmospheric Surface Layer, on the Southwestern Atlantic Ocean. The analysis occurs in the framework of the Monin-Obukhov similarity theory and Kolmogorov's spectral law, which are applied to evaluate the different terms of the turbulent kinetic energy budget equation. The dataset includes 187 high-frequency-sampled segments of air temperature and wind velocity, which are carefully selected and corrected for ship motion, and have been collected during the Air-Sea Interaction at Brazil–Malvinas Confluence project, which was conducted in the Southwestern Atlantic Ocean in October 2013, 2014, and 2015. The results showed that the momentum flux is significantly modulated by the sea roughness. The dataset indicated the occurrence of upward transport of turbulent kinetic energy, during mainly stable conditions, although its general patterns of transport and dissipation were similar to observations taken over land surfaces. A particular behavior of the drag coefficient was detected, with a negative trend for calm wind speeds up to 10 m s^{-1} during conditions with wave heights less then 2.5 m, and the continuous decrease of the drag coefficient with increasing wind speed for significant wave heights above 2.5 m. This phenomenon was explained by the swell influence, which makes the waves act as roughness elements, inducing a zero-plane displacement in the order of 0.1 to 1 m and suggesting the presence of a wave-induced roughness layer. In addition, numerical simulations using regional models were performed, with results indicating the inability to satisfactorily simulate the influence of drag on the momentum fluxes, underestimating the friction velocity and, consequently, overestimating the near-surface wind speed during high-wave conditions.

Keywords: Brazil–Malvinas Confluence, Marine Atmospheric Surface Layer, Wave-

induced roughness layer, Drag coefficient, Turbulent kinetic energy.

List of Figures

List of Tables

List of Abbreviations and Symbols

BLLAST	Boundary Layer Late Afternoon and Sunset Turbulence
BMC	Brazil–Malvinas Confluence
CFSv2	Climate Forecast System version 2
DNS	Direct numerical simulation
IMU	Inertial motion unit
INTERCONF	Air-Sea Interaction at Brazil-Malvinas Confluence
LES	Large-eddy simulation
MASL	Marine atmospheric surface layer
NCEP	National Centers for Environmental Prediction
PBL	Planetary boundary layer
RANS	Reynolds-averaged Navier-Stokes equations
SST	Sea-surface temperature
TKE	Turbulent kinetic energy
WRF	Weather, Research and Forecasting model

α	Kolmogorov constant
α_c	Charnock constant
β	Obukhov-Corrsin constant

χ_*	Scalar characteristic scale
ϵ_x	Absolute value of the error of variable x
ϵ	Dissipation rate of turbulent kinetic energy
η	Terrain-following hydrostatic-pressure vertical coordinate
κ	von Kármán constant
ν	Kinematic viscosity of air
$\mathbf{\Omega}$	Angular velocity vector
Φ^D	Non-dimensional dissipation
Φ^P	Non-dimensional production
Φ^T	Non-dimensional transport
Φ	Roll angle
π	Pi number $\pi = 3.14159...$
ψ^P	Integrated stability function
Ψ	Yaw angle
ρ	Air density
σ	Standard deviation
τ	Momentum flux
θ	Virtual potential temperature
Θ	Pitch angle
ζ	Stability parameter
C_D	Drag coefficient
C_p	Specific heat of dry air at constant pressure
c_p	Phase speed at primary wave mean period
c	Specific CO_2 content

d	Displacement length
e	Nepierian number $e = 2.7181...$
e	Turbulent kinetic energy
g	Gravity acceleration
$\mathscr{H}$	Spacial energy spectrum
H	Sensible heat flux
Hs	Significant height of combined wind waves and swell
I	Frequency interval
k	Wavenumber
L	Monin-Obukhov length
LE	Latent heat flux
L_e	Latent heat of vaporization
n_*	Block-centred frequency
N_χ	Dissipation rate of scalar variance
n	Time frequency
p	Atmospheric pressure
Pr	Turbulent Prandtl number
q	Specific humidity
$\mathbf{r}$	Position vector
R^2	Correlation coefficient
Re_*	Roughness Reynolds number
$RMSE$	Root-mean-square error
S	Time spectral density
Sc	Turbulent Schmidt number

$\mathbf{T}$	Transformation matrix
u_*	Friction velocity
u, v, w	Components of the velocity vector
$\mathbf{V}$	Velocity vector
$\ddot{\mathbf{x}}$	Acceleration vector
z_0	Aerodynamic roughness length
z	Height above the surface

Contents

Chapter 1

Introduction

The atmospheric surface layer is usually defined for land surfaces as the lower 10% of the planetary boundary layer (PBL), and is that part of the atmosphere directly influenced by contact with the Earth's surface, responding to surface forcing on a timescale of about an hour (Stull, 1988). This thin layer (a few tens of meters) is characterized by near-constant (less than 10% magnitude variation) turbulent fluxes, with vertical profiles of momentum, temperature, moisture, and pollutant concentrations increasing logarithmically with height. Near the surface (the first few millimeters) lies a thin layer called the aerodynamic roughness layer (or microlayer), of height equal to that point where the theoretical logarithmic profile for the wind speed is zero (the aerodynamic roughness height), or where the molecular transport processes dominate when compared with turbulent transport. In the presence of large or closely-spaced roughness elements (e.g. buildings and trees), the roughness length is displaced upward (the zero-plane displacement) to form an internal roughness layer.

Over the ocean, the atmospheric surface layer is referred to as the Marine Atmospheric Surface Layer (MASL), which has some special properties, such as the modulation of the flow by the sea waves, which creates an internal layer known as the wave boundary layer (Sjöblom and Smedman, 2003). Although Monin-Obukhov similarity theory is no longer valid within this layer, the logarithmic wind profiles is still present above it, with the estimated roughness length in the order of just a few millimeters (Garratt, 1977). This interesting behavior of the MASL is caused by the fact that the waves in fully-developed seas often move nearly as fast as the near-surface wind speed, and therefore, the resulting drag (e.g. Garratt (1994)) is, even for higher waves, considerably smaller than it would be for stationary roughness elements of the same size.

The internal roughness layer has not yet been clearly detected in observations taken over the oceans, although it has been theoretically discussed in studies based on numerical simulations (Belcher and Hunt, 1998) and laboratory experiments (Buckley and Veron, 2016). Despite that, it is reasonable to suppose the presence of a wave-induced roughness layer, especially when the waves are not aligned with the wind direction, which is often reported in open-sea regions.

The vertical structure of the PBL above the sea surface described here is schematically illustrated in Fig. 1.1.

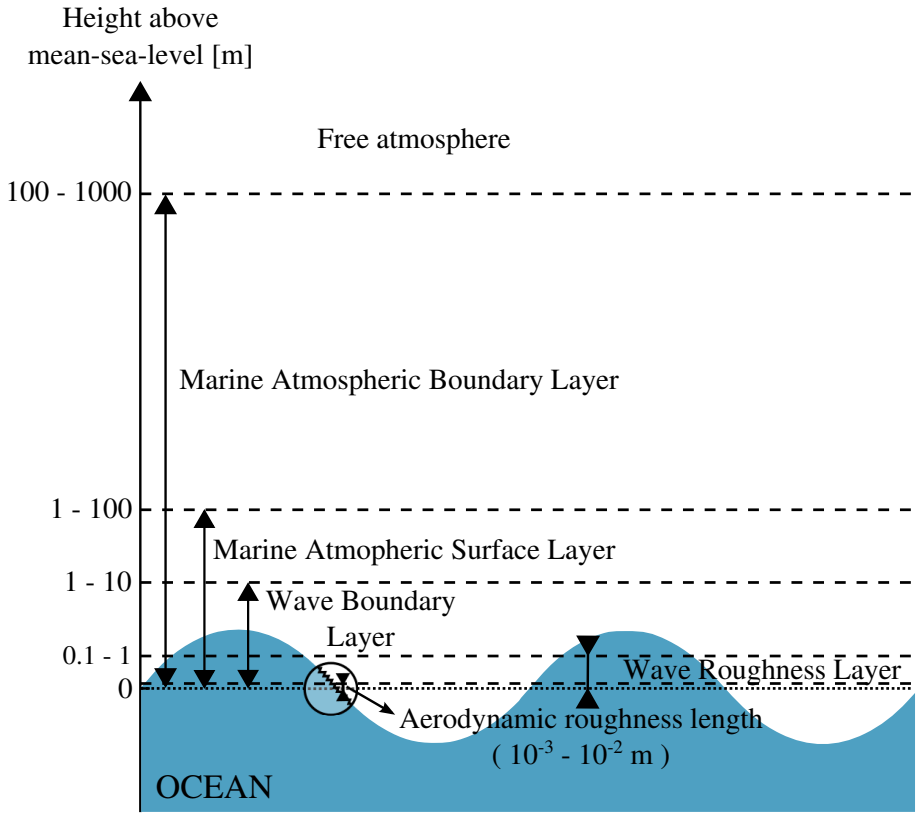

Figure 1.1: Vertical structure of the PBL above the sea surface.

Although turbulent fluxes on the air–sea interface have been studied intensively in the past decades (e.g. Sun and French (2016) and the references within), there is still uncertainty regarding the complete air–sea coupled system, where sea waves and the sea-surface temperature (SST) modulate the MASL and vice-versa. This two-way interaction is usually formulated in terms of the surface layer stability, or in the context of the Turbulent Kinetic Energy (TKE) budget equation. Furthermore, the majority of the available studies over the ocean are conducted in near-neutral stability conditions, which gives great

scientific importance to the studies of confluence regions, since the strong SST gradients there enable the investigation of a wide range of stability conditions over relatively small spatial and temporal scales.

In the air–sea coupled system, the turbulent flow above the sea surface is locally modulated by the energy provided by heat fluxes from the ocean surface (Pezzi et al., 2005; Small et al., 2008; Spall, 2007) and momentum delivered from the waves (Donelan et al., 1997; Kahma et al., 2016). At the same time, the SST and waves are modulated by the downward momentum flux from the atmosphere (Donelan et al., 2012; Gaube et al., 2015). In numerical simulations for weather and climate forecasting (i.e. models based on the Reynolds-averaged Navier Stokes equations), the roughness over the sea is expressed in terms of the drag coefficient (e.g. Garratt (1994)), which correlates the momentum flux to the mean flow parameters, typically the 10 m neutral wind speed. The momentum fluxes, in turn, are often analyzed in the context of the TKE budget equation (e.g. Högström (1996)), which describes the production, consumption, transport and dissipation of TKE.

With the main objective of exploring the air–sea interactions within the MASL, this work uses data from the *Air-Sea Interaction at Brazil-Malvinas Confluence* project (INTERCONF) (Pezzi et al., 2009), during which direct measurements of turbulence parameters were carried out aboard the Brazilian Polar Ship Almirante Maximiano H-41. This vessel supports the Brazilian Antarctic Research base, and thereby navigates once a year through the region of interest in the Southwestern Atlantic Ocean. This is a cyclogenetic and storm track region (Hoskins and Hodges, 2005; Reboita et al., 2010) mainly characterized by the presence of the Brazil–Malvinas Confluence (BMC), where the warm Brazilian Current meets the cold Malvinas Current, creating intense SST gradients, and is known as one of the most dynamically active regions of the world (Chelton et al., 1990; Piola et al., 2000).

Despite the importance of the Southwestern Atlantic Ocean for the atmospheric systems impacting the South American continent, there are few available in situ observations of momentum fluxes and atmospheric turbulence statistics in this region. The current scientific knowledge of processes related to momentum fluxes in the vicinity of the BMC is mainly based on bulk formulations derived in studies for other regions and applied to satellite datasets (O'Neill et al., 2010), numerical simulations (Camargo et al., 2013; Mendonça et al., 2017), and radiosonde measurements (Acevedo et al., 2010; Pezzi et al., 2016).

1.1 Objectives

The main objective of this work is to characterize the MASL over the Southwestern Atlantic Ocean, where the dynamic processes involving turbulent kinetic energy are modulated by wave and stability conditions. This thesis follows three lines of research, with each having its own specific objectives:

1. Theoretical study of the similarity theory and the turbulent processes of the atmospheric surface layer;
    - Build a quality-control algorithm for flux estimates;
    - Estimate the dissipation rate of TKE and scalar variances;
    - Evaluate the turbulent processes of the atmospheric surface layer in ideal conditions.
2. Data analysis of INTERCONF micrometeorological measurements;
    - Minimize the influence of ship motion on the velocity observations;
    - Estimate the momentum fluxes and the similarity parameters for the INTERCONF cruises;
    - Analyze processes involving upward momentum fluxes.
3. Simulation of the MASL over the BMC region;
    - Perform a numerical simulation of turbulent parameters using a regional atmospheric model;
    - Compare simulation results with in situ observations collected during the INTERCONF cruise.

Chapter 2

Theory of the atmospheric surface layer

This chapter introduces the scientific background necessary for atmospheric surface layer studies applicable for either ocean or land surfaces. Here, the expressions describing the atmospheric surface layer are formulated and evaluated based on a reliable dataset collected during the *Boundary Layer Late Afternoon and Sunset Turbulence* (BLLAST) experiment (Lothon et al., 2014). Although the BLLAST dataset is not directly related to the main focus of this work, which is the MASL, the validity of the universal surface layer expressions and the similarity functions are better tested using a reliable land-based dataset. The chapter concludes with a discussion about the modeling of the atmospheric surface layer for field experiments, such as the INTERCONF project.

The results concerning the atmospheric surface layer study for the BLLAST dataset are published in Hackerott et al. (2017), on which the theories and discussions presented here are based.

2.1 The Boundary Layer Late Afternoon and Sunset Turbulence dataset

The BLLAST experiment was held from 14 June to 8 July 2011 in France (*Plateau de Lannemezan*), a few kilometers north of the foothills of the Pyrénées. The surrounding area is characterized by a flat surface (150×150 m^2) covered with short grass. The vegetation within a radial distance of 500 m is composed of crops (wheat and maize), moorland and patches of forest (van de Boer et al., 2014).

Although there was a large number of instruments available, such as data from a 60 m micrometeorological tower, radiosondes, tethered balloons, aircraft, drones, lidar, and sodar, only measurements of the velocity components, air temperature, and the concentra-

tions of water vapor and carbon dioxide, carried out on a 2 m micrometeorological mast, were considered. The measurement system, operating at a sampling frequency of 20 Hz, includes a sonic anemometer (Campbell CSAT 3) and an open-path gas analyzer (LiCor 7500), as illustrated in Fig. 2.1. This was the instrumentation set-up available in the BLLAST campaign that most closely resembles to the set-up used during the INTERCONF campaigns.

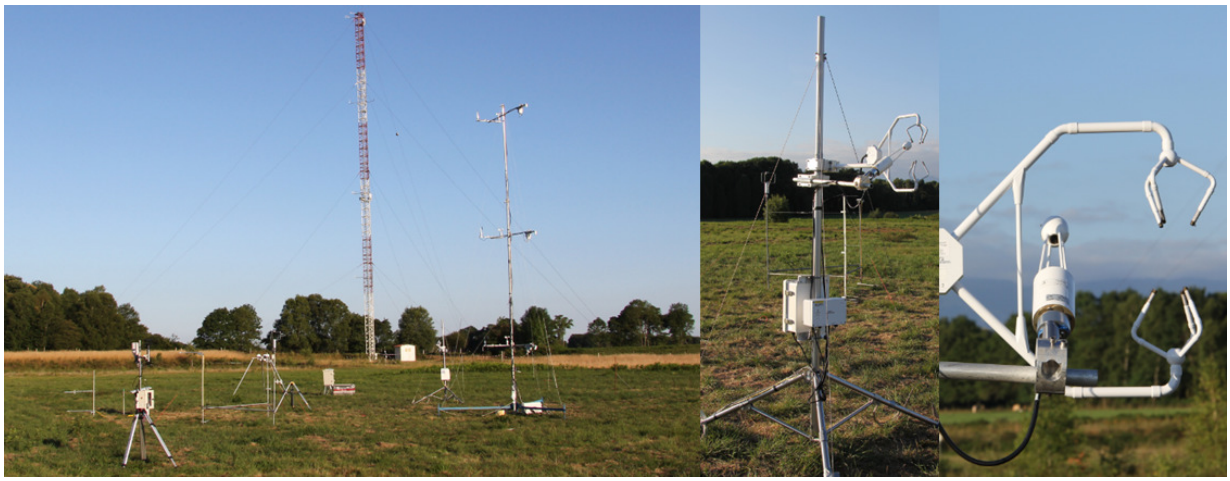

Figure 2.1: Photos of the field set-up (left) of Surface Site 3 at Site 1 of the BLLAST campaign, with the micrometeorological mast (middle), and the sonic anemometer and open-path gas analyzer (right). Adapted from (Hackerott et al., 2017).

The methodology related to data assessment and quality control is further discussed in Chapter 3. For now, it is considered that the data is already filtered based on the requirements described below. The temperature is the virtual potential temperature (θ), the humidity is the specific humidity (q), the pollutant gas is the specific CO_2 content (c) and the velocity data is aligned with the streamwise direction (i.e. the mean vertical and transversal velocities are both equal to zero, $\overline{v} = \overline{w} = 0$).

2.2 The turbulent fluxes and scaling parameters

The vertical kinematic flux of any quantity is mathematically expressed by the average of the multiplication of a certain quantity with the vertical velocity component. Additionally, any meteorological variable can be expressed as the sum of a mean and a turbulent part, which is defined as the fluctuation around the mean. Therefore, the vertical kinematic eddy flux is expressed by the average of the multiplication of the fluctuation of some

quantity with the fluctuation of the vertical velocity component. The fluctuation of meteorological quantities are measured by high-frequency sensors, such as a sonic anemometer, which measures flow properties sampled at 20 Hz, while the mean properties are defined for a time scale large enough to capture all turbulent eddies, which is about a few tens of minutes.

The turbulent fluxes transporting energy between different atmospheric layers are known as the momentum flux (τ), the sensible heat flux (H) and the latent heat flux LE, which are estimated from the vertical kinematic eddy fluxes using the expressions

$$\tau = \rho\sqrt{\left(\overline{u'w'}\right)^2 + \left(\overline{v'w'}\right)^2} \ , \tag{2.1}$$

$$H = -\rho \ C_p\overline{\theta'w'} \tag{2.2}$$

and

$$LE = -\rho \ L_e\overline{q'w'} \ , \tag{2.3}$$

respectively, where ρ is the air density, and u', v', w', q', and θ' are the fluctuations of the velocity components, water vapor concentration and virtual potential temperature. Here, $C_p = 1004.67$ J kg^{-1} K^{-1} is the specific heat of dry air at constant pressure, and $L_e = 2.45 \times 10^6$ J kg^{-1} is the latent heat of vaporization.

The atmospheric surface layer is "*the region at the bottom of the boundary-layer where turbulent fluxes and stress vary by less than 10% of their magnitude*" (Stull, 1988). Therefore, the vertical kinematic eddy fluxes within this layer are considered constant, enabling the definition of turbulent scaling parameters. These parameters are the friction velocity (u_*), the scalar characteristic scales (χ_*) and the Obukhov length (L), where the latter is often referred by the height-dependent stability parameter ($\zeta = \frac{z}{L}$), which indicates whether the atmospheric surface layer is stable ($\zeta > 0$) or convective ($\zeta < 0$), corresponding to whether the buoyancy acts as a sink or source of TKE, respectively.

The scaling parameters can be estimated using the eddy-covariance method (Aubinet et al., 2012), which computes the covariances (second-moments) from high-frequency data. The expressions for each atmospheric surface layer scaling parameter are

$$u_* = \left[\left(\overline{u'w'}\right)^2 + \left(\overline{v'w'}\right)^2\right]^{\frac{1}{4}} \ , \tag{2.4}$$

$$\chi_* = -\frac{\overline{\chi'w'}}{u_*} \ , \tag{2.5}$$

and

$$L = \frac{u_*^2 \theta_0}{\kappa g \theta_*} \ , \tag{2.6}$$

where κ is the von Kármán constant ($\kappa \approx 0.4$), g is the acceleration due to gravity, and θ_0 is the reference virtual potential temperature.

Regardless of the simplicity of Eqs. (2.4), (2.5) and (2.6), special care must be taken to guarantee two main criteria of the eddy-covariance method: the stationarity of the flow, and the representation of all relevant scales of turbulent eddies. Stationary flow is important to ensure that the covariances are not affected by mechanisms other than boundary-layer isotropic turbulence, such as mesoscale variability or disturbed turbulent flows. While the stationarity criterion favors short data segments (few minutes), the capture of all scales typically requires longer averaging intervals (several minutes).

Within the BLLAST dataset, ζ has been visually correlated with θ_*, q_* and c_*. Hackerott et al. (2017) argue that while ζ is assigned the same sign as θ_* by definition (see Eq. (2.6)), for q_* and c_*, the direction of the kinematic eddy flux is not dependent on the stability, but on the scalar content gradient between the atmospheric surface layer and the first millimeter of air above the surface. In the case of CO_2 content, the sign of c_* is related to the photosynthesis activity, which is positive during the daytime and negative during the nighttime over vegetated fields. Nevertheless, the absolute magnitude of all characteristic scales is affected by the turbulence, increasing when the turbulent eddies are stronger, either due to mechanical or to buoyant turbulence production.

The characteristic scales are usually compared with ζ using the similarity relationships (Wyngaard et al., 1971; Pahlow et al., 2001) $\frac{\sigma_w}{u_*}(\zeta)$ and $\frac{\sigma_\chi}{|\chi_*|}(\zeta)$, where σ is the standard deviation function. In near-neutral conditions, the values for $\frac{\sigma_\chi}{|\chi_*|}$, where χ represents θ, q or c, increase rapidly, and thus the y-axis is usually limited for plotting purposes. Hackerott et al. (2017) highlight that the values of $\frac{\sigma_q}{|q_*|}$ are observed to be slightly higher than those for $\frac{\sigma_\theta}{|\theta_*|}$ (see Fig. 2.2), as theoretically predicted by Katul and Hsieh (1999), although both decrease to close to one during the convective regime, while behaving similarly. For $\frac{\sigma_c}{|c_*|}$, however, it also decreases with the enhancement of the convective stability regime, but shows much more scatter and higher values in comparison with the similarity relation observed for θ and q. During near-neutral and stable regimes, $\frac{\sigma_w}{u_*}$ is 1.36 ± 0.15, which is acceptable considering the constant value of 1.1 found by Pahlow et al. (2001). The BLLAST dataset is considered, therefore, in agreement with the following similarity func-

tions proposed by Wyngaard et al. (1971) for the convective regime, and that proposed by Pahlow et al. (2001) for the stable regime, where

$$\frac{\sigma_w}{u_*}(\zeta) = \begin{cases} 1.8(-\zeta)^{\frac{1}{3}} , & \zeta \leq 0 \\ 1.1 + 0.9(\zeta)^{0.6} , & \zeta > 0 \end{cases} \tag{2.7}$$

and

$$\frac{\sigma_\theta}{|\theta_*|}(\zeta) = \begin{cases} 0.95(-\zeta)^{-\frac{1}{3}} , & \zeta \leq 0 \\ 3 + 0.05(\zeta)^{-1} , & \zeta > 0 \end{cases} \tag{2.8}$$

for $-2 < \zeta < 0.5$.

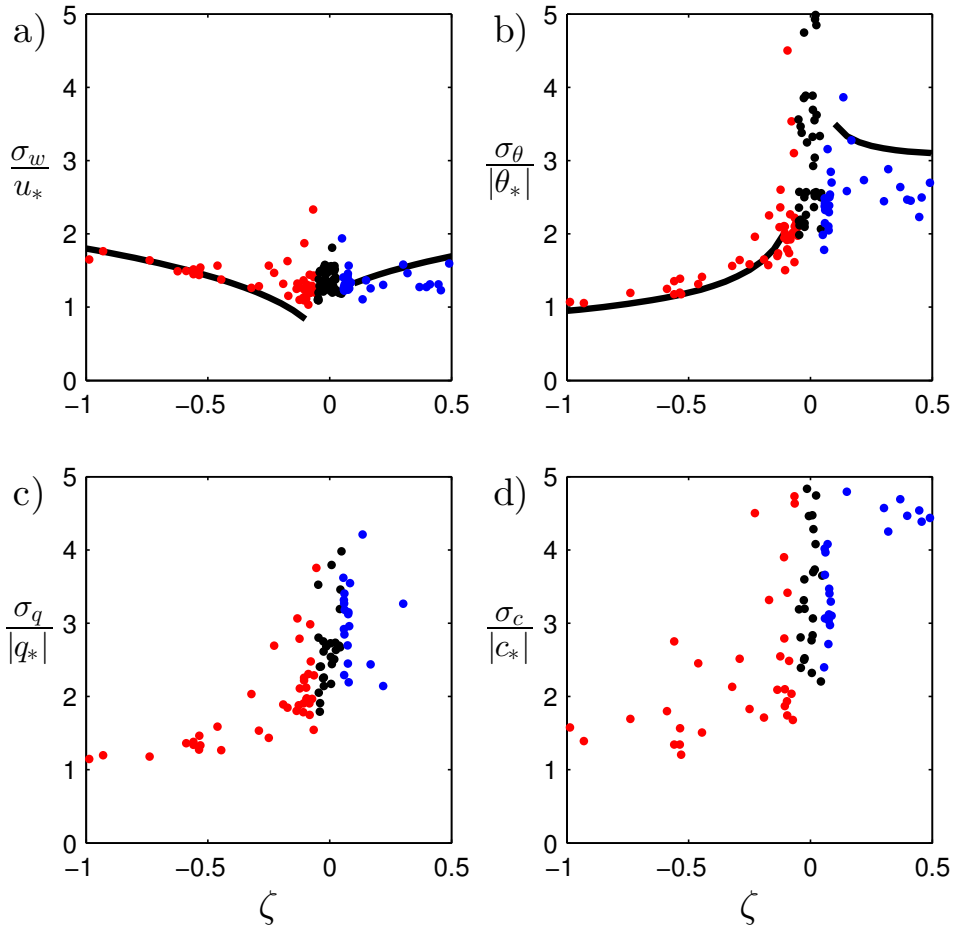

Figure 2.2: Non-dimensional standard deviation versus the stability parameter (ζ) for the (a) vertical velocity component, (b) virtual potential temperature, (c) specific humidity, and (d) specific CO_2 content. The colors indicate the convective (red), near-neutral (black), and stable (blue) regimes. The black lines in (a) and (b) are the similarity expressions derived by Wyngaard et al. (1971) for the convective regime and by Pahlow et al. (2001) for the stable regime, and expressed by Eqs 2.7 and 2.8. Adapted from Hackerott et al. (2017).

The discrepancies among the values of $\frac{\sigma_\chi}{|\chi_*|}$ evaluated for different scalars are interpreted

as scalar dissimilarity resulting from inhomogeneous distribution of distinct scalar source fields (Williams et al., 2007). In this case, Hackerott et al. (2017) hypothesize that the different patches surrounding the experimental site do not cause significant heterogeneity in the latent and sensible heat sources, but imply significant inhomogeneity of the CO_2 sources and sinks, leading to intermittent CO_2 turbulent processes.

2.3 The Kolmogorov power law and the dissipation rates

The Kolmogorov power law (Kolmogorov, 1941) is a similarity theory (Garratt, 1994) assuming the existence of an inertial subrange of wavenumbers (k), where the energy is only transferred from large to small scales at the dissipation rate of TKE (ϵ) or indeed the dissipation rate of any scalar variance (N_χ). From dimensional analysis (Sorbjan, 1989), the relations between the spatial one-dimensional energy spectrum ($\mathscr{H}$), k and ϵ or N_χ are

$$\mathscr{H}_w(k) = \alpha\epsilon^{\frac{2}{3}}k^{-\frac{5}{3}} \tag{2.9}$$

and

$$\mathscr{H}_\chi(k) = \beta\epsilon^{-\frac{1}{3}}N_\chi k^{-\frac{5}{3}}, \tag{2.10}$$

where α is the Kolmogorov constant, with $\alpha = 0.7$ in the case of the vertical velocity spectra (Kaimal et al., 1972), which is more often used than the longitudinal velocity, because it appears to be less intermittent (Nilsson et al., 2016; Hackerott et al., 2017), and $\beta = 0.8$ is the Obukhov-Corrsin constant, which can be assumed to be invariant for $\chi = \theta$, $\chi = q$ or $\chi = c$ (Hill, 1989; Högström, 1996; Iwata et al., 2005).

Assuming the Taylor Hypothesis of frozen turbulence (Willis and Deardorff, 1976), the relationship between the wavenumber and the time frequency (n) is $k = \frac{2\pi n}{\overline{u}}$, where $\overline{u}$ is the mean longitudinal wind speed. As a consequence, the time spectral density (S) is related to $\mathscr{H}(k)$ by $S(n) = \frac{2\pi}{\overline{u}}\mathscr{H}(\frac{2\pi n}{\overline{u}})$, and Eqs. (2.9) and (2.10) can be rewritten for the time spectral density as

$$S_w(n) = \alpha\epsilon^{\frac{2}{3}}n^{-\frac{5}{3}}\left(\frac{2\pi}{\overline{u}}\right)^{-\frac{2}{3}} \tag{2.11}$$

and

$$S_\chi(n) = \beta\epsilon^{-\frac{1}{3}}n^{-\frac{5}{3}}N_\chi\left(\frac{2\pi}{\overline{u}}\right)^{-\frac{2}{3}}. \tag{2.12}$$

The spectral densities for a time series are computed using the Fast Fourier Transform (FFT), which requires additional treatment to reduce undesirable inherent noise (Stull, 1988). The data segments must be detrended, and tapered by 5% with a Tuckey window function (Bloomfield, 2000). Hackerott et al. (2017) suggest based on visual inspection of spectral curves calculated for different segment lengths to use 18,000 points of a 20 Hz sampled data segment (15 min), which is justified to be large enough to ensure that the low-frequency limit of the inertial subrange is well-resolved in the FFT calculations. As this method is very sensitive to the stationarity assumption (Bluteau et al., 2011), it is more likely to be violated when using longer data segments (e.g. 30 min), which would result in an elevated spectral density due to white noise.

Once $S_w(n)$ is calculated, ϵ is estimated from Eq. (2.11) using a non-linear least-squares fit within the inertial subrange to determine ϵ, which is illustrated in Fig. 2.3 where the fitted curve is highlighted in blue. Next, N_χ is estimated based on Eq. (2.12), also by applying a non-linear fit to the respective inertial subrange of $S_\chi(n)$.

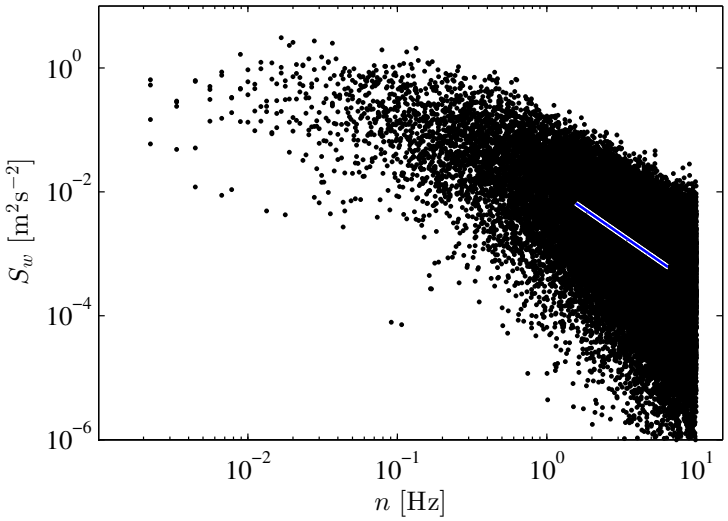

Figure 2.3: Example of the energy density spectrum of the vertical velocity component [m^{2}s^{-2}] versus frequency [Hz], with the curve defined by Eq. (2.11) and fitted using a non-linear least-squares fit within the detected inertial subrange.

To provide a representative value for each dissipation rate within a 30-min segment, Hackerott et al. (2017) suggest an iterative method. First, all 30-min intervals are enlarged by 14 min before and after the original segment, resulting in 69,600 data samples. Within the iterative process, the dissipation rates for 15-min intervals are calculated, starting at the beginning of the extended segment, and then repeated by moving the start point in

increments of 1 min until the end of the extended segment is reached. This iteration ensures that almost all data of the original 30-min interval (excluding the first and last 1-min period) are weighted equally. The dissipation rate for the 30-min segment is then defined as the median of the 44 iterations, which is used instead of the average to prevent the overestimation of dissipation rates arising from non-stationarities.

2.3.1 Determination of the inertial subrange

The determination of the inertial subrange is crucial for accurately estimating the dissipation rates. With the purpose of determining the inertial subrange limits, Hackerott et al. (2017) suggest an iterative method that evaluates the variations of the constants α and β defined in Eqs. 2.11 and 2.12 by keeping constant values for the dissipation rates within a frequency interval I. From the definition of the inertial subrange, both the dissipation rates and α, or β, are constant and, therefore, the boundaries for I can be defined by identifying the minimum standard deviation calculated for α, or β, in different regions of the spectra.

The spectra calculated from 18,000 data samples collected at 20 Hz are divided into 48 frequency blocks (Table 2.1), of which the number of estimates per block is logarithmically distributed, similar to that proposed by Kaimal and Gaynor (1983).

For each block-centered frequency n^*, the average power-spectrum, $\overline{S}(n^*)$, and the dissipation rate of TKE $\epsilon^*(\overline{S_w}(n^*), n^*)$, are calculated using

$$\epsilon^* = \left(\frac{\overline{S_w}(n^*)}{\alpha}\right)^{\frac{3}{2}} n^{*\frac{5}{2}} \left(\frac{2\pi}{\overline{u}}\right) . \tag{2.13}$$

The iteration among the blocks consists of a loop starting from the centered frequency block $n^* = 0.0922$ Hz (index 22 in Table 2.1) and moving the interval I towards the higher frequencies, one block per iteration, up to $n^* = 4.5244$ Hz (index 44). For this method, Hackerott et al. (2017) suggest a window size for the interval I that includes nine consecutive blocks.

For each iteration, α is estimated for a total of nine block-centered frequencies within I, keeping ϵ^* as a constant equal to the one corresponding to the fifth block from I (i.e. the block in the middle of I). Finally, the standard deviation of α (σ_α) is calculated for each I.

Table 2.1 - Number of estimates used to smooth the power spectra, from 18,000 data samples collected at 20 Hz.

Frequency block index	Number of estimates per block	Centered frequency n^* [Hz]
1	1	0.0011
2	1	0.0022
3	1	0.0033
4	1	0.0044
5	1	0.0056
6	1	0.0067
7	1	0.0078
8	1	0.0089
9	1	0.0100
10	1	0.0111
11	2	0.0128
12	3	0.0156
13	3	0.0189
14	3	0.0222
15	5	0.0267
16	5	0.0322
17	6	0.0383
18	7	0.0456
19	8	0.0539
20	11	0.0644
21	12	0.0772
22	15	0.0922
23	17	0.1100
24	21	0.1311
25	25	0.1567
26	29	0.1867
27	36	0.2228
28	42	0.2661
29	50	0.3172
30	61	0.3789
31	72	0.4528
32	86	0.5406
33	102	0.6450
34	122	0.7694
35	147	0.9189
36	174	1.0972
37	208	1.3094
38	249	1.5633
39	296	1.8661
40	355	2.2278
41	422	2.6594
42	505	3.1744
43	603	3.7900
44	719	4.5244
45	859	5.40111
46	1025	6.44778
47	1224	7.69722
48	1461	9.18889

The inertial subrange is then defined as the I that has the smallest σ_α after completing the iteration. The method succeeds if the smallest σ_α is smaller than 0.07 (i.e. 10% of α).

A similar procedure is carried out for the estimation of I in the power spectra of χ. Since ϵ is now known, the following expression is applied in an analogous way as described before, but using β instead of α,

$$N^*_{\chi_i} = \left(\frac{\overline{S_{\chi_i}}(n^*)}{\beta}\right)\epsilon^{\frac{1}{3}} {n^*}^{\frac{5}{3}} \left(\frac{2\pi}{\overline{u}}\right)^{\frac{2}{3}} . \tag{2.14}$$

2.4 The variance budget equations

The variance budget equations and TKE budget equation are the expressions that describe the dynamic processes in the turbulent boundary-layer. Assuming homogeneous turbulent flow in the absence of subsidence, neglecting any effects of molecular diffusion and radiation destruction, and with the coordinate system aligned to the mean wind direction, the TKE and scalar variance budget equations are

$$\frac{\partial \overline{e}}{\partial t} = -\overline{u'w'}\frac{\partial \overline{u}}{\partial z} + \frac{g}{\theta_0}\overline{\theta' w'} - \frac{\partial \overline{ew'}}{\partial z} - \frac{1}{\rho_0}\frac{\partial \overline{p'w'}}{\partial z} - \epsilon \tag{2.15}$$

and

$$\frac{1}{2}\frac{\partial \overline{\chi'^2}}{\partial t} = -\overline{\chi' w'}\frac{\partial \overline{\chi}}{\partial z} - \frac{1}{2}\frac{\partial \overline{\chi'^2 w'}}{\partial z} - N_\chi, \tag{2.16}$$

respectively, where $e = \frac{1}{2}(u'^2 + v'^2 + w'^2)$ is the TKE, ρ_0 is the reference air density, and p' is the fluctuation of the atmospheric pressure. The overbar and prime denote Reynolds averages and instantaneous fluctuations, respectively.

Using the characteristic-scale definition (Sect 2.2), considering a steady-state surface layer, and normalizing Eq. (2.15) by $\frac{\kappa z}{u_*^2}$, as well as (2.16) by $\frac{\kappa z}{\chi_*^2}$, the variance budget equations assume the traditional form,

$$\underbrace{\frac{\kappa z}{u_*}\frac{\partial \overline{u}}{\partial z}}_{\Phi_u^P} - \underbrace{\frac{\kappa z \theta_*}{{u_*}^2}\frac{g}{\theta_0}}_{\zeta} - \underbrace{\left[\frac{\kappa z}{{u_*}^3}\frac{\partial \overline{ew'}}{\partial z} + \frac{\kappa z}{{u_*}^3}\frac{1}{\rho_0}\frac{\partial \overline{p'w'}}{\partial z}\right]}_{\Phi_u^T} - \underbrace{\frac{\kappa z}{{u_*}^3}\epsilon}_{\Phi_u^D} = 0 \tag{2.17}$$

and

$$\underbrace{\frac{\kappa z}{\chi_*}\frac{\partial \overline{\chi}}{\partial z}}_{\Phi_\chi^P} - \underbrace{\frac{\kappa z}{2u_*{\chi_*}^2}\frac{\partial \overline{\chi'^2 w'}}{\partial z}}_{\Phi_\chi^T} - \underbrace{\frac{\kappa z}{u_*{\chi_*}^2}N_\chi}_{\Phi_\chi^D} = 0, \tag{2.18}$$

where Φ_u^P is the non-dimensional mechanical production of TKE, and Φ_χ^P is the non-dimensional production of χ variance. The superscript T indicates transport and D dissipation. The buoyancy component (ζ) is, by definition, the Monin-Obukhov stability parameter. The sum of the vertical transport of TKE and divergence of pressure transport in Eq. (2.17) is often treated as the total non-dimensional transport of TKE, Φ_u^T.

It is interesting to note that in the absence of heat or CO_2 fluxes (i.e. $\overline{\chi' w'} = 0$), when the characteristic-scales vanish (i.e. $\chi_* = 0$), all terms in Eq. (2.18) become undefined, leading to an asymptotic behavior with large positive and negative values. In these cases, χ_* is an unsuitable scaling parameter (Jensen et al., 2016), although the classical formulations for Φ_θ^P indicate a constant value for the near-neutral regime (Dyer, 1974; Högström, 1996). Jensen et al. (2016) explain that, in the absence of a heat flux, non-local effects may become important, so that Φ_θ^P becomes a poor indicator of the local heat fluxes.

For near-neutral conditions ($\zeta \approx 0$), $\theta_* \to 0$ and a singularity occurs in Eq. (2.18). This is not the case for q and c, where the signs of q_* and c_* are determined by the direction of the corresponding vertical gradients, which are not necessarily correlated with ζ. However, it is important to exclude the segments with $|q|_* < 0.01$ g kg^{-1} and $|c|_* < 0.1$ mg kg^{-1} to evaluate the behavior of the variance budget terms. This singularity is not observed for the TKE budget equation, because one of the quality-control tests for the eddy-covariance method, the Taylor's hypothesis test, certifies that $u_* \not\approx 0$.

2.5 The similarity theory for the terms of the variance budget equation

From Monin-Obukhov similarity theory, Φ_u^P and Φ_θ^P may be expressed in terms of ζ. According to Foken (2006), the most acceptable universal functions for the variance production terms, as described by Högström (1996), are

$$\Phi_u^P(\zeta) = \begin{cases} (1 - 19\zeta)^{-\frac{1}{4}} , & \zeta \leq 0 \\ 1 + 5.3\zeta , & \zeta > 0 \end{cases} \tag{2.19}$$

and

$$\Phi_\theta^P(\zeta) = \begin{cases} 0.95(1 - 11.6\zeta)^{-\frac{1}{2}} , & \zeta \leq 0 \\ 1 + 8\zeta , & \zeta > 0 \end{cases} \tag{2.20}$$

for $-2 < \zeta < 0.5$.

The dissipation term of the TKE budget equation can also be described in the framework of the Monin-Obukhov similarity theory (Hill, 1997). However, the consensus

about the universal function for $\Phi_u^D(\zeta)$ and $\Phi_\chi^D(\zeta)$ has still not yet been reached, and different expressions are available (Ohtaki, 1985; Kader, 1992; Hartogensis and Bruin, 2005; Pahlow et al., 2001; Hackerott et al., 2017). Using the BLLAST dataset, Hackerott et al. (2017) propose the following linear functions for $\Phi^D(\zeta)$

$$\Phi^D(\zeta) = \zeta\ a^{\pm} + b^{\pm}, \tag{2.21}$$

where the superscripts indicate convective $(-)$ and stable $(+)$ regimes, and $a^{\pm}$ and $b^{\pm}$ are, respectively, the slope and intercept coefficients for the linear regression (Table 2.2).

Table 2.2 - Coefficients $a^{\pm}$ and $b^{\pm}$ for the regression defined in Eq. (2.21). Here, R^2 and $RMSE$ are the squared correlation coefficient and the root-mean-square error, respectively. The p-values for individual coefficient estimates < 0.001 are based on a t-test.

		Φ_u^D	Φ_θ^D	Φ_q^D
Convective	b^-	0.77	0.39	0.36
	a^-	-0.25	0.22	0.25
	R^2	0.04	0.28	0.27
	$RMSE$	0.31	0.09	0.10
Stable	b^+	0.77	0.39	0.36
	a^+	1.06	2.56	3.67
	R^2	0.42	0.66	0.11
	$RMSE$	0.23	0.50	1.45

The results for Φ^D versus ζ estimated during the BLLAST experiment by Hackerott et al. (2017) are presented in Fig. 2.4. Although the correlation coefficient (R^2) for Φ_χ^D delivers low values for the convective surface layer compared with the stable one, the root-mean-square error ($RMSE$) is much lower, indicating a higher precision of the regression curves for convective conditions. The results for Φ_u^D show a weak correlation with ζ for both the convective and stable regimes as a consequence of the high correlation between the dissipation rate of TKE and the wind speed, which is, therefore, more affected by mesoscale variability than the local turbulent motions. While there are several possible factors that influence the quality of the Φ_u^D computations, Hackerott et al. (2017) conclude that the universal function should include the effect of the mean wind speed, as also recommended by Yelland and Taylor (1996), who proposed different functions for the $3-7$ m s^{-1}, $10-12$ m s^{-1} and $17-20$ m s^{-1} wind-speed regimes. However, the BLLAST dataset

only covers the lowest of those wind-speed intervals, which emphasizes the need for more relevant mechanisms rather than only ζ.

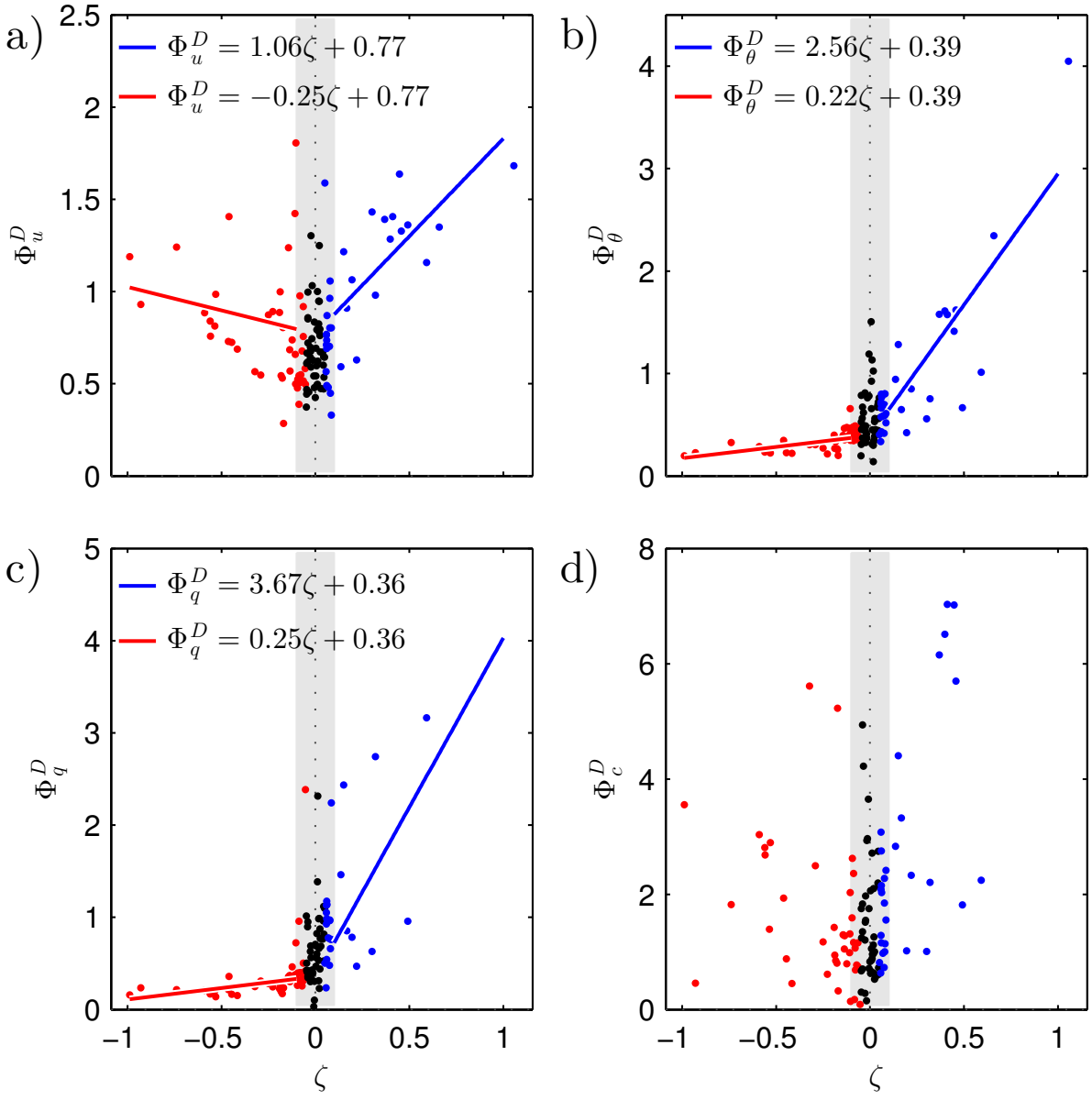

Figure 2.4: Non-dimensional dissipation component (Φ^D) versus the Monin-Obukhov stability parameter (ζ) for the budget equation of: (a) turbulent kinetic energy; (b) the variance of virtual potential temperature; (c) the variance of specific humidity; and (d) the variance of specific CO_2 content, estimated for the BLLAST experiment. The colors indicate convective (red), near-neutral (black) and stable (blue) conditions. The red and blue lines are the linear regressions estimated for the convective and stable regimes, respectively. The gray area corresponds to $|\zeta| \leq 0.1$, where data are not considered for the linear fit. Adapted from Hackerott et al. (2017).

During the stable regime, Hackerott et al. (2017) argued that the high scatter of Φ^D

versus ζ (i.e. relatively high $RMSE$) and the small correlation coefficients (i.e. $R^2 < 0.7$) increase the difficulty in finding appropriate similarity expressions. For this reason, they kept the intercept coefficient for the stable regime equal to that estimated for the convective regime. In addition, since Φ_q^D and Φ_c^D for near-neutral conditions ($|\zeta| \leq 0.05$) were observed to be insufficient to avoid singularities, they suggested enlarging this range to $|\zeta| \leq 0.1$ to provide a less biased representation of the universal functions.

A high scatter in the stable regime has also been reported by Pahlow et al. (2001); Hartogensis and Bruin (2005); Nilsson et al. (2016), and, as a consequence, the available universal functions reported in the literature vary substantially. For example, Pahlow et al. (2001) found $a^+ = 5$ and $b^+ = 0.61$, while Hartogensis and Bruin (2005) found $a^+ = 2.5$ and $b^+ = 8$ for Φ_u^D. The only consensus is that Φ_u^D increases as the surface layer becomes more stable. For Φ_χ^D, however, there is no consensus in the literature, and few functions are available. Pahlow et al. (2001) suggested a constant value near unity in the range $0 < \zeta < 100$ for Φ_θ^D, although their data varies randomly between 0.1 and 10. In general, the results presented in Fig. 2.4 show an increasing magnitude of Φ^D in the stable surface layer and significant differences between the slope coefficients of the proposed linear function, independent of the evaluated scalar variance.

The similar results obtained for $\Phi_\theta^D(\zeta)$ and $\Phi_q^D(\zeta)$ during the convective regime are explained by scalar similarity (discussed in more detail in Sect. 2.6), which is in agreement with results from Kader (1992), and would also be in agreement with Ohtaki (1985) for c, if the same coefficients were observed for this scalar. Although these authors proposed different functions, their curves can be approximated by linear functions in the range $-1 < \zeta \leq -0.2$, with a similar slope and slightly higher magnitudes than the ones proposed by Hackerott et al. (2017). For $-0.2 < \zeta < 0$, the parameterizations proposed by Kader (1992) and Ohtaki (1985) cannot be considered linear since they increase rapidly in magnitude, which may be a consequence of the influence of the singularities that occur in the near-neutral regimes, and which were not neglected by these authors.

The non-dimensional transport terms for TKE and the variance of θ can be estimated as a residual term in Eqs. (2.17) and (2.18), since universal functions for the Φ_u^P and Φ_θ^P are well-established (see Eqs. (2.19) and (2.20)), and the dissipation terms are independently estimated. This method can also be extended to Φ_q^T and Φ_c^T by assuming scalar similarity to Φ_θ^T.

In the similarity form, the expressions for Φ^T are

$$\Phi_u^T(\zeta) = \begin{cases} (1-19\zeta)^{-\frac{1}{4}} + \zeta\ a^- + b^- & -1 < \zeta < -0.1 \\ b^+ + \zeta\ a^+\ , & 0.1 < \zeta < 0.5 \end{cases} \tag{2.22}$$

and

$$\Phi_\chi^T(\zeta) = \begin{cases} 0.95(1-11.6\zeta)^{-\frac{1}{2}} + \zeta\ a^- + b^-\ , & -1 < \zeta < -0.1 \\ b^+ + \zeta\ a^+\ , & 0.1 < \zeta < 0.5 \end{cases} \tag{2.23}$$

where the coefficients adjusted for the BLLAST campaign $a^\pm$ and $b^\pm$ are summarized in Table 2.3.

Table 2.3 - Coefficients $a^\pm$ and $b^\pm$ for the regressions defined in Eqs. (2.22) and (2.23).

		Φ_u^T	Φ_θ^T	Φ_q^T
Convective	b^-	-0.77	-0.39	-0.36
	a^-	-0.75	-0.22	-0.25
Stable	b^+	0.23	0.61	0.64
	a^+	3.24	5.44	4.33

The results for Φ^T estimated for the BLLAST experiment are presented in Fig. 2.5. It is important to note that Hackerott et al. (2017) could not estimate Φ_c^T due to dissimilarities observed for Φ_c^D. Although large scatter was observed for Φ_u^T, the proposed universal function is in agreement with the results from Dupuis et al. (1997), who proposed the linear relation $\Phi_u^T = -0.65\zeta$ for $-7 < \zeta < 0$, and Nilsson et al. (2016) who suggested the approximation $\Phi_u^T \approx -0.5\zeta$ for $-8 < \zeta < 0$. The curves proposed by these authors suggest a convergence to low values in the near-neutral stability regime in agreement with Fairall and Larsen (1986) who showed that Φ_u^T is only $\approx 25\%$ of Φ_u^D in this regime. The results from Hackerott et al. (2017), however, indicate an average ratio between Φ_u^T and Φ_u^D equal to 0.6 ± 0.4 for $|\zeta| \leq 0.05$.

For Φ_χ^T, however, the BLLAST results indicate convergence to low values in the convective regime, which means that these terms may be neglected in this regime. For the stable surface layer, Φ^T increases in magnitude as the surface layer becomes more stable, where the magnitude of Φ^T becomes comparable to Φ^P and Φ^D.

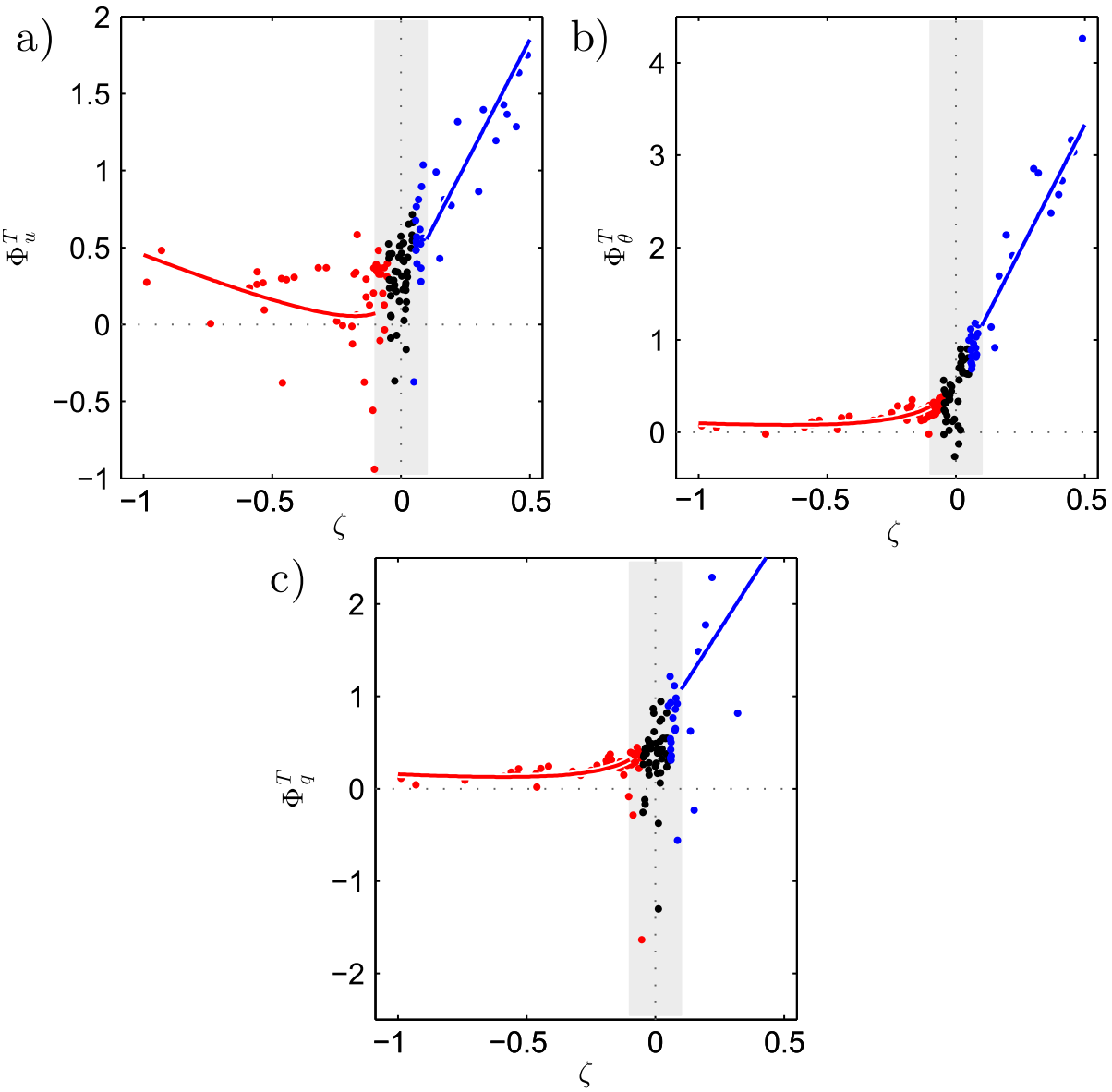

Figure 2.5: Non-dimensional total transport component (Φ^T) versus the stability parameter (ζ) for the budget equation of (a) turbulent kinetic energy, and variances of (b) virtual potential temperature, and (c) specific humidity, estimated for the BLLAST experiment. The colors indicate the convective (red), near-neutral (black) and stable (blue) regimes. The lines are the total transport term estimated as a residual of the variance budget equations, considering the suggested parameterizations for the non-dimensional dissipation and dynamical production terms. The gray area corresponds to $|\zeta| \leq 0.1$, where data are not considered for the parameterizations. Adapted from Hackerott et al. (2017).

2.6 *Scalar similarity in the atmospheric surface layer*

Turbulent processes within the atmospheric surface layer do not only promote similarity among different variance budget terms considering one variable, but also promote

similarity among scaling parameters evaluated from different variables. Although questionable (Foken, 2006), many studies have shown similarities between the variance production of temperature and humidity (Dyer, 1974; Hill, 1989; Högström, 1996), implying that the turbulent Prandtl number (Pr) equals the turbulent Schmidt number (Sc), i.e. $\Phi_\theta^P = \Phi_q^P$. Hackerott et al. (2017) show that scalar similarity is also valid for the variance dissipation and transport, and observed dissimilarities may result from three main factors (Katul et al., 2008): 1) surface heterogeneity, 2) non-stationarity of the data, and 3) entrainment (non-local processes).

According to Hill (1989), while scalar similarity is expected for Φ_χ^D where the Monin-Obukhov similarity theory has been verified, this similarity was not observed in the BLLAST experiment for Φ_c^D (see Fig. 2.4d), where the scatter was observed to be much higher than that observed for Φ_θ^D and Φ_q^D, and no linear regression could be applied. The assumption of Monin-Obukhov similarity theory is based on an area-averaged description of turbulence statistics and, as a consequence, local sinks or sources of some scalars result in imperfect scalar–scalar correlation (Rannik, 1998). The heterogeneous surface land use in the vicinity of the BLLAST experiment could imply different sinks and sources of CO_2 throughout the diurnal cycle, resulting in the dissimilarity observed for Φ_c^D compared with Φ_θ^D and Φ_q^D. Hackerott et al. (2017) argued that the steady-state filter, based on Taylor's hypothesis, is insufficient to remove data contaminated by inhomogeneities in the CO_2 time series, which results in scalar dissimilarity.

A heterogeneous distribution of vegetation enhances the intermittent turbulence, especially during the transition period (Ruppert et al., 2006), since different crops open and close stomata at different times, resulting in a larger heterogeneity of CO_2 and humidity concentration. This process, however, seems to be more important for CO_2 in terms of turbulent variance statistics. Furthermore, Williams et al. (2007) suggested that differences in the source distribution of two scalar fields can result in scalar dissimilarity. Although Hackerott et al. (2017) observed scalar similarity for θ and q, van de Boer et al. (2014) identified dissimilarities among these two scalars for the same BLLAST experiment. Their results are, however, based on data from a different site in which the surface was covered mainly by wheat. They suggested that the ripening of wheat leads to a weaker latent heat flux, so that the similarity functions for humidity become more susceptible to intermittent processes. For these cases, according to de Arellano and Duynkerke (1995), the

analyzed scalar should be considered as scarce, which invalidates the usual flux-gradient relationships.

Entrainment processes can also contribute to the observed dissimilarities. Using the BLLAST radiosondes, van de Boer et al. (2014) showed that the surface layer from 25 to 28 June, and on 5 July, was distinctly affected by entrainment from the free troposphere. Although Hackerott et al. (2017) observed some near-neutral and stable 30-min segments during these days, the convective cases are almost completely rejected by the quality-control process. For the contaminated cases, van de Boer et al. (2014) suggested a correction for the characteristic-scales based on ζ, σ_χ, the boundary-layer height and skewness statistics of the observations.

According to Hackerott et al. (2017), a consequence of scalar similarity in the dissipation term of the variance budget equation is that Eq. (2.18) can be simplified to

$$\frac{N_{\chi_1}}{\chi_{1*}^2} = \frac{N\chi_2}{\chi_{2*}^2}, \tag{2.24}$$

which can be rearranged to indirectly estimate q_* and c_* from their respective dissipation rates and the scaling parameters of θ using

$$|\hat{\chi_{2*}}| = \left| \chi_{1*} \sqrt{\frac{N_{\chi_2}}{N_{\chi_1}}} \right| , \tag{2.25}$$

where the hat indicates the indirect estimate of χ_{2*}.

Equation 2.25 significantly reduces the complexity of the inertial-dissipation method (Högström, 1996), since estimates for $\hat{\chi_{2*}}$ no longer require an iterative method (i.e. Dupuis et al. (1997)). This equation is also helpful in the verification of scalar similarity, as illustrated in Fig. 2.6, where q and c are compared with $\chi_1 = \theta$. In Fig. 2.6a, $|\hat{q}_*|$ is well correlated to $|q_*|$, with $R^2 = 0.94$ considering only convective data, while in Fig. 2.6b, there is only a weak correlation ($R^2 = 0.21$) between $|\hat{c}_*|$ and $|c_*|$, indicating scalar similarity for humidity and temperature, and dissimilarity for temperature and CO_2 concentration.

Another implication of Eq. (2.24) is that the conventional normalization of the power spectrum, as originally proposed by Kaimal et al. (1972), collapses the spectra within the inertial subrange of θ, q and c. It is observed in the examples presented in Fig. 2.7a–c that the non-dimensional power spectra calculated for variances of θ, q and c collapse, while scalar similarity is observed for the dissipation component in these three examples

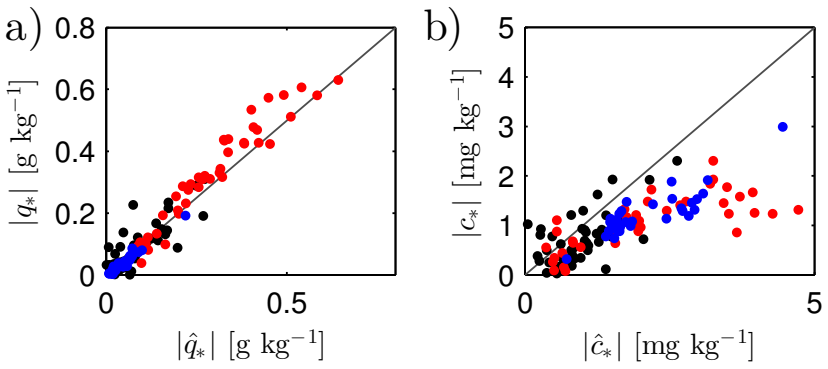

Figure 2.6: Absolute values of the characteristic scales of (a) specific humidity [g kg^{-1}], and (b) specific CO_2 content [mg kg^{-1}], indirectly estimated from the dissipation rates and characteristic scale of virtual potential temperature (ordinate axis) versus that estimated using the eddy-covariance method (abscissa axis) for the BLLAST experiment. The colors indicate the convective (red), near-neutral (black), and stable (blue) regimes. The axes in (b) are limited to 5 mg kg^{-1}. Adapted from Hackerott et al. (2017).

($\Phi_\chi^D \approx 0.30$, $\Phi_\chi^D \approx 0.75$, and $\Phi_\chi^D \approx 0.45$, respectively). The spectra do not collapse in Fig. 2.7d because it is an example of the stable surface layer with considerable variation in the dissipation terms, i.e. $\Phi_u^D = 1.4$, $\Phi_\theta^D = 0.7$, $\Phi_q^D = 2.7$, and $\Phi_c^D = 0.7$.

An implication of scalar similarity in the Φ_χ^D is that Eq. (2.18) can also be re-written as

$$\Phi_{\chi 1}^P + \Phi_{\chi 1}^T = \Phi_{\chi 2}^P + \Phi_{\chi 2}^T \ , \tag{2.26}$$

which implies that the contributions of the production and transport components are the same for the variances of θ, q, and c. Considering the evidence (Dyer, 1974; Hill, 1989; Högström, 1996) that $\Phi_\theta^P = \Phi_q^P$ (i.e. $Pr = Sc$), scalar similarity is also found for the transport terms (i.e. $\Phi_\theta^T = \Phi_q^T$).

2.7 *Modeling of the atmospheric surface layer*

There are three numerical methods to solve turbulence in fluid dynamics: using direct numerical simulation (DNS), using large-eddy simulation (LES) or using the Reynolds-averaged Navier-Stokes equations (RANS). Direct numerical simulation resolves all turbulent scales, including large-scale eddies, eddies occupying the inertial subrange, and those of the Kolmogorov scale where the TKE is dissipated and converted into heat. Large-

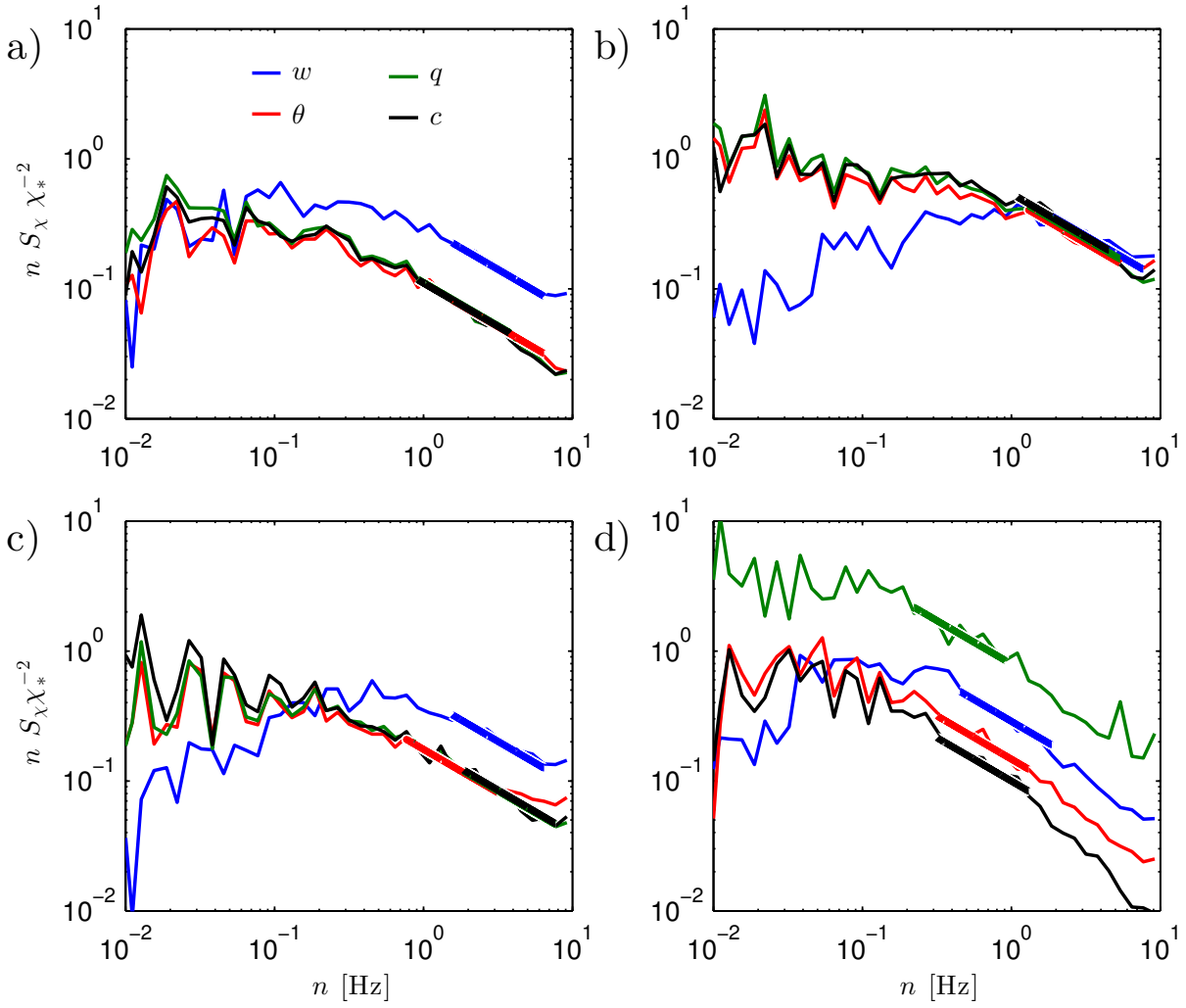

Figure 2.7: Examples of non-dimensional power spectra calculated for the vertical velocity component (blue), virtual potential temperature (red), specific humidity (green), and specific CO_2 content (black), taken during different stability regimes: (*a*) convective ($\zeta = -0.6$); (*b*) slightly stable ($\zeta = 0.08$); (*c*) near-neutral ($\zeta = -0.04$); and (*d*) stable ($\zeta = 0.5$). The thick lines indicate the non-linear $-2/3$ power law fitted within the inertial subrange. Adapted from Hackerott et al. (2017).

eddy simulation explicitly resolves the large turbulent eddies, and parameterizes the high-frequency part of the inertial subrange, making it less computational demanding than DNS. Both LES and DNS, however, are not feasible for operational weather or climate forecast models, whose finest spatial resolutions are currently in the order of a few kilometers, which is the size of only the largest turbulent atmospheric eddies. At present, RANS-based models are the only methods capable of satisfactorily coupling all atmospheric scales. They enable comparison of numerical simulations with real-world observations over large areas, such as the Southwestern Atlantic Ocean.

While there has recently been successful scientific efforts to couple LES to mesoscale models (Moeng et al., 2007; Kirkil et al., 2012; Wyszogrodzki et al., 2012; Talbot et al., 2012; Xie et al., 2015; Rai et al., 2017), all thee studies are confined to small regions (e.g. urban areas). The study of the behavior of the atmospheric surface layer over a whole oceanic basin using LES is still problematic, if not impossible. The problem is not only related to computational issues, but also to the correct interaction between different scales, and to resolve the interactions of different numerical schemes operating with different filters, resolutions, and methods at the subgrid scale (Xie et al., 2015).

In this context, the modeling efforts in this work have concentrated on RANS-based simulations, specifically the Advanced Research Weather, Research and Forecasting (WRF-ARW) model, which is a state-of-the-art supported community mesoscale model [1] (Dudhia, 2014), and may be employed for atmospheric simulations over a wide range of scales.

The detailed description of the WRF-ARW model is available in Skamarock et al. (2008). In summary, the model is a fully-compressible, Eulerian mass non-hydrostatic model with Arakawa C horizontal grid staggering, and terrain-following dry hydrostatic-pressure for the vertical coordinates.

In general, numerical weather prediction models, including the WRF model, have the same dry dynamical equations (Dudhia, 2014) with resolved and unresolved dynamics. The unresolved part has to be parameterized by schemes divisible into six categories:

1. Radiative physics: these handle both long-wave and short-wave radiation, including the solar cycle, the interaction with clouds and aerosols, and radiation fluxes at the surface interface;

2. Unresolved convective column physics: these handle vertical moisture transport by updrafts and downdrafts within convection;

3. Resolved cloud physics: these handle cloud and precipitation processes that include moist phase changes and the associated latent heating;

4. Surface physics: these handle processes that lead to heat and moisture fluxes below and at the interface of the model bottom boundary;

[1] Source code available in `\http://www2.mmm.ucar.edu/wrf/users/`. Accessed in September 2017.

5. PBL physics: these handle the subgrid turbulent transport through all model vertical levels;

6. Surface layer physics: these handle subgrid turbulent transport below the first vertical level of the grid.

The WRF surface-layer-physics scheme has to be linked to its respective PBL physics scheme. The list of all available surface layer schemes in WRF version 3.6.1, with the corresponding references, is presented in Table 2.4.

Table 2.4 - Parameterizations and their abbreviations used for PBL and surface layer (SL) schemes.

PBL and SL schemes	Abbreviation
Yonsei University with MM5 similarity (Hong et al., 2006)	YSU/MM5
Mellor-Yamada-Janjic with Eta similarity (Janjić, 1994)	MYJ/ETA
Quasi-Normal Scale Elimination (Sukoriansky et al., 2005)	QNSE
Mellor-Yamada-Nakanishi and Niino Level 2.5 (Nakanishi and Niino, 2006)	MYNN2
Asymmetric Convective Model with Pleim-Xiu SL scheme (Pleim, 2007)	ACM2
Total Energy Mass Flux (Angevine et al., 2010)	TEMF

According to Dr. Jimy Dudhia[2], the WRF PBL schemes distribute surface fluxes caused by boundary-layer eddies, and allow PBL growth by entrainment. Above the PBL, the schemes also calculate vertical diffusion due to turbulence. The PBL options in the WRF model can be divided into two classes: local closure by TKE prediction (e.g. MYJ, MYNN2, and QNSE) and diagnostic non-local closure (e.g. YSU, ACM2, and TEMF). The non-local PBL schemes have two components: a term for local transport by small eddies and a term for non-local transport by large eddies, which differ between the schemes. The YSU includes a non-gradient term for non-local transport, while the ACM2 and the TEMF schemes include a mass-flux profile (additional updraft flux) for non-local transport. The TKE prediction schemes solve the different terms of the TKE budget equation to determine the local diffusivity. A complete review of the PBL schemes of the WRF model with its advantages and disadvantages is available in the work of Cohen et al. (2015), and also Banks et al. (2016).

The surface layer schemes in the WRF model are based on Monin-Obukhov similarity

[2]Presentation on the NCAS NCAR WRF Tutorial Course at Durham, UK, on 10 October 2017.

theory with similar approaches to estimate the momentum flux over the ocean [3], while using the same iterative scheme to estimate the roughness length and friction velocity, both as a function of the 10 m wind speed. The main difference among the schemes is in the parameterization of the roughness length for heat and moisture.

Although the WRF model can be coupled to wave and ocean models (Warner et al., 2010) for a complete description of air-sea interaction, for simplicity, this study uses the WRF model without these models in simulations. Therefore, the results derived from the WRF model presented here do not account for any wave influences, but only for the SST, which is provided by input data at the surface.

To evaluate the sensitivity of WRF simulations to the SST, two 72-h simulations were performed over the BMC region. The only difference between the two simulations is a warm core eddy, created with a 2-D Gaussian function set to an amplitude of 5°C, which was added to the original SST field, and centered close to the confluence region, as shown in Fig. 2.8. The PBL and surface layer schemes used for the simulations are the YSU and MM5 schemes, respectively.

Figure 2.9 summarizes the experimental results showing the zonal cross-section at 43°S of the average differences in velocity and SST between the two experiments (anomalies). This sensitivity test shows that the simulated wind speed increases proportionally to the increase in SST, and the velocity is rotated to the left as it flows towards the positive SST gradient and to the right over a negative SST gradient. These results are in agreement with climatological studies (e.g. Small et al. (2008); Spall (2007)).

This simple experiment also showed that a small modification to the SST field yields modifications in remote regions, especially for the velocity and pressure fields. The SST used for a boundary condition is often derived from low-resolution datasets, which may induce the propagation of errors to larger scales. This indicates the importance of using re-analysis data for the boundary conditions, and nudging techniques above the PBL when comparing the results of numerical simulations of the atmospheric surface layer with in situ observations.

[3]Personal communication by Dr. Jimy Dudhia during the NCAS NCAR WRF Tutorial Course at Durham, UK, on 10 October 2017.

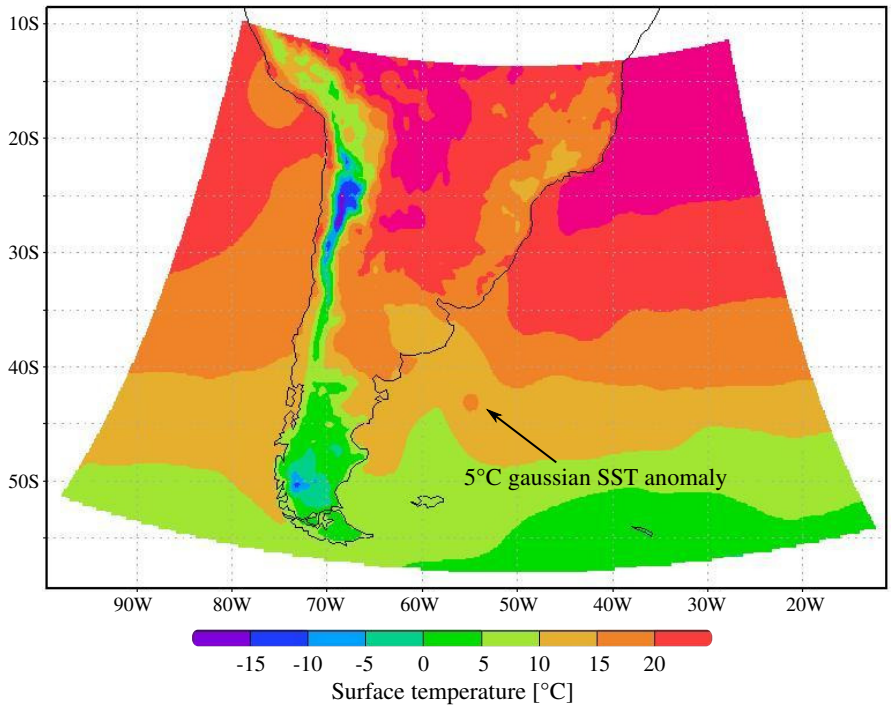

Figure 2.8: Surface temperature [°C] field of the WRF simulation used to test the SST sensitivity.

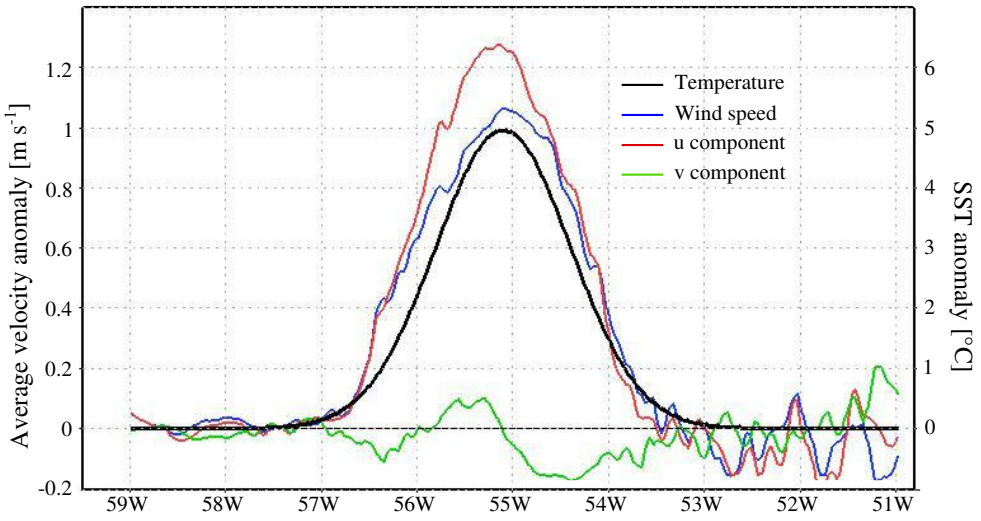

Figure 2.9: Zonal cross-section at 43°S of the difference between the two experiments (anomaly) showing the averaged wind speed (blue), zonal (red) and meridional (green) velocity components [m s^{-1}], and SST [°C] (black).

Chapter 3

Methodology

This Chapter describes the methodology used to derive the turbulent parameters for the INTERCONF campaigns, and is divided into two parts: (1) the methodology used to estimate the turbulent parameters from in situ observations (Sects. 3.1 to 3.4) and (2) the methodology used to derive the turbulent parameters from numerical simulations (Sect. 3.5).

3.1 In situ observations

A micrometeorological tower was mounted on the bow of the Polar Ship Almirante Maximiano H-41, which is operated by the Brazilian Navy. In situ observations were collected during three field campaigns ranging from Rio Grande (Southern Brazil) to Ushuaia (Southern Argentina) in the periods 14 to 20 October 2013 (OP32), 17 to 23 October 2014 (OP33) and 10 to 19 October 2015 (OP34). The ship tracks for each campaign are illustrated in Fig. 3.1, and are overlaid on the SST field in the region, which highlights the intense along-the-track SST gradients caused by the presence of the BMC.

The ship and instrumentation set-up chosen for the OP32, OP33, and OP34 campaigns are shown in Fig. 3.2. The set-up for OP34 is slightly different, with two sonic anemometers vertically aligned and the mast mounted on a higher platform. The velocity [m s^{-1}] and sonic temperature [°C] were collected at a sampling frequency of 20 Hz by a 3-D sonic anemometer CSAT 3 installed at 15 m above the mean sea-surface-level during the OP32 and OP33 campaigns, and at 12.2 m above the mean sea-surface-level during the OP34 campaign. The sonic temperature is assumed to be equal to the virtual potential temperature, hereafter defined as θ. The ship motion was measured by an inertial motion

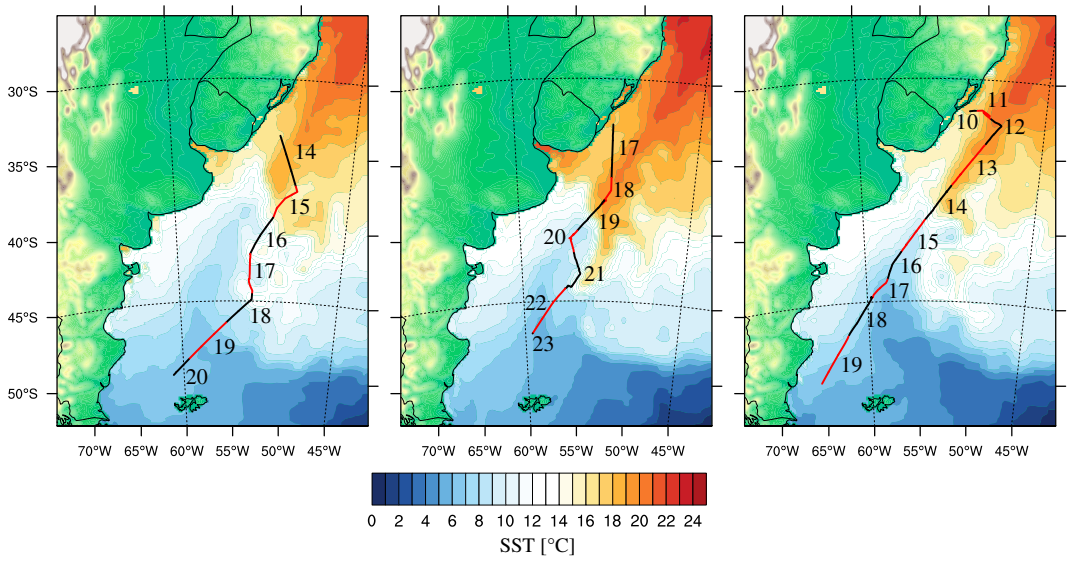

Figure 3.1: Cruise routes for OP32 (left), OP33 (middle), and OP34 (right). The route colors (black and red) indicate different days and the numbers are the days of October of the respective year (2013, 2014 and 2015). The shaded colors over the ocean indicate the sea surface temperature [°C] estimated from the 15 km grid interpolation of the NCEP Climate Forecast System Analysis 2, for 16 October 2013 00Z (left), 20 October 2014 00Z (middle) and 13 October 2015 00Z (right). The shaded colors over the continent indicate the topography height ranging from sea level (green) to 3 km (white).

unit (IMU) known as the Motion Pack III, which was also installed on the mast, near the flux measurement systems (1.36 m for the OP32 and OP33 campaigns, and 4.4 m for the OP34 campaign).

3.1.1 Data quality control

All in situ observations were first checked for outliers and divided into 20-min half-overlapping segments. Foken et al. (2005) suggest that spikes are values outside the range of approximately four times the standard deviation of a segment. As this range was observed to be too low here, it was increased to five standard deviations. In addition, Foken et al. (2005) classify values as spikes when they lay outside the physically reasonable range. The corresponding physical limits used in this work are shown in Table 3.1. Based on this quality-control algorithm, segments with more than 100 spikes are discarded. Spikes within accepted segments are replaced by a linear interpolation of the neighboring data.

The lower and upper limits for the vertical velocity component have to be relatively large compared with the measurements taken over land or a stable platform, since the ship motion induces rapid vertical motion, which easily reaches 10 to 15 m s^{-1}.

Figure 3.2: Photograph of the Polar Ship Almirante Maximiano H-41 taken in October 2014 (left) and instrumentation set-up for both the OP32 and OP33 campaigns (upper right), and for the OP34 campaign (lower right), showing the two sensors used in this work: the IMU Motion Pack III and the sonic anemometer CSAT 3.

Table 3.1 - Physical limits chosen for the basic spike detection.

Sensor and variable	Lower limit	Upper limit
CSAT3 - *horizontal velocities* [m s^{-1}]	-50	50
CSAT3 - *vertical velocity* [m s^{-1}]	-20	20
CSAT3 - *virtual temperature* [°C]	-10	30
IMU - *accelerations* [m^2 s^{-1}]	-50	50
IMU - *angular velocities* [rad s^{-1}]	-1	1
GPS - *ship heading* [°]	0	360
GPS - *ship velocity* [m s^{-1}]	0	20

3.1.1.1 Motion correction

The contamination induced by the ship motion in the velocity dataset has also to be removed, or largely reduced, before the calculation of fluxes (Edson et al., 1998; Huang et al., 2013; Prytherch et al., 2015). Although the inertial subrange may be considered isotropic and, therefore, invariant to the platform motion, the increased energy at the motion-affected frequency band may induce anisotropy, which appears as a source of noise. Thus, the whole spectrum is modulated and, as a consequence, the dissipation rates and the flux estimates become biased (Bakhoday Paskyabi et al., 2013).

This work used the algorithm proposed by Miller et al. (2008) to estimate the platform velocity vector, which uses the angular velocities and accelerations measured by the IMU, together with the ship heading and velocity registered by the GPS. The IMU sensor (Fig. 3.3) measures the angular velocities $\mathbf{\Omega}_p$ [rad s^{-1}] and the accelerations $\ddot{\mathbf{x}}_p$ [m s^{-2}] in the platform's coordinate system defined by the orthonormal basis $\{\mathbf{x}_p, \mathbf{y}_p, \mathbf{z}_p\}$. It is worth mentioning that the IMU coordinate system was originally different from the one described in the instrument manual. A laboratory experiment led by Dr. Marcelo Santini had to be consequently performed at the Laboratório de Integração e Testes of the National Institute for Space Research using a controlled rotation table to identify the correct coordinate axis.

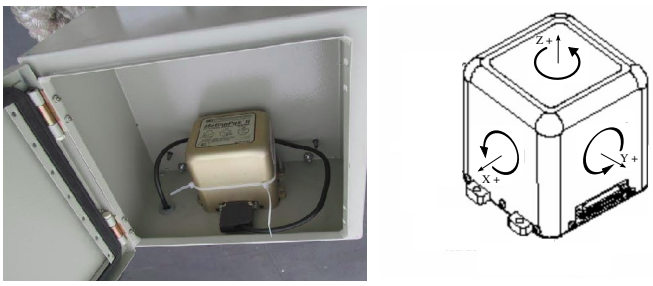

Figure 3.3: Photograph of the IMU Motion Pack III and a schematic diagram of the coordinate axes.

The platform coordinate system is defined here in the right-hand orientation, with $\mathbf{x}_p$ pointing to the bow, $\mathbf{y}_p$ to the port side and $\mathbf{z}_p$ upward, according to Fig. 3.4. The Eulerian angles, which represent the rotation around each axis, are also defined in a right-hand orientation, where the roll (Φ) is the rotation angle around $\mathbf{x}_p$, the pitch (Θ) is the rotation angle around $\mathbf{y}_p$ and the yaw (Ψ) is the rotation angle around $\mathbf{z}_p$.

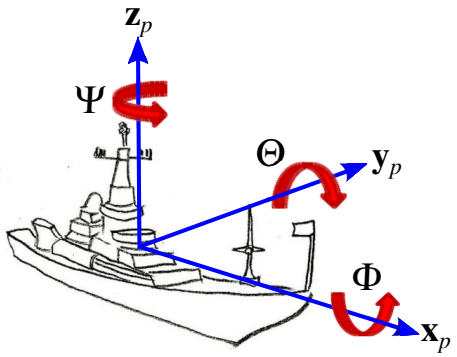

Figure 3.4: Schematic diagram of the ship coordinate system and the Eulerian angles: roll (Φ), pitch (Θ), and yaw (Ψ).

According to Miller et al. (2008), the true velocity vector $\mathbf{V}_{true}$ of the air flow is expressed as the sum of the velocity vector measured by the sonic anemometer $\mathbf{V}_{sonic}$, in the Earth coordinate system, and the platform motion velocity, which in turn is defined as the sum of the ship velocity vector ($\mathbf{V}_{ship}$), the platform velocity vector ($\mathbf{V}_p$) and the anemometer rotation velocity vector ($\mathbf{V}_{rot}$),

$$\mathbf{V}_{true} = \mathbf{T}\ \mathbf{V}_{sonic} + [\mathbf{V}_{ship}]_{lp} + \mathbf{T}\ [\mathbf{V}_p]_{hp} + \mathbf{T}\ [\mathbf{V}_{rot}]_{hp}, \tag{3.1}$$

where the subscripts *lp* and *hp* indicate whether a low-pass or a high-pass filter is applied. Here, $\mathbf{T}$ is the transformation matrix that enables the change from the platform coordinate system to the Earth's coordinate system, which is defined as the multiplication of the three rotation matrices,

$$\mathbf{T} = \begin{bmatrix} \cos\Psi & -\sin\Psi & 0 \\ \sin\Psi & \cos\Psi & 0 \\ 0 & 0 & 1 \end{bmatrix} \begin{bmatrix} \cos\Theta & 0 & \sin\Theta \\ 0 & 1 & 0 \\ -\sin\Theta & 0 & \cos\Theta \end{bmatrix} \begin{bmatrix} 1 & 0 & 0 \\ 0 & \cos\Phi & -\sin\Phi \\ 0 & \sin\Phi & \cos\Phi \end{bmatrix}. \tag{3.2}$$

It was assumed that all measurements were collected in the same coordinate system, which is the platform coordinate system. Also, the order of the rotation matrices $\mathbf{T} = \mathbf{T}(\Psi)\mathbf{T}(\Theta)\mathbf{T}(\Phi)$ was carefully chosen to be $\Psi \rightarrow \Theta \rightarrow \Phi$ to reduce the transformation sensitivity.

In Eq. (3.1), $\mathbf{V}_{ship}$ is estimated from the ship position measured by the GPS at a low sampling frequency (1 Hz). The values of $\mathbf{V}_p$ and $\mathbf{V}_{rot}$ are estimated from the data collected by the IMU using

$$\mathbf{V}_p = \int \ddot{\mathbf{x}}_p dt \tag{3.3}$$

and

$$\mathbf{V}_{rot} = \mathbf{\Omega}_p \times \mathbf{r}, \tag{3.4}$$

respectively, where $\mathbf{r}$ is the position vector [m] from the IMU to the anemometer, $\mathbf{r} = [1.0,\ 0.0,\ -4.3]$ for the OP34 campaign and $\mathbf{r} = [1.2,\ 0.4,\ 0.5]$ for the OP32 and OP33 campaigns.

The Eulerian angles are estimated by a combination of two different estimates, which yields a complementary filtering technique. The two estimates use:

1. the rotation rates measured by the IMU with a high-pass filter:

$$\begin{bmatrix} \Phi \\ \Theta \\ \Psi \end{bmatrix}_{hp} = \left[\int \mathbf{\Omega}_p dt \right]_{hp}. \tag{3.5}$$

2. the accelerations measured by the IMU with a low-pass filter:

$$\begin{bmatrix} \Phi \\ \Theta \\ \Psi \end{bmatrix}_{lp} = \begin{bmatrix} \tan^{-1}\left(\frac{\ddot{y}_p}{g}\right) \\ \tan^{-1}\left(-\frac{\ddot{x}_p}{g}\right) \\ \Psi_{GPS} \end{bmatrix}_{lp}, \tag{3.6}$$

where the acceleration due to gravity is calculated as $g = \sqrt{\ddot{x}_p^2 + \ddot{y}_p^2 + \ddot{z}_p^2}$, and Ψ_{GPS} is the ship heading measured by the GPS, converted to a counter-clockwise rotation direction.

A complementary filtering procedure is, therefore, required in Eqs. (3.1), (3.5), and (3.6). Miller et al. (2008) suggest a fourth-order Butterworth filter for which a cut-off period is supplied as the input. The combination of low- and high-frequency measures are important because of the inherent drift in the rate estimates (Edson et al., 1998; Fer and Bakhoday Paskyabi, 2014; Flügge et al., 2016).

The method used to estimate the cut-off period is the one described by Fer and Bakhoday Paskyabi (2014) and Flügge et al. (2016), and is a method of trial and error whereby the root-mean-squared values of $[\Phi]_{hp}$, $[\Theta]_{hp}$, $[\Psi]_{hp}$, $[\Theta]_{lp}$, and $[\Phi]_{lp}$ are tested for cut-off periods between 5 and 35 s. Analysis of the statistical evolution for different cut-off periods (Fig. 3.5) suggests that a cut-off period of 22 s is sufficient to separate the low-frequency tilts from the wave-induced frequency band in the range from 10 to 17 s, which dominates the tilting motion estimated from the accelerations ($\ddot{x}_p$, $\ddot{y}_p$, and g) in Eq. (3.6).

The motion-correction algorithm successfully reduces the effect of ship motion on the velocity dataset, mainly within the frequency range between 0.09 and 0.3 Hz, Fig. 3.6. Here, the averaged vertical velocity power spectrum and co-spectrum of longitudinal and vertical velocity components, considering the 187 accepted 20-min segments, for the uncorrected dataset (red) are compared with the corrected one (blue). The differences observed in the low-frequency range are mainly caused by the vertical alignment correction of the coordinate system to the gravity vector, while the differences observed in the high-frequency

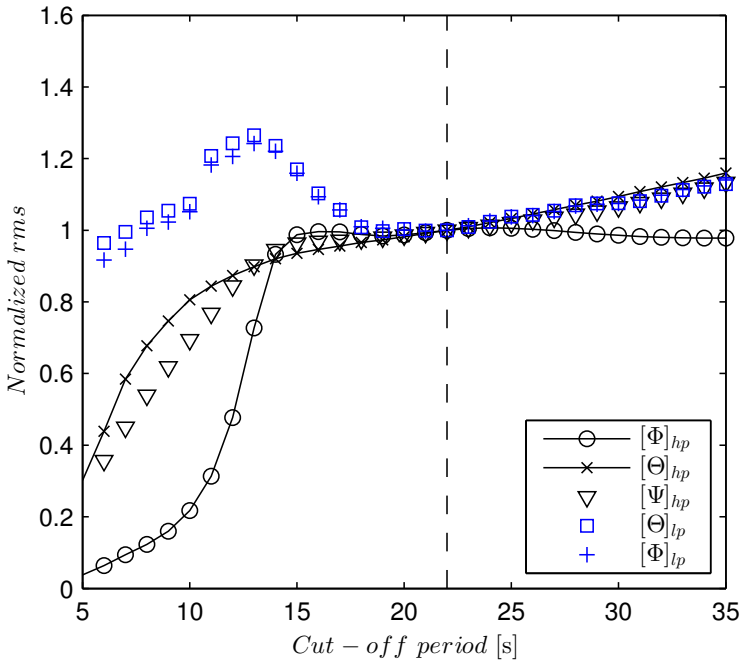

Figure 3.5: Influence of the cut-off period filter on the statistics of the Eulerian angles estimated according to Eq. (3.5) and Eq. (3.6). The root-mean-squared angles for each 20-min segment were averaged for all accepted segments and normalized by the respective value corresponding to a cut-off period of 22 s, which is identified by the dashed line.

range are mainly caused by the anisotropy noise produced by the increased energy at the motion-affected frequency band (Bakhoday Paskyabi et al., 2013). Despite all difficulties involved in collecting high-frequency velocity data on the open ocean, from a moving ship, the curves reasonably follow the theoretically predicted $-\frac{5}{3}$ slope for the spectra (Fig. 3.6a) and $-\frac{7}{3}$ slope for the co-spectra (Fig. 3.6b) within the inertial subrange.

3.1.1.2 Data assessment for turbulence statistics

In addition to the despiking and motion-correction algorithms, the sonic anemometer dataset also undergoes an automated quality-control for turbulence statistics, which tests each segment for flow-distortion, non-stationarity, or the failure of Taylor's hypothesis (Stull, 1988). With the exception of the flow-distortion test, the velocity data are rotated into the streamwise direction (i.e. $\overline{v} = \overline{w} = 0$) following Lee et al. (2005). Also, Taylor's hypothesis is evaluated without removing the ship's velocity from the wind velocity in the motion correction algorithm.

According to Lee et al. (2005), the streamwise velocity vector ($\mathbf{V}_{stream}$) can be calcu-

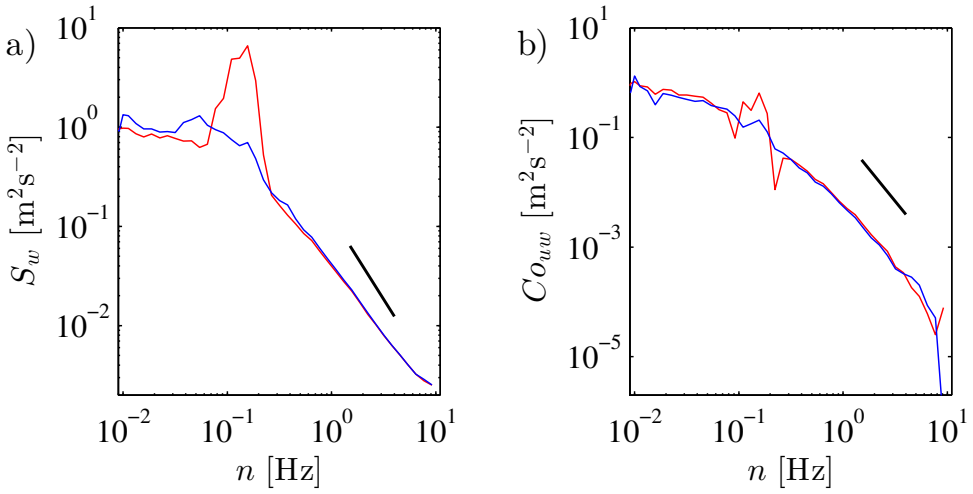

Figure 3.6: Averaged power spectrum of vertical velocity (a) and co-spectrum of longitudinal and vertical velocities (b), considering all accepted 20-min segments before (red) and after (blue) the platform motion correction. The short dark lines are indicate the $-\frac{5}{3}$ slope (a) and $-\frac{7}{3}$ slope (b), used to identify the inertial subrange.

lated using

$$\mathbf{V}_{stream} = \begin{bmatrix} u\frac{\overline{u}}{\sqrt{\overline{u}^2+\overline{v}^2+\overline{w}^2}} + v\frac{\overline{v}}{\sqrt{\overline{u}^2+\overline{v}^2+\overline{w}^2}} + w\frac{\overline{w}}{\sqrt{\overline{u}^2+\overline{v}^2+\overline{w}^2}} \\ v\frac{\overline{u}}{\sqrt{\overline{u}^2+\overline{v}^2}} - u\frac{\overline{v}}{\sqrt{\overline{u}^2+\overline{v}^2}} \\ w\frac{\sqrt{\overline{u}^2+\overline{v}^2}}{\sqrt{\overline{u}^2+\overline{v}^2+\overline{w}^2}} - u\frac{\overline{u}\ \overline{w}}{\sqrt{\overline{u}^2+\overline{v}^2}\sqrt{\overline{u}^2+\overline{v}^2+\overline{w}^2}} - v\frac{\overline{v}\ \overline{w}\sqrt{\overline{u}^2+\overline{v}^2}}{\sqrt{\overline{u}^2+\overline{v}^2+\overline{w}^2}} \end{bmatrix}. \tag{3.7}$$

The stationarity test is based on the methodology described by Foken et al. (2005) in which the covariances $\overline{w'u'}$ and $\overline{w'\theta'}$ are calculated for each 5-min segment, and then compared with the covariance calculated for the original 20-min segment. The data segment is flagged as accepted if all 5-min covariances differ by less than 30% of the 20-min covariance for $\overline{w'u'}$ (minimum requirement defined by Foken et al. (2005)) and by less than 50% for $\overline{w'\theta'}$. The limit for $\overline{w'\theta'}$ is chosen as 50% instead of 30% to retain more acceptable segments, which were also visually inspected and accepted.

The flow-distortion is evaluated by a combination of three tests: the angle-of-attack test (Fer and Bakhoday Paskyabi, 2014), the distorted-sector test (Li et al., 2013), and the acceptable tilt-angle test. The first test flags segments in which the vertical angle-of-attack of the flow is greater than 5° compared with the horizontal plane. The second test evaluates the horizontal angle-of-attack of the flow, where the segments are flagged if the flow is measured from a sector between 70° and 200° anti-clockwise from the bow for the OP32 and OP33 campaigns, and between 150° and 200° for the OP34 campaign. The

acceptable tilt-angle test consists in the evaluation of the mean ship roll in the segment, whereby time-series are flagged if the ship is tilted side-ward by more than 2° on average.

A comparison among all quality-control tests for turbulence statistics is illustrated in Fig. 3.7. The stationarity test for the streamwise velocity component is the most restrictive test, discarding about 75% of the dataset, with the flagging not biased toward any particular region of the Southwestern Atlantic Ocean. After all quality-control tests, 187 20-min averaged half-overlapped segments are finally accepted, which represents only 6% of the original dataset.

Finally, Fig. 3.8 presents the time-series of all accepted (black dots) 20-min-averaged segments considering all parameters used in this work: wind speed, virtual potential temperature, and H_s. The rejected segments (gray) are also displayed for comparison purposes. Also shown is the SST (red line), which is estimated as the 20-min-averaged temperature registered by the thermosalinograph installed at 5 m depth, approximately, to identify the confluence region. The accepted dataset is well distributed over both sides of the BMC (warm and cold regions), covering a wide range of atmospheric and sea conditions. The methodology used to estimate the significant wave height will be further described in Sect. 3.5.

3.2 Turbulence analysis of the MASL

The atmospheric surface layer is often described in the context of the TKE budget equation (see Sect. 2.4), as expressed by Eq. (2.17), which assumes that the vertical momentum fluxes are constant with height within the atmospheric surface layer under stationary and homogeneous conditions, with both negligible vertical mesoscale motions and molecular diffusion, and with the coordinate system aligned to the mean wind direction following Eq. (3.7).

The scaling parameters u_* and θ_* were estimated using the eddy-covariance method according to Eqs. (2.4) and 2.5, but which may also be estimated using the inertial dissipation method (Högström, 1996). Pan et al. (2005) demonstrated, however, that this method produces results different from the eddy-covariance method due to the effect of a swell-related modification of the drag coefficient, which is not taken into account in the inertial dissipation method. In addition, Donelan et al. (1997) point out that the

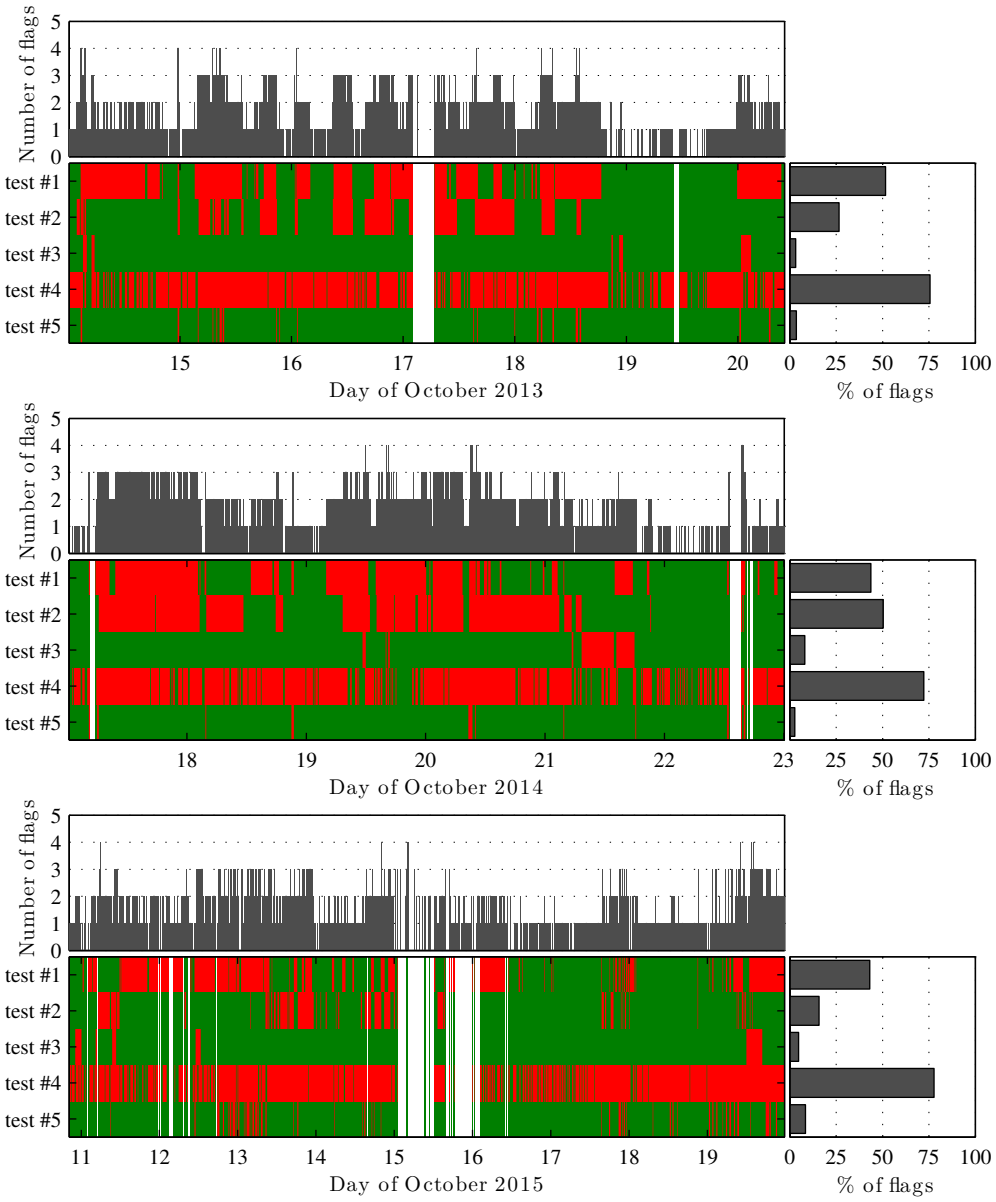

Figure 3.7: Time-series of segments discarded by the different tests marked in red in the bottom panels: flow angle-of-attack (test #1), horizontal distorted-sector (test #2), tilt-angle (test #3), stationarity (test #4), and Taylor's hypothesis (test #5). The histograms indicate the number of red flags for each 20-min segment (upper panel) and the percentage of removed segments by each test (right panel), for the three campaigns of the INTERCONF project.

inertial dissipation method is not suitable for estimating the friction velocity under the nonequilibrium wave conditions expected to be frequent in the INTERCONF dataset, resulting from the energetic nature of the confluence region. This observation was also reinforced by Drennan et al. (1999).

As it was not possible to estimate the vertical derivatives in Eq. (2.17) because the wind speed was measured at a single height, the production term Φ^P was parameterized

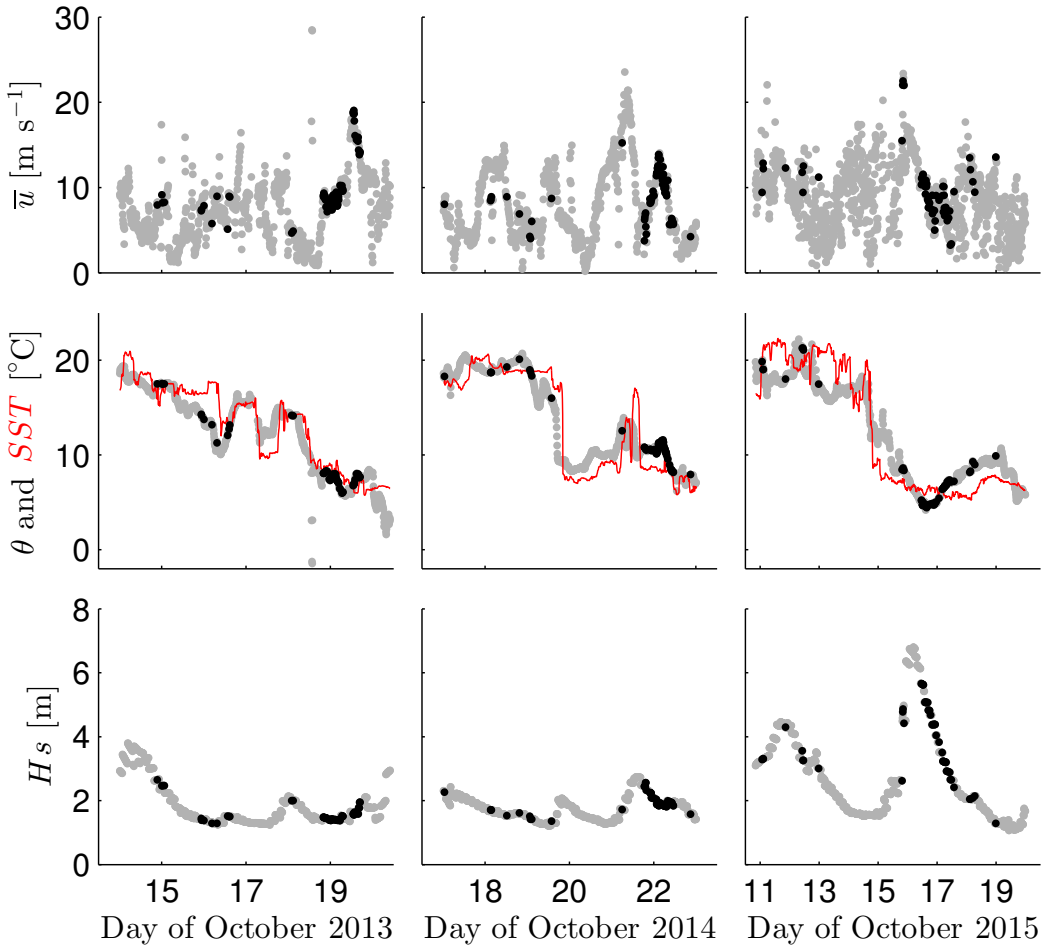

Figure 3.8: Time-series of wind speed [m s^{-1}], sea-surface (red line) and virtual potential temperature [°C] and significant wave height [m], for three campaigns of the INTERCONF project. The black dots are the accepted 20-min segments after quality testing of the turbulence statistics.

by the functions described by Högström (1996), Eq. (2.19), and the total non-dimensional transport of TKE Φ^T, which was assumed as the sum of the vertical transport of TKE and divergence of pressure transport, and estimated as a residual term.

The dissipation term Φ^D was estimated from the dissipation rate of TKE ϵ according to the methodology described in Sect. 2.3, which uses a non-linear fit of Eq. (2.11) in the inertial subrange of the power spectrum of the vertical velocity component for a time interval of 15 min, with data collected at 20 Hz, and centered within the 20-min segment. The limits of the inertial subrange are estimated according the methodology described in Sect. 2.3.1.

3.3 Momentum flux and drag coefficient

The drag coefficient at a reference height of 10 m (C_{D10}) is historically used as the variable to relate the momentum flux to standard parameters of the mean flow (Garratt, 1994), such as the 10-m mean wind speed ($\overline{u_{10}}$). In the context of Monin-Obukhov similarity theory, combining Eq. (2.1) with Eq. (2.4) enables the momentum flux to be expressed by the following bulk relationship,

$$\frac{\tau}{\rho} = \overline{u'w'} = u_*^2 = C_{D10}\overline{u_{10}}^2 \ . \tag{3.8}$$

For both parameterization and simplicity purposes, the bulk formulations are often stated for neutral conditions, C_{DN10} and $\overline{u_{N10}}$. For example, Garratt (1977) proposed the following expression for C_{DN10}

$$C_{DN10} = (0.75 + 0.067\ \overline{u_{N10}}) \times 10^{-3}. \tag{3.9}$$

This formulation is similar (of the same order of magnitude) to others, such as the COARE 3.5 algorithm (Edson et al., 2013) and the one proposed by Large and Pond (1981), and, therefore, the comparisons presented here are based on Eq. (3.9).

To estimate $\overline{u_{N10}}$, Andreas et al. (2012) suggested a correction for stability effects of $\overline{u}$ measured within the atmospheric surface layer,

$$\overline{u_{N10}} = \overline{u} - \frac{u_*}{\kappa}\left[ln\frac{z}{10} - \psi^P(\zeta)\right] \ , \tag{3.10}$$

where ψ^P is the integrated stability function $\Phi_u^P(\zeta)$ (Eq. (2.19)), which is expressed as

$$\psi^P(\zeta) = \begin{cases} 2\ ln\left[\frac{1+x^{-1}}{2}\right] + ln\left[\frac{1+x^{-2}}{2}\right] - 2\ tan^{-1}x^{-1} + \frac{\pi}{2}\ , & \zeta \leq 0 \\ -5.3\zeta\ , & \zeta > 0 \end{cases} \tag{3.11}$$

where $x = (1 - 19\zeta)^{-\frac{1}{4}}$.

Besides the drag coefficient, the aerodynamic roughness length z_0 is also an important parameter for air–sea interaction studies and bulk formulations, and is defined as the height where the theoretical logarithmic wind-speed profile is zero. This profile formulation is derived from the integration of Φ_u^P in Eq. (2.17) for neutral conditions ($\zeta = 0$) so that Eq. (2.19) assumes the form $\Phi_u^P = 1$, giving the logarithmic profile as

$$\overline{u_N}(z) = \frac{u_*}{\kappa} ln\left(\frac{z}{z_0}\right) \ , \tag{3.12}$$

which is also known as the law of the wall.

From Eq. (3.12), z_0 can be estimated for the reference level of 10-m height by

$$z_0 = 10 \ e^{-\kappa \frac{\overline{u_{N10}}}{u_*}} \ . \tag{3.13}$$

In bulk parameterizations, z_0 is often expressed as a function of u_* and the Charnock constant $\alpha_c = 0.016$ (Garratt, 1994),

$$z_0 = \alpha_c \frac{u_*^2}{g} \ , \tag{3.14}$$

which has the disadvantage that the value of α_c may considerably vary during swell conditions (García-Nava et al., 2009).

3.4 Uncertainty of the estimates

The scaling parameters θ_* and u_* were estimated using the eddy-covariance method, whose uncertainties are expected to be lower than 30% of the estimated value (Rannik et al., 2016) when applying the restrictive quality control for turbulence statistics described in Sect. 3.1.1.2. Therefore, it was assumed that $\epsilon_{u_*} = 0.3u_*$ and $\epsilon_{\theta_*} = 0.3\theta_*$.

Andreas et al. (2012) showed that the expression for $\overline{u_{N10}}$ (Eq. (3.10)) has a very weak built-in correlation with u_* if the measurements have been recorded not far from a height of 10 m and in near-neutral stratification. Therefore, $\epsilon_{\overline{u_{N10}}} \approx \epsilon_{\overline{u}}$, and as a consequence, $\epsilon_{C_{DN10}} \approx \epsilon_{C_D}$. The comparison between $\overline{u}$ and C_D, with their respective estimates for the neutral regime at a 10-m height shown in Fig. 3.9, indicates no significant differences. Therefore, it was assumed that the uncertainties related to other error sources, such as the methodology used to estimate the characteristic scales (eddy-covariance method), were much larger than the uncertainty related to the stability and height corrections. In this context, the instrumentation errors (i.e. $\epsilon_{\overline{u}}$ and $\epsilon_{\overline{\theta}}$) were assumed to be negligible.

The uncertainty of ϵ is not as well documented as it is for the characteristic scales, however, it was observed that the estimates of ϵ for 10-min half-overlapping segments within a 20-min segment window, vary less than 10%. Thus, this value was assumed as an appropriate estimation for σ_ϵ.

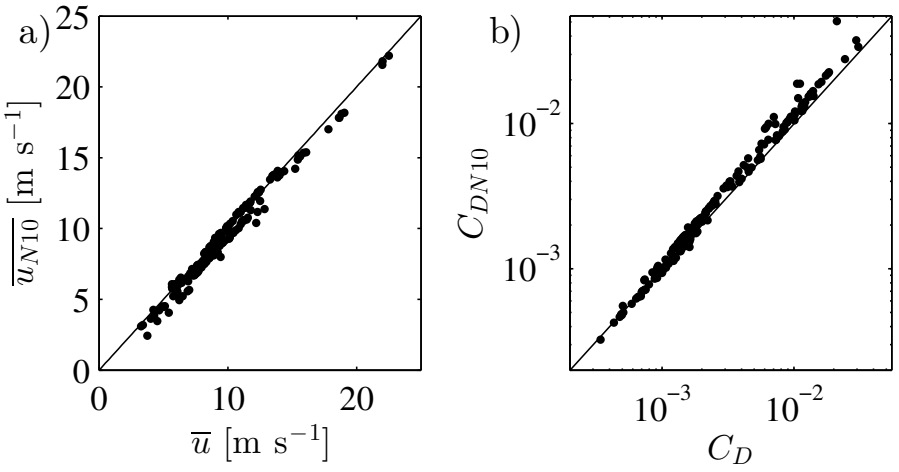

Figure 3.9: Comparison between the averaged wind speed (a) and drag coefficient (b) estimated with and without both the stability and height corrections.

The errors ϵ_{u_*}, ϵ_{θ_*}, and ϵ_ϵ propagate to the other variables estimated here according to

$$\epsilon_{X(x_1,x_2,...,x_n)} = \sqrt{\left(\epsilon_{x_1}\frac{\partial X}{\partial x_1}\right)^2 + \left(\epsilon_{x_2}\frac{\partial X}{\partial x_2}\right)^2 + ... + \left(\epsilon_{x_n}\frac{\partial X}{\partial x_n}\right)^2} \quad , \tag{3.15}$$

where $X(x_1,x_2,...)$ is a parameter estimated from the variables x_1,x_2,...,x_n. Therefore, the errors for ζ, Φ^D, and Φ^P derived in Eqs. (2.17) and (2.19) are

$$\epsilon_{\zeta(u_*,\theta_*)} = \sqrt{\left(\epsilon_{\theta_*}\frac{\kappa z g}{\theta u_*^2}\right)^2 + \left(\epsilon_{u_*}\frac{2\kappa z g \theta_*}{\theta u_*^3}\right)^2} \quad , \tag{3.16}$$

$$\epsilon_{\Phi^D(u_*,\epsilon)} = \sqrt{\left(-3\epsilon_{u_*}\frac{\kappa z \epsilon}{u_*^4}\right)^2 + \left(\epsilon_\epsilon\frac{\kappa z}{u_*^3}\right)^2} \tag{3.17}$$

and

$$\epsilon_{\Phi^P(\zeta)} = \begin{cases} \sqrt{\left(\epsilon_\zeta \frac{19}{4}(1-19\zeta)^{-\frac{5}{4}}\right)^2}, & \zeta \leq 0 \\ \sqrt{(5.3\epsilon_\zeta)^2}, & \zeta > 0 \end{cases} \tag{3.18}$$

Since the transport term was estimated as $\Phi^T = \Phi^P - \zeta - \Phi^D$, then

$$\epsilon_{\Phi^T(\Phi^P,\Phi^D,\zeta)} = \sqrt{(\epsilon_{\Phi^P})^2 + (\epsilon_{\Phi^D})^2 + (\epsilon_\zeta)^2} \quad . \tag{3.19}$$

For C_{DN10} and z_0, the errors are

$$\epsilon_{C_{DN10}(u_*)} = \sqrt{\left(2\epsilon_{u_*}\frac{u_*}{\overline{u_{N10}}^2}\right)^2} \tag{3.20}$$

and

$$\epsilon_{z_0(u_*)} = \sqrt{\left(\epsilon_{u_*} \frac{10\kappa\overline{u_{N10}}}{u_*^2} e^{-\kappa\frac{\overline{u_{N10}}}{u_*}}\right)^2} \quad , \tag{3.21}$$

respectively.

3.5 Numerical simulations

This section describes all numerical simulations used in this work, which can be divided into two groups: global models and regional models. The first group is used for validation and reference purposes, while the second group is used to test different atmospheric surface layer schemes.

All model results were taken from grid points interpolated to the ship coordinates using the same methodology, which is a linear interpolation in time and space.

3.5.1 Global models

Two global models operated by the National Centers for Environmental Prediction (NCEP) were used, the WAVEWATCH III® model and the Climate Forecast System Version 2 (CFSv2) model.

The wave parameters used here are estimated from the wave hindcast product of the WAVEWATCH III® model, operated by NOAA/NWS/NCEP at a 30 arc-minute global grid resolution for 3-h intervals. For comparison purposes, the model dataset is linearly interpolated in time and space to the ship coordinates.

The numerical results from WAVEWATCH III® for Hs were compared with that estimated as four times the standard deviation of the vertical ship displacement measured from the IMU data for a 20-min segment (Fig. 3.10).

Although the comparison showed a good level of agreement (R^2=0.7), it was decided to use only the wave parameters estimated from the WAVEWATCH III model because the in situ method is able to only capture the most energetic and large waves, due to the ship size (93.4 m length) and weight (3,865 t of gross tonnage). In other words, the ship inertia could induce higher displacement than what would be observed if the ship followed exactly the wave curvature. Therefore, accurate values of the wave height estimated from the IMU dataset should not be expected, but rather the tendencies of either increasing or decreasing wave heights.

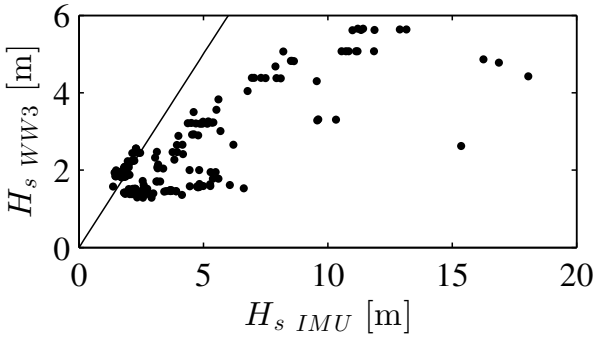

Figure 3.10: Comparison between the significant wave height estimated using the IMU dataset and that using the WAVEWATCH III® model results.

The simulations of inverse wave age (simulated 10 m wind speed, u_{10}, divided by the phase speed at the primary wave mean period, c_p) in Fig. 3.11 show that the majority (85%) of the analyzed dataset was collected during the swell conditions, i.e. $\frac{\overline{u_{10}}}{c_p} < 0.83$ (Donelan et al., 1993; Bakhoday Paskyabi and Fer, 2014).

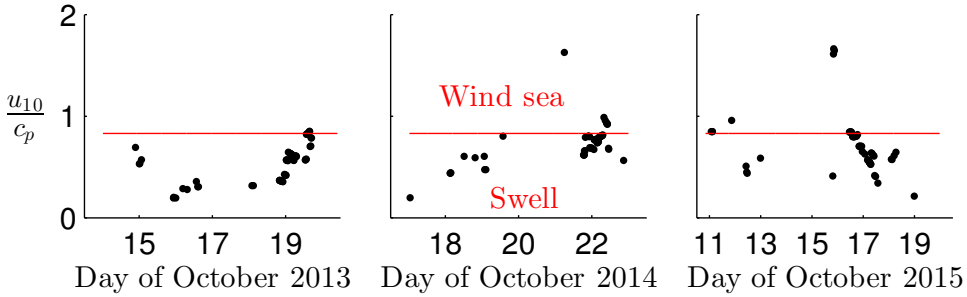

Figure 3.11: Time series of the inverse wave age estimated for the analyzed dataset from the WAVEWATCH III® model. The red line is the separation between swell and wind sea.

A preliminary analysis of the turbulent parameters estimated in this work, considering for the diagnosis of both the inverse wave age and the significant wave height of the combined wind sea and swell (H_s), showed no visual relation between the wave age and the analyzed parameters. On the other hand, a considerable influence of H_s on the estimated turbulent parameters was observed, and therefore, only H_s is used for diagnosis, from which two wave regimes are defined: $H_s \geq 2.5$ m and $H_s < 2.5$ m. The first represents 30% of the dataset used here.

The CFSv2 model was used for two purposes: validation of the friction-velocity estimates and the boundary conditions for the regional models. This is a re-analysis product processed by a fully-coupled atmosphere–ocean–land model provided by NCEP since March

2011 at a 0.5° resolution for 1-h intervals. The detailed model description is available in Saha et al. (2014).

3.5.2 Regional models

This work used the regional model WRF version 3.6.1 (Skamarock et al., 2008) with boundary conditions from the CFSv2 model (i.e. initial conditions and lateral boundary) updated at 1-h intervals. The model was configured with different surface layer schemes to evaluate different representations of the atmospheric surface layer.

The model was configured with a single domain large enough to cover all ship routes. The domain size was intentionally small to retain the large scale as close as possible to the CFSv2 model. It was set to 155 points in the x, 250 points in the y, and 50 points in the z direction, with a 12×12 km horizontal gridspacing, and 60-s time-step. A Lambert conformal conic projection is used, with standard longitude set to $-15°$ and a standard parallel set to $-40°$ and $-45°$. This projection enabled a domain best aligned with the ship routes, as shown in Fig. 3.12.

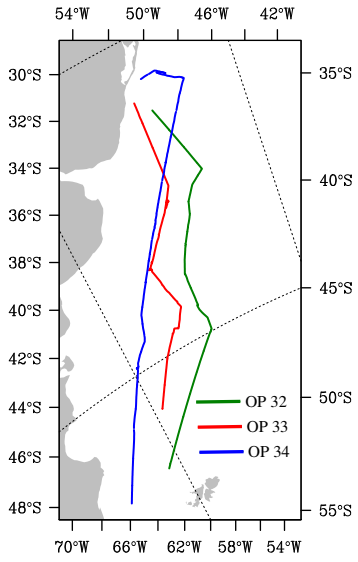

Figure 3.12: Area covered by the WRF model domain with the INTERCONF campaign routes.

The vertical levels in the WRF model are distributed on a terrain-following hydrostatic-

pressure vertical coordinate (η) defined as

$$\eta = \frac{p - p_t}{p_s - p_t}, \tag{3.22}$$

where p is the atmosphere pressure at the chosen height, $p_t = 50$ hPa is the pressure along the model top boundary, and p_s is the pressure along the model surface boundary.

The lowest η level was set to 0.995, which is equivalent to a height between 20 and 40 m. The vertical levels were configured to include 17 levels logarithmically distributed below $\eta = 0.8$, which is approximately a height of 1 km, and the remaining levels with a distribution limited to a maximum of width of 2 km, with 10 levels above $\eta = 0.2$ (at approximately 10 km). This set-up was chosen so as to best agree with the conclusions of recent publications concerning the optimal vertical-level distributions for the WRF model (Ma et al., 2012, 2014; Shin et al., 2012; Zängl et al., 2008).

All the runs were performed using the following parameterizations:

- Radiative physics (for short-wave and long-wave radiation): the RRTMG scheme, which is the new version of the Rapid Radiative Transfer Model. This scheme is described by Iacono et al. (2008);

- Unresolved convective column physics (Cumulus parameterization): the Kain-Fritsch scheme, which is a 1-D entraining / detraining cloud model that includes downdrafts, and is more suited for mid-latitudes. This scheme is described by Kain (2004);

- Resolved cloud physics (Microphysics): the WRF Single-Moment 5-Class scheme, which is a model for the prognostic formulation of the phases of water vapor, cloud, ice, rain and snow. This scheme is described by (Hong et al., 2004).

The land-use categories were provided by the MODIS-based land-use data, with 20 categories at a 30 arc-sec resolution, which is suitable for the Noah land-surface physics model. This model has been developed through multi-institutional cooperation (Niu et al., 2011), with soil temperature and moisture resolved for four vertical soil layers, and, hence, is only applied for land-surface grid cells. For water surfaces, the SST was updated every 3-h using the CFSv2 dataset.

Test runs were performed with and without internal-domain nudging above the planetary boundary-layer (PBL), which is the boundary-layer height estimated by the PBL

scheme. The use of nudging for dynamics studies is often not recommended because it adds fake source terms. However, it was observed that the model was not able to represent the large-scale features after a few days of simulation without internal grid nudging; increasing the lateral boundary nudging was also insufficient. Therefore, the internal-domain nudging above the PBL was turned on, with nudging coefficients equal to 0.0003 s^{-1} set for the horizontal velocity components, temperature and specific humidity at a time interval of 6h. A negligible nudging influence on the surface-layer parameters is expected, since it only affects the region above the PBL height, which is expected to be far (about ten times) above the surface layer.

The numerical study of the present thesis aims to evaluate the performance of simulations within the atmospheric surface layer, especially the friction velocity, which is estimated at the first half-η level, and, therefore, below the first model level, and is not directly influenced by the source terms created by the nudging processes. In summary, the use of nudging guarantees that differences between the surface layer schemes are only due to the characteristics of the turbulence parameterizations of the different schemes, and not due to interactions between different atmospheric scales. Figures 3.13, 3.14, and 3.15 show that the use of nudging above the PBL enables the WRF model to simulate the synoptic scales represented by the mean sea-level pressure similarly to the CFSv2 model, even for a forecast length longer than 10 days.

The simulation outputs were requested for every 30-min interval, and the time period for each campaign is described in Table 3.2.

Table 3.2 - WRF simulation period for each campaign.

Campaign	Start date	End date
OP32	13 October 2013 at 12Z	21 October 2013 at 00Z
OP33	16 October 2014 at 12Z	24 October 2014 at 00Z
OP34	10 October 2014 at 06Z	20 October 2015 at 00Z

This work evaluates all atmospheric surface layer schemes available in WRF version 3.6.1, with the six experiments performed listed in Table 3.3.

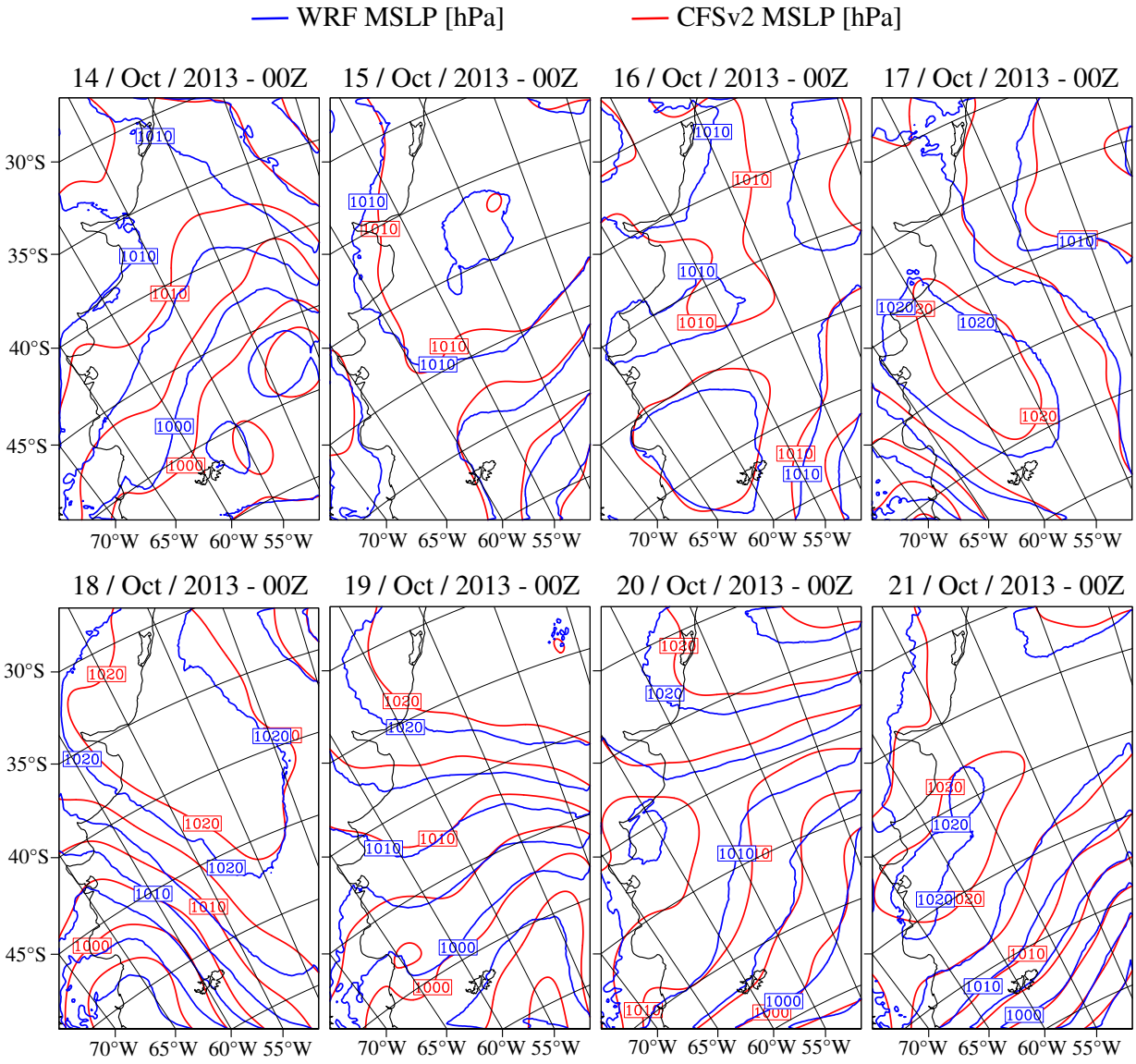

Figure 3.13: Comparison between the mean sea-level pressure [hPa] estimated by the WRF (blue lines) and CFSv2 (red lines) models at 00Z of each day of the OP32 campaign.

Table 3.3 - Planetary boundary-layer (PBL) and atmospheric surface layer (SL) schemes used for each experiment.

Experiment	PBL and SL schemes
Exp1	YSU/MM5
Exp2	MYJ/ETA
Exp3	QNSE
Exp4	MYNN2
Exp5	ACM2
Exp6	TEMF

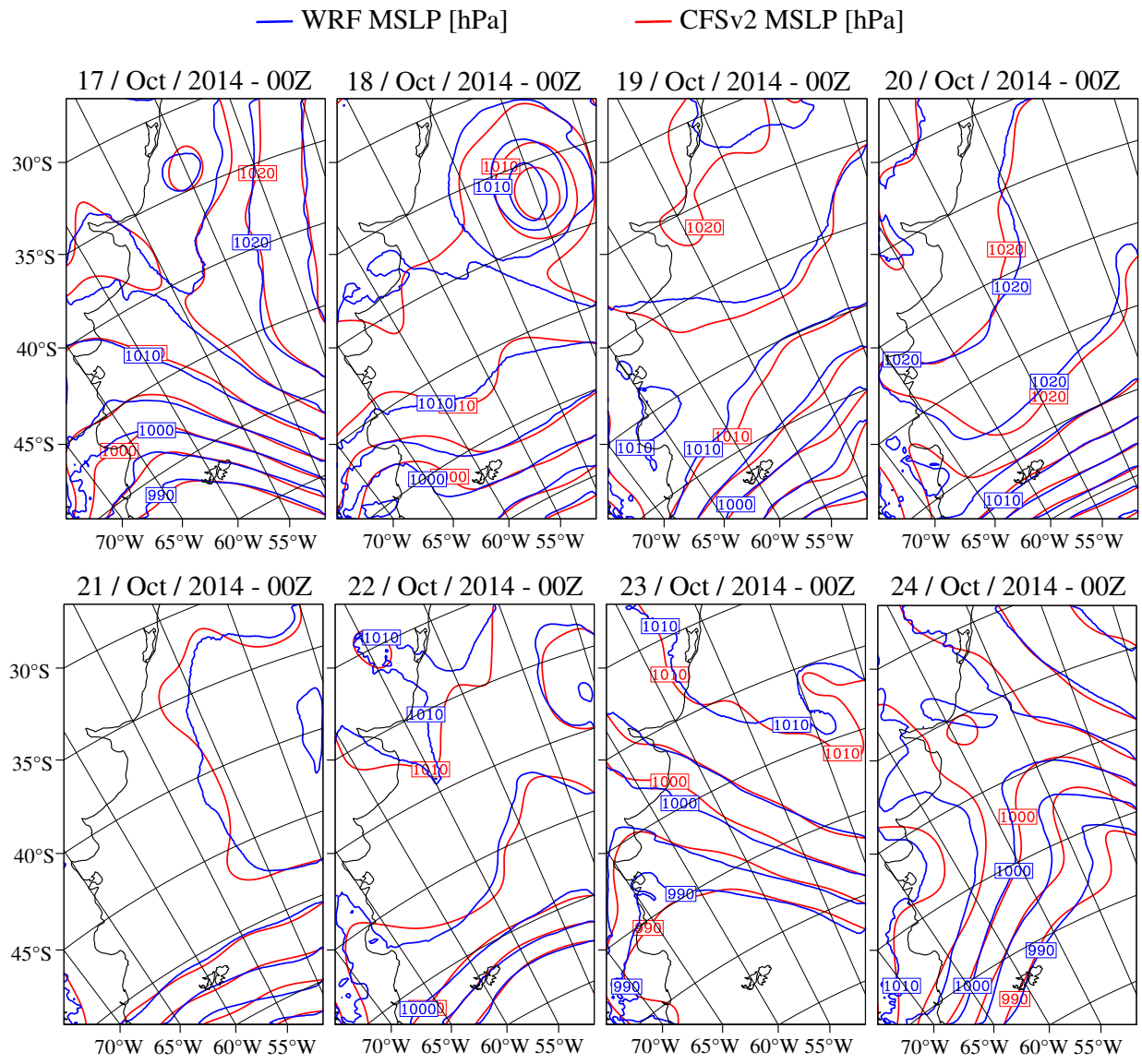

Figure 3.14: As for Fig. 3.13, but for the OP33 campaign.

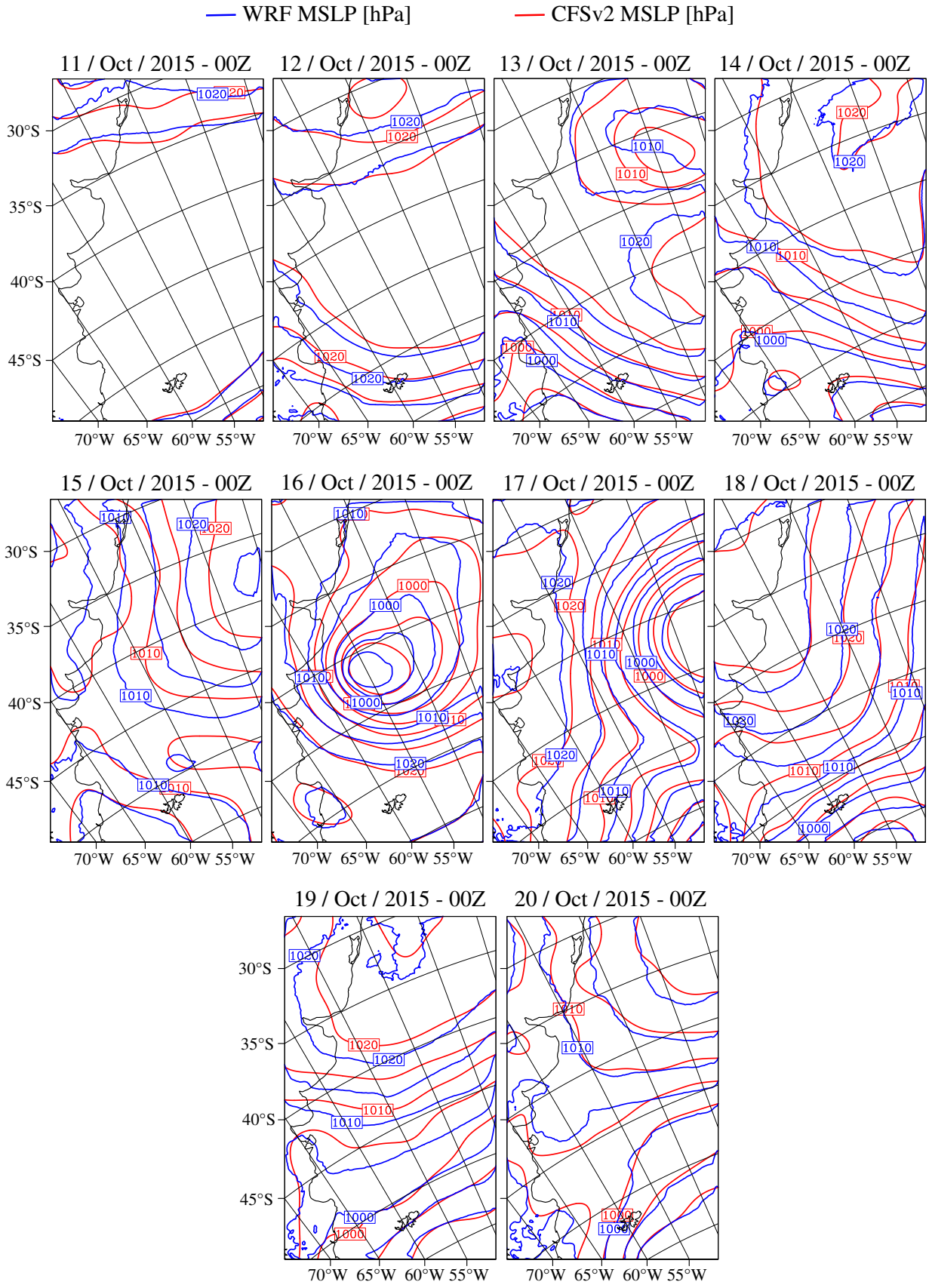

Figure 3.15: As for Fig. 3.13, but for the OP34 campaign.

Chapter 4

Results

This chapter presents the results and discussions for the momentum flux parameters and dimensionless dissipation and transport components of the TKE budget equation over the Southwestern Atlantic Ocean. The chapter is divided into two parts: the first is related to the in situ data, and the second is dedicated to the WRF simulations.

The results presented in the first part were submitted to the *Journal of Geophysical Research - Atmospheres*, with the co-authors L. P. Pezzi, M. Bakhoday Paskyabi, A. P. Oliveira, J. Reuder, R. B. Souza, and R. Camargo, under the title *The role of roughness and stability on the momentum flux in the Marine Atmospheric Surface Layer: a study on the Southwestern Atlantic Ocean.*

4.1 Analysis of the MASL turbulent parameters from observations

The scaling parameters u_* and θ_* were estimated using the eddy-covariance method. The validity of these estimates were evaluated by comparing the parameters $\frac{\sigma_w}{u_*}$ or $\frac{\sigma_\theta}{\theta_*}$ to the ζ, where σ is the standard deviation. The comparison presented in Fig. 4.1 shows considerable agreement with the often cited results from Wyngaard et al. (1971) for the convective regime, and from Pahlow et al. (2001) for the stable regime, which are expressed by Eq. (2.7) and 2.8, respectively. These comparisons are important to ensure that the measurements are located within the MASL and above the wave boundary-layer (Sjöblom and Smedman, 2004), where Monin-Obukhov Similarity theory is applicable and the logarithmic vertical profiles are only functions of stability.

Although the high H_s conditions are observed only during near-neutral conditions, the average of $\frac{\sigma_w}{u_*}$ when $\zeta < 0.05$ is 0.99 ± 0.13 for $H_s \geq 2.5$ m (Fig. 4.2), which is comparable

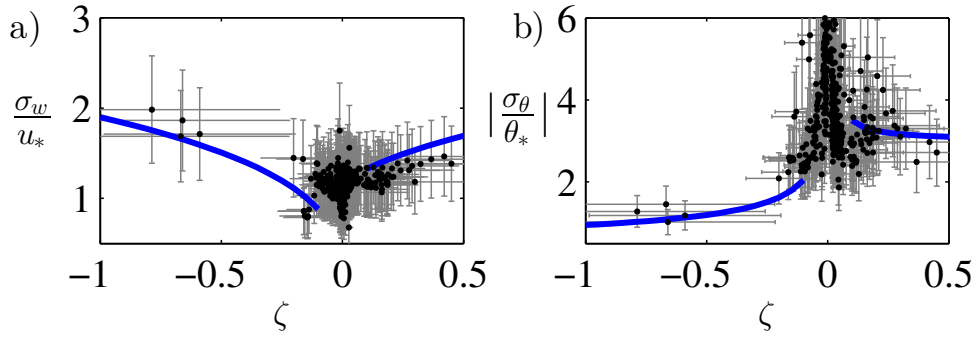

Figure 4.1: Normalized standard deviation for (*a*) the vertical velocity component and (*b*) the virtual potential temperature as a function of the stability parameter. The blue lines are the similarity expressions derived by Wyngaard et al. (1971) for the convective regime and by Pahlow et al. (2001) for the stable regime. The vertical axis in (*b*) is limited to a magnitude of six since $|\frac{\sigma_\theta}{\theta_*}| \to \infty$ in the neutral regime.

to 1.20 ± 0.09 observed for $H_s < 2.5$ m. These numbers are in agreement with the results from Wyngaard et al. (1971) and Pahlow et al. (2001).

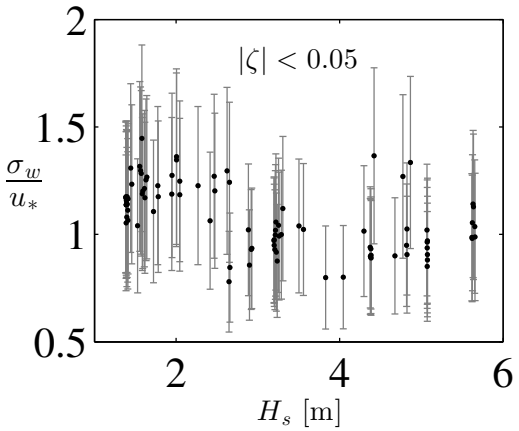

Figure 4.2: Normalized standard deviation of the vertical velocity component versus the significant wave height for the near-neutral regime ($|\zeta| < 0.05$).

The time series for the friction velocity during the INTERCONF cruises are presented in Fig. 4.3, together with the CFSv2 estimates for comparative purposes. Considering the inherent errors in the global model results (i.e bulk approximations, interpolation errors and data assimilation issues), the estimates of u_* are satisfactory, with $R^2 = 0.61$. The underestimation seen in parts of the CFSv2 data are interpreted as a potential underestimation of the modeled surface drag.

Considering the uncertainty, the results for the transport and dissipation terms of the

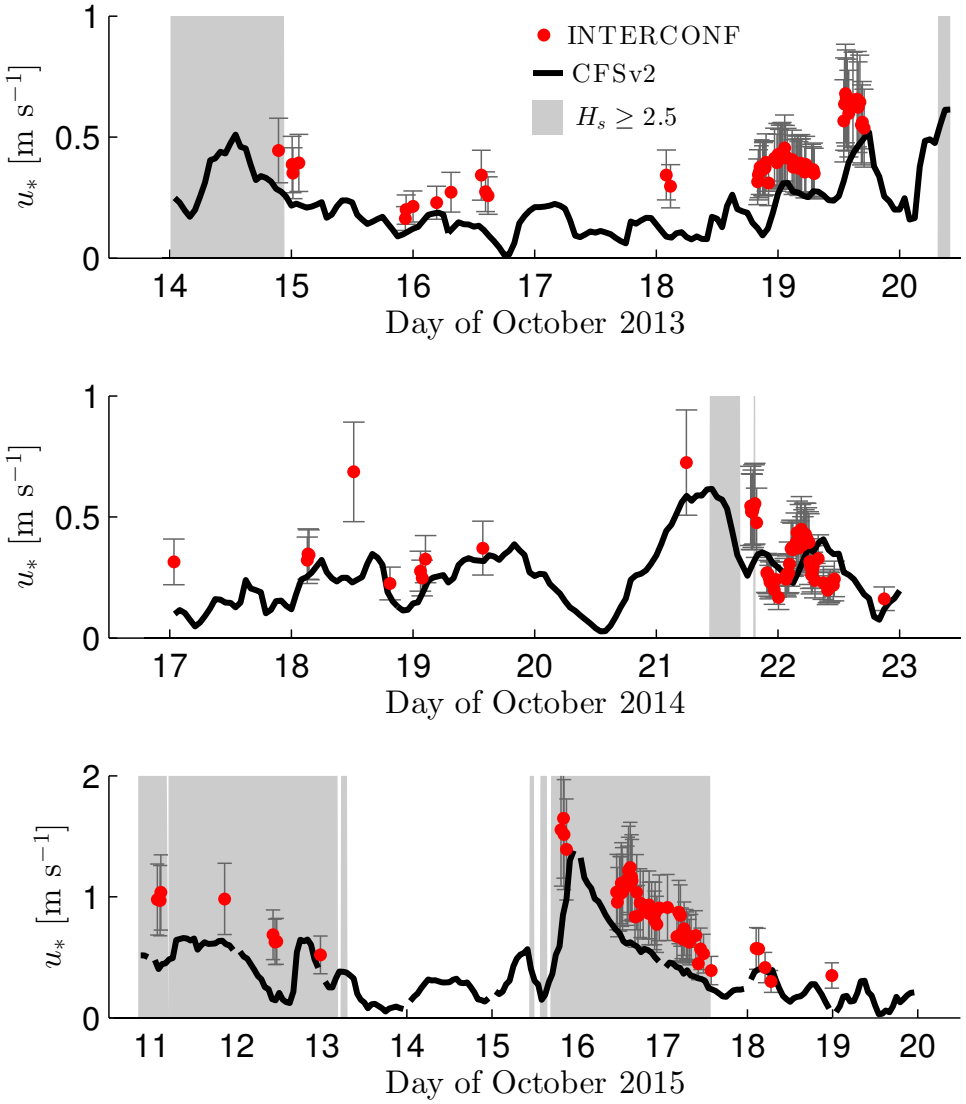

Figure 4.3: Comparison between the friction velocity [m s^{-1}] estimated for the INTERCONF dataset and from the re-analysis data of the Climate Forecast System version 2 model interpolated in time and space to the ship coordinates. The gray areas indicate the significant wave height above 2.5 m.

TKE budget equation are in agreement with the observations taken over a land surface by Hackerott et al. (2017). This is demonstrated in Fig. 4.4, where the magnitude of both dissipation and transport tends to increase as stability departs from the neutral regime. It is not possible, however, to determine the influence of wave conditions in all stability regimes, since all observations recorded with $H_s \geq 2.5$ m are associated with the near-neutral MASL. Within the near-neutral regime, however, no significant differences in $\Phi^{D,T}$ were observed between the two wave height regimes.

The magnitude of Φ^T was estimated as a residual term in Eq. (2.17), and, therefore, no

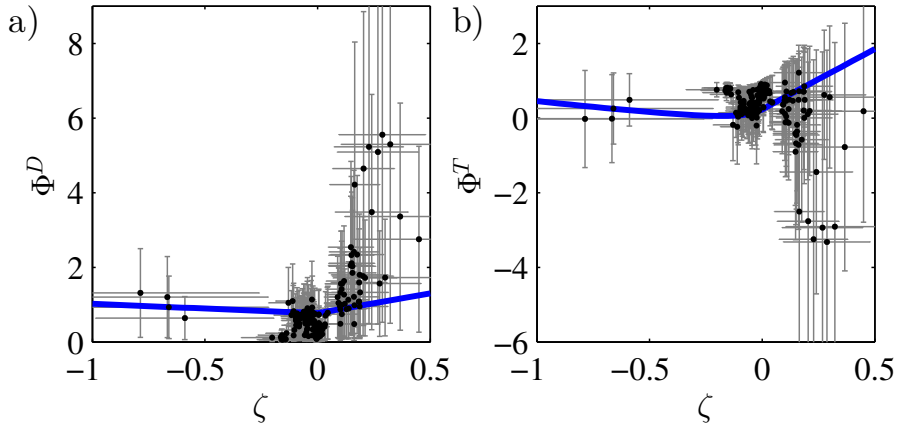

Figure 4.4: Dimensionless dissipation (a) and transport (b) terms of the TKE budget equation versus the Monin-Obukhov stability parameter. The blue lines are the expressions from Hackerott et al. (2017).

direct measurement was performed to estimate the pressure fluctuation in the atmospheric surface layer due to surface motion. Nevertheless, negative values of TKE transport observed in Fig. 4.4b indicate an upward TKE transport induced by momentum transferred from the surface to the MASL in the presence of waves. Recently, Kahma et al. (2016) showed measurements of wave-pressure correlations, indicating that swell is associated with upward momentum fluxes at the 99% confidence level. The INTERCONF dataset shows that this phenomenon occurs frequently under stable MASL conditions ($\zeta > 0$).

The high values of Φ^D in the stable regime compared with land-based measurements are also explained by the upward momentum flux delivered from the surface motion (waves). The TKE is increased by the presence of wave perturbations applied on the MASL, and, consequently, the dissipation rate of TKE also increases. Unfortunately, it is not possible to make further conclusions with regard to this hypothesis, since the TKE production term was not estimated directly, but calculated using the similarity functions of Högström (1996). This phenomenon is expected to occur more often during near-neutral and stable regimes (assuming the equivalent wind speed) when the turbulence is mainly produced by shear effects, and other sources of turbulence (i.e. surface motion) become more relevant. It is, however, difficult to measure the wave influence during the stable regime since non-stationarities and intermittent turbulence are usually more frequently observed, causing high scatter in the estimates of Φ^D (Hartogensis and Bruin, 2005; Nilsson et al., 2016; Hackerott et al., 2017).

The results for the drag coefficient are presented in Fig. 4.5, where C_{DN10} is compared with the neutral 10 m mean wind speed, with colors distinguishing different significant wave heights estimated by the WAVEWATCH III® model. To emphasize the trends, 2 m s^{-1} bin averages were calculated for H_s above (red) and below (blue) 2.5 m. Although the expression proposed by Garratt (1977) satisfies the INTERCONF dataset for smooth sea with a wind speed above 10 m s^{-1}, the drag coefficient must take into account more parameters in addition to the wind speed. In the specific case of the BMC, the strong current gradient affects the wave height since counter-wind currents considerably change the wave shape (Taylor and Yelland, 2001; Drennan and Shay, 2005; Kara et al., 2007).

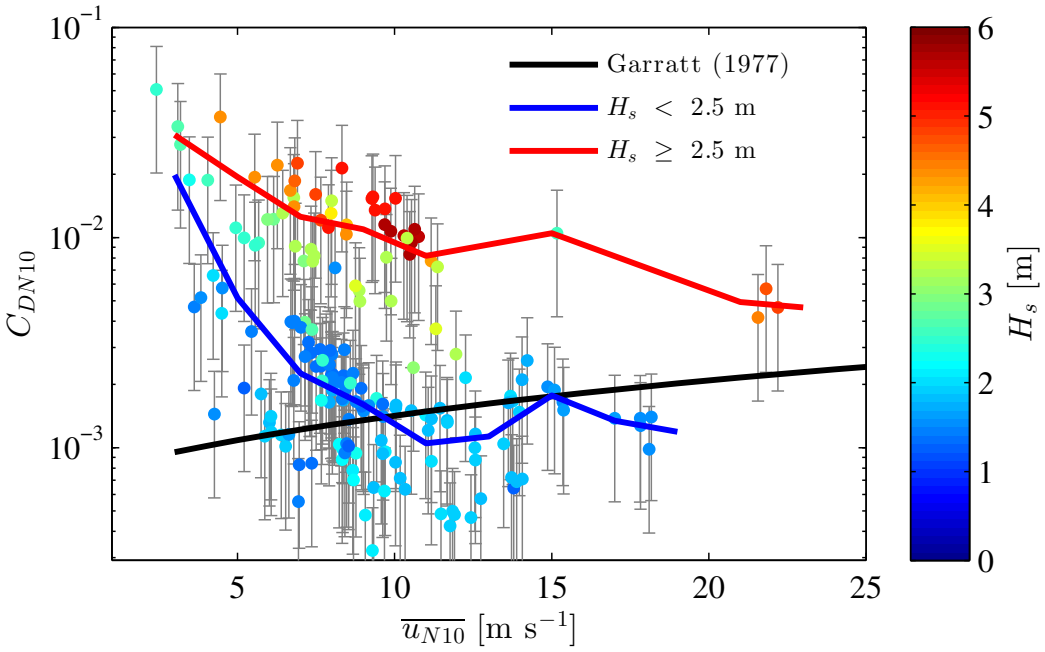

Figure 4.5: Drag coefficient versus neutral 10 m mean wind speed [m s^{-1}], with colors indicating the significant wave height [m]. The errorbars (gray) are estimated assuming a 30% error in the friction velocity propagating to the calculation of C_{DN10}. The black line is the expression proposed by Garratt (1977), and the blue and red lines are 2 m s^{-1} bin averages considering only waves lower and higher than 2.5 m, respectively.

The decrease in C_{DN10} with increasing wind speed is expected under the swell-dominated conditions (Yelland and Taylor, 1996; Donelan et al., 1997; Pan et al., 2005) at low wind-speed regimes (below 6 m s^{-1}). The INTERCONF dataset, however, indicated a negative trend for the drag coefficient up to 10 m s^{-1} for low waves, and a continuous decrease with increasing wind speed for high wave conditions. Similar observations were also reported by García-Nava et al. (2012), who suggested that the wind-sea, which is responsible for the

sea roughness for similar wave and wind directions, are damped by the presence of swell, resulting in the reduction of the total wind stress, even in moderate to high wind-speed conditions. This phenomenon is one hypothesis for the decrease of C_{DN10} with increasing wind speed, observed in the vicinity of the BMC, where intense swell events are frequently observed because of the high occurrence of extra-tropical cyclones and cyclogenisis activity (Hoskins and Hodges, 2005; Reboita et al., 2010). Unfortunately, we cannot make further conclusions regarding to the difference between the swell and wind-sea because of the lack of advanced measurements of detailed wave energy spectra during the INTERCONF cruises.

The high values of C_{DN10} compared with the bulk formulation in the range from 6 to 12 m s^{-1} may also be explained by the presence of counter-swell (Donelan et al., 1997). In these wind-speed regimes, the high values of the roughness Reynolds number ($Re_* = u_* z_0/\nu$, where $\nu = 1.5 \times 10^{-5}$ $m^2 s^{-1}$ is the kinematic viscosity of air) presented in Fig. 4.6 can be attributed to a counter-swell effect acting as roughness elements (García-Nava et al., 2009).

4.1.1 The wave-induced roughness layer

The results presented in the previous section showed that the wave height has an important influence on the friction velocity and, consequently, on the drag coefficient. According to Monin-Obukhov similarity theory, u_* determines the steepness of the logarithmic wind-speed profile (Eq. (3.10)) and, after considering the MASL stability, z_0 can be estimated. Large values of the aerodynamic roughness length (in the order of a few meters) over land surfaces, in particular over vegetation or urban canopies, are interpreted as a result of the effective roughness plus a displacement length, d. Analogously, waves over the ocean also act as roughness elements and the corresponding d can be interpreted as the depth of the wave-induced roughness layer.

Figure 4.7 shows z_0 estimated from Eq. (3.13) compared with the classical expression defined by Eq. (3.14). These results show a significant departure from the reference curve for the dataset with H_s above 2.5 m, indicating the presence of the wave-induced roughness layer, with d in the range between 0.1 and 1 m.

Since there was no direct wave measurement available during the experiments, it is not possible to assert more precise values or formulations regarding d. Nevertheless, the results

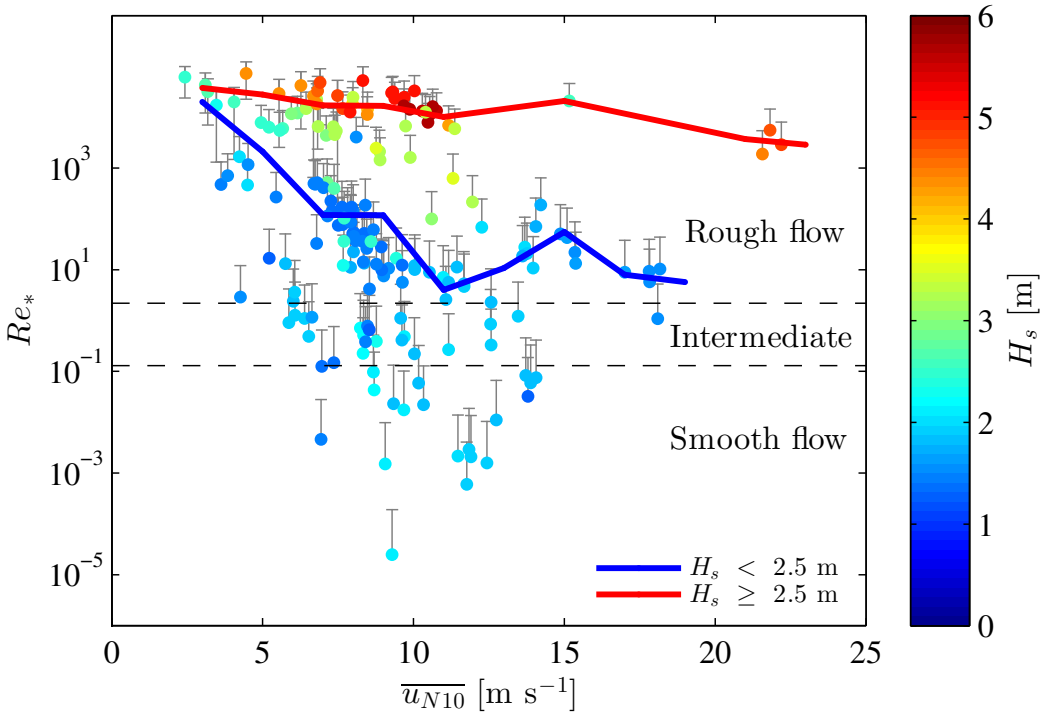

Figure 4.6: Roughness Reynolds number versus the neutral 10 m mean wind speed [m s^{-1}], with colors indicating the significant wave height [m]. The blue and red lines are 2 m s^{-1} bin averages considering only waves lower and higher than 2.5 m, respectively. Some of the errorbars are larger than the estimated value, and are displayed only above to avoid negative values in the logarithmic plot. Dashed lines represent the limits for rough, intermediate and smooth flow conditions, located at $Re_* = 0.13$ and $Re_* = 2.2$.

show the importance of accounting for a wave-induced roughness layer for momentum flux parameterizations. Conceptually, this work suggests extending the vertical structure of the Marine Atmospheric Boundary Layer, by including a wave-induced roughness layer with a thickness in the order of 0.1 to 1 m as schematically illustrated in Fig. 1.1, which is presented in the Introduction of this thesis (Chap. 1).

4.2 WRF parameterizations for the turbulent parameters of the MASL

The mesoscale model WRF was executed using six combinations of PBL and surface layer schemes. The results for the time series of the friction velocity are presented in Fig. 4.8, which is similar to Fig. 4.3, but includes all WRF experiments.

Although all surface layer schemes use Monin-Obukhov similarity theory to calculate the heat and momentum fluxes, and a similar methodology to estimate z_0, it is possible to observe subtle differences among the simulations. The differences in the friction velocity

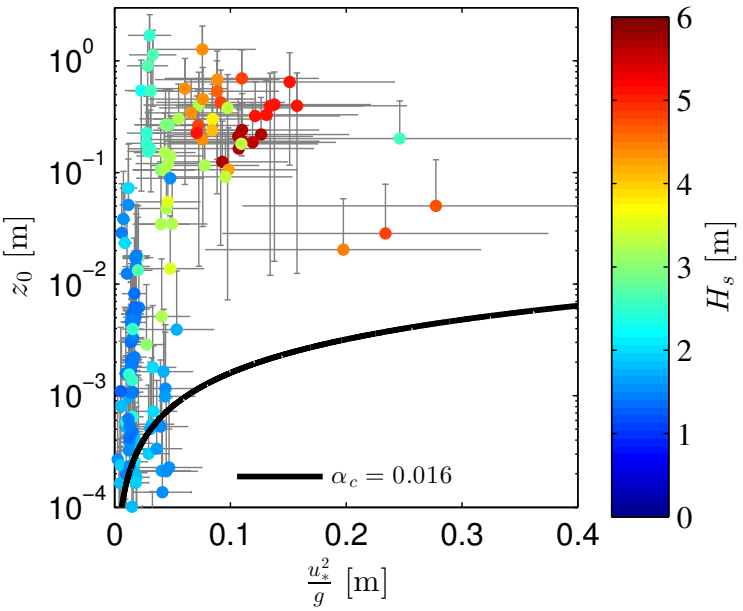

Figure 4.7: Scatterplot of the aerodynamic roughness length [m] versus the normalized squared friction velocity [m], with colors indicating the significant wave height [m]. The errorbars (gray) are estimated assuming an error of 30% in the friction velocity propagating to z_0 in Eq. (3.13) and $\frac{u_*^2}{g}$. The black line represents Eq. (3.14) with a Charnock constant equal to 0.016. For clarity, the plotted values are limited to $z_0 > 10^{-4}$ m and, therefore, 81 values below this limit are absent, all of them, however, with $\frac{u_*^2}{g} < 0.021$ m. Some of the vertical errorbars are larger than the estimated value and are displayed only above to avoid negative values in the logarithmic plot.

are, consequently, reflected in the time series of the 10 m wind speed, which is shown in Fig. 4.9.

The analysis of both time series (u_* and $\overline{u_{10}}$) suggests that the underestimation of u_* occurs mainly during high-wave conditions (gray areas), and, consequently, $\overline{u_{10}}$ is overestimated in this regime, since the increase in drag results the decrease in the 10 m wind speed. This bias, however, is not clearly observed for low-wave conditions ($H_s \leq 2.5$ m), where the simulations are closer to the observations, or at least not clearly biased, for both variables.

The biased tendency observed for u_* and $\overline{u_{10}}$ is evident in the scatterplot of simulations versus observations for the two wave regimes presented in Fig. 4.10. To avoid redundancy, only the results for the global model CFSv2 are shown. The bias results for all simulations, for both wave height regimes are listed in Table 4.1.

It is not possible to rank the schemes, since all behave similarly. However, Exp 3 and Exp 6 depart, although not consistently, from the others mainly during high-wave

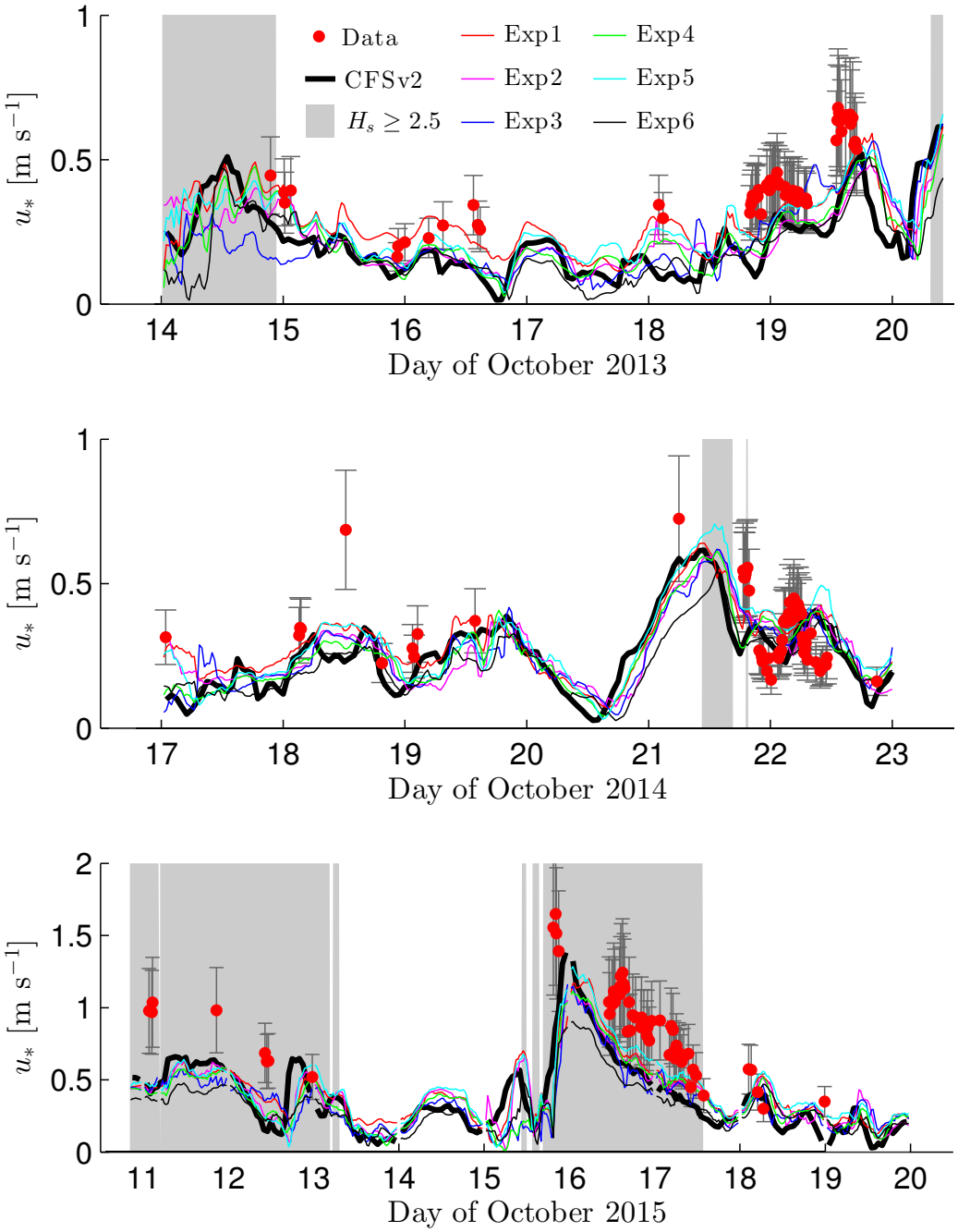

Figure 4.8: Time series of friction velocity estimated and simulated during the INTERCONF campaigns. The gray areas indicate a significant wave height above 2.5 m.

conditions, which may be merely a coincidence, since the models do not account for swell. In addition, the physics of these schemes are theoretically different in terms of the PBL parameterization, where the Exp 3 scheme (QNSE) is a non-local parameterization, while the Exp 6 scheme (TEMF) is a local 1.5-order TKE closure scheme. Another interesting observation is that the Exp 1 scheme, which is the non-local YSU PBL scheme with the

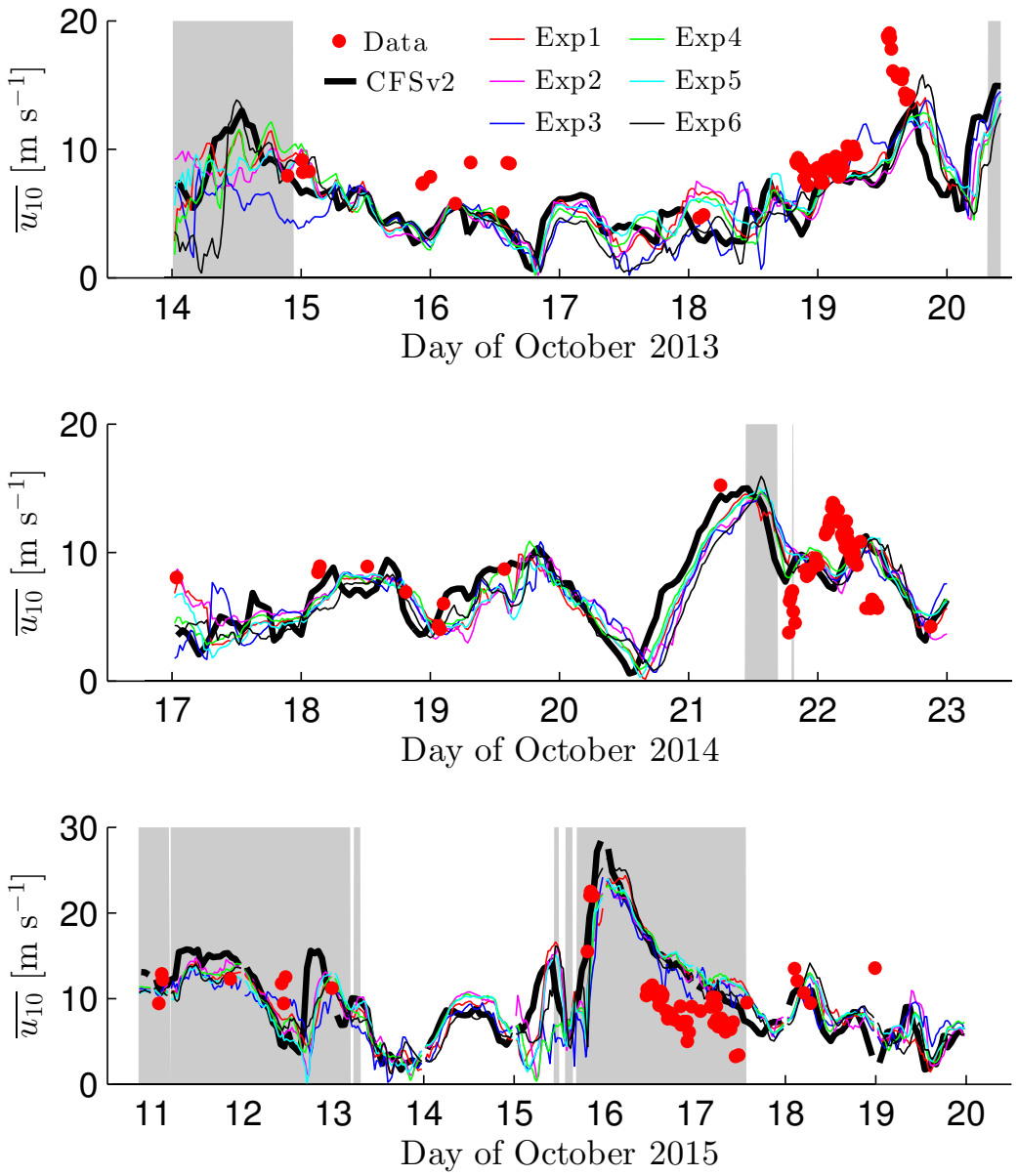

Figure 4.9: Time series of wind speed at 10 m estimated and simulated during the INTERCONF campaigns. The gray areas indicate a significant wave height above 2.5 m.

MM5 surface layer, shows better results for u_* only during the INTERCONF cruise of 2013, although there was no significant improvement for the 10 m wind speed.

The subtle differences among the experiments are probably more related to the latent and sensible heat fluxes rather than the momentum flux calculations since, as mentioned in Chap. 2, the main differences among the schemes are related to the parameterizations of thermal and moisture roughness lengths. The energy for the atmospheric motions is mainly provided by the surface heat (latent and sensible) fluxes, which modify the stability profile

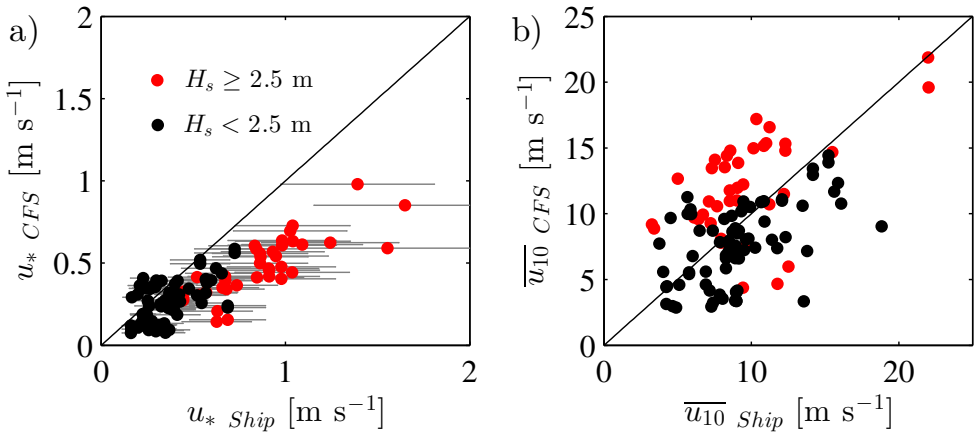

Figure 4.10: Scatterplots of (a) the friction velocity and (b) the wind speed at 10 m, estimated from the CFSv2 model versus the estimated ones from the ship measurements.

within the MASL. Therefore, differences in the calculations of θ_* and q_* lead to different results for u_*.

To correct the bias during high-wave conditions, the results presented in this work suggest the inclusion of a zero-plane displacement d in the order of 0.1 to 1 m in the formulation of z_0. This would increase the drag and, consequently, reduce the 10 m wind speed. The identification of high-wave regions, however, is a challenge without wave information from a coupled air-sea model.

Table 4.1 - Bias (average of simulated minus observed) of wind speed and friction velocity for two regimes of the significant wave height. All values are displayed in [m s^{-1}].

	$H_s > 2.5$ m	$H_s \leq 2.5$ m
$\overline{u_{10}}^{CFS}$	2.39	-1.45
u_*^{CFS}	-0.38	-0.10
$\overline{u_{10}}^{Exp1}$	3.37	-1.24
u_*^{Exp1}	-0.32	-0.03
$\overline{u_{10}}^{Exp2}$	2.87	-1.56
u_*^{Exp2}	-0.36	-0.08
$\overline{u_{10}}^{Exp3}$	1.92	-1.55
u_*^{Exp3}	-0.40	-0.08
$\overline{u_{10}}^{Exp4}$	3.25	-1.22
u_*^{Exp4}	-0.35	-0.07
$\overline{u_{10}}^{Exp5}$	3.26	-1.31
u_*^{Exp5}	-0.28	-0.03
$\overline{u_{10}}^{Exp6}$	2.41	-1.58
u_*^{Exp6}	-0.47	-0.11

Chapter 5

Conclusions and Perspectives

For the first time, in situ turbulence measurements collected on the Southwestern Atlantic Ocean, in the vicinity of the BMC region, were used to determine the influence of the ocean waves and atmospheric stability on the MASL. Here, the MASL momentum flux parameters were successfully estimated from three ship based experiments of the INTERCONF project. The effect of ship motion on the velocity data was satisfactory reduced and 187 20-min segments were finally selected after a rigorous quality-control procedure, which was first evaluated for the well-tested, land-based BLLAST dataset.

The momentum flux processes within the MASL were studied and characterized from the analysis of different terms of the TKE budget. It was observed that both the transport and dissipation terms of the TKE budget follow similar patterns found in studies over land surfaces, where both the transport and the dissipation terms increase as the stability departs from near-neutral conditions. Negative values of TKE transport were observed during the stable regime, which indicates an upward momentum flux induced by wave motion, increasing the production and dissipation of TKE. For the near-neutral and convective regimes, however, these terms showed less sensitivity to the waves.

One of the main results of this thesis is that the drag coefficient indicate different behaviors than previous studies. It shows a negative trend of C_{DN10} for a calm wind speed up to 10 m s^{-1}, considering $H_s < 2.5$ m, and a continuous decrease of the C_{DN10} with increasing wind speed for $H_s \geq 2.5$ m.

During high-waves sea conditions ($H_s \geq 2.5$ m), the analysis of z_0 indicated that the waves act like roughness elements by inducing a zero-plane displacement d in the order of 0.1 to 1 m, which is analogous to the canopy-layer height over land surfaces, and suggests the presence of a wave roughness layer within the MASL.

With respect to the model simulations, all current available surface-layer parameterizations within the WRF model (six experiments) were successfully tested, with the results showing a similar behavior, but the inability to correctly reproduce the vertical wind-speed profile within the MASL during rough-sea conditions, with significant underestimation of the friction velocity, and, as a consequence, overestimation of the 10 m wind speed. For future work, a modification of the formulation of the aerodynamic roughness length by including a zero-plane displacement term for rough sea states would be beneficial. However, a precise expression for this correction requires wave and current measurements, which were not available during the INTERCONF cruises.

In addition to the conclusions for the MASL, this work also clarified an interesting behavior of turbulence within a general atmospheric surface layer. For the theoretical study of the similarity theory and turbulent processes of the atmospheric surface layer, it was concluded that $\Phi^D_{\theta,q}(\zeta) \approx 0.4 + 0.2\zeta$ for the convective atmospheric surface layer. This scalar similarity implies that q_*, and c_* can be expressed as a function of their respective dissipation rates, N_θ and θ_*, as expressed by Eq. (2.25).

These findings are important for estimating H, LE, and the transfer coefficients related to the scaling parameters of θ and q. The influence of platform motion on the temperature and moisture measurements is still questionable, and the use of the inertial dissipation method as simplified by Eq. (2.25) is recommended. This may also be useful for studies where the displacement length is unknown or varies according to the wind direction, such as in urban areas, which, however, is a theme for future work.

Finally, I hope that the results presented here encourage new field campaigns over the BMC region. It is evident that the continuous sampling of this region, not only with atmospheric measurements, but also with in situ wave energy spectra estimates will enable the improvement of bulk formulations. Additionally, the selected dataset presented in this work should be further used to estimate the heat fluxes in the BMC region, which are also key components to cyclone development in the Southwestern Atlantic Ocean, which is one of the most dynamically active ocean regions (Chelton et al., 1990; Piola et al., 2000) and a very active atmospheric storm track region (Hoskins and Hodges, 2005; Reboita et al., 2010).

For further field campaigns, I highly suggest to include more micrometeorology instruments vertically distributed in the tower to allow direct measurements of the transport

and production terms of the TKE budget equation, and consequently better estimates of z_0. It would be also interesting to have direct wave measurements, to correlate the flux measurements to the wave height, the wave age, and the angle of wind relative to the wave direction.

Bibliography

Acevedo O. C., Pezzi L. P., Souza R. B., Anabor V., Degrazia G. A., Atmospheric boundary layer adjustment to the synoptic cycle at the Brazil-Malvinas Confluence, South Atlantic Ocean, Journal of Geophysical Research: Atmospheres, 2010, vol. 115, p. n/a

Andreas E. L., Mahrt L., Vickers D., A new drag relation for aerodynamically rough flow over the ocean, Journal of the Atmospheric Sciences, 2012, vol. 69, p. 2520

Angevine W. M., Jiang H., Mauritsen T., Performance of an eddy diffusivity-mass flux scheme for shallow cumulus boundary layers, Monthly Weather Review, 2010, vol. 138, p. 2895

Aubinet M., Timo V., Dario P., Eddy covariance. Springer Netherlands Dordrecht, 2012

Bakhoday Paskyabi M., Fer I., The influence of surface gravity waves on the injection of turbulence in the upper ocean, Nonlinear Processes in Geophysics, 2014, vol. 21, p. 713

Bakhoday Paskyabi M., Flügge M., Edson J. B., Reuder J., Wave-induced characteristics of atmospheric turbulence flux measurements, Energy Procedia, 2013, vol. 35, p. 102

Banks R. F., Tiana-Alsina J., Baldasano J. M., Rocadenbosch F., Papayannis A., Solomos S., Tzanis C. G., Sensitivity of boundary-layer variables to PBL schemes in the WRF model based on surface meteorological observations, lidar, and radiosondes during the HygrA-CD campaign, Atmospheric Research, 2016, vol. 176-177, p. 185

Belcher S. E., Hunt J. C. R., Turbulent flow over hills and waves, Annual Review of Fluid Mechanics, 1998, vol. 30, p. 507

Bloomfield P., Fourier analysis of time series 2 edn. John Wiley & Sons, Inc. Raleigh, North Carolina, USA, 2000

Bluteau C. E., Jones N. L., Ivey G. N., Estimating turbulent kinetic energy dissipation using the inertial subrange method in environmental flows, Limnology and Oceanography: Methods, 2011, vol. 9, p. 302

Buckley M. P., Veron F., Structure of the airflow above surface waves, Journal of Physical Oceanography, 2016, vol. 46, p. 1377

Camargo R., Todesco E., Pezzi L. P., de Souza R. B., Modulation mechanisms of marine atmospheric boundary layer at the Brazil-Malvinas Confluence region, Journal of Geophysical Research: Atmospheres, 2013, vol. 118, p. 6266

Chelton D. B., Schlax M. G., Witter D. L., Richman J. G., GEOSAT altimeter observations of the surface circulation of the Southern Ocean, Journal of Geophysical Research: Oceans, 1990, vol. 95, p. 17877

Cohen A. E., Cavallo S. M., Coniglio M. C., Brooks H. E., A review of planetary boundary layer parameterization schemes and their sensitivity in simulating Southeastern U.S. cold season severe weather environments, Weather and Forecasting, 2015, vol. 30, p. 591

de Arellano J. V. G., Duynkerke P. G., Atmospheric surface layer similarity theory applied to chemically reactive species, Journal of Geophysical Research, 1995, vol. 100, p. 1397

Donelan M. A., Curcic M., Chen S. S., Magnusson A. K., Modeling waves and wind stress, Journal of Geophysical Research: Oceans, 2012, vol. 117, p. n/a

Donelan M. A., Dobson F. W., Smith S. D., Anderson R. J., On the dependence of sea surface roughness on wave development, Journal of Physical Oceanography, 1993, vol. 23, p. 2143

Donelan M. A., Drennan W. M., Katsaros K. B., The air-sea momentum flux in conditions of wind sea and swell, Journal of Physical Oceanography, 1997, vol. 27, p. 2087

Drennan W. M., Kahma K. K., Donelan M. A., On momentum flux and velocity spectra over waves, Boundary-Layer Meteorology, 1999, vol. 92, p. 489

Drennan W. M., Shay L. K., On the variability of the fluxes of momentum and sensible heat, Boundary-Layer Meteorology, 2005, vol. 119, p. 81

Dudhia J., A history of mesoscale model development, Asia-Pacific Journal of Atmospheric Sciences, 2014, vol. 50, p. 121

Dupuis H., Taylor P. K., Weill A., Katsaros K., Inertial dissipation method applied to derive turbulent fluxes over the ocean during the Surface of the Ocean, Fluxes and Interactions with the Atmosphere/Atlantic Stratocumulus Transition Experiment (SOFIA/ASTEX) and Structure des Echanges Mer-Atmosphere, Journal of Geophysical Research, 1997, vol. 102, p. 21115

Dyer A. J., A review of flux-profile relationships, Boundary-Layer Meteorology, 1974, vol. 7, p. 363

Edson J. B., Hinton A. A., Prada K. E., Hare J. E., Fairall C. W., Direct covariance flux estimates from mobile platforms at sea*, Journal of Atmospheric and Oceanic Technology, 1998, vol. 15, p. 547

Edson J. B., Jampana V., Weller R. A., Bigorre S. P., Plueddemann A. J., Fairall C. W., Miller S. D., Mahrt L., Vickers D., Hersbach H., On the exchange of momentum over the open ocean, Journal of Physical Oceanography, 2013, vol. 43, p. 1589

Fairall C. W., Larsen S. E., Inertial-dissipation methods and turbulent fluxes at the air-ocean interface, Boundary-Layer Meteorology, 1986, vol. 34, p. 287

Fer I., Bakhoday Paskyabi M., Autonomous Ocean Turbulence Measurements Using Shear Probes on a Moored Instrument, Journal of Atmospheric and Oceanic Technology, 2014, vol. 31, p. 474

Flügge M., Paskyabi M. B., Reuder J., Edson J. B., Plueddemann A. J., Comparison of Direct Covariance Flux Measurements from an Offshore Tower and a Buoy, Journal of Atmospheric and Oceanic Technology, 2016, vol. 33, p. 873

Foken T., 50 years of the Monin-Obukhov similarity theory, Boundary-Layer Meteorology, 2006, vol. 119, p. 431

Foken T., Göockede M., Mauder M., Mahrt L., Amiro B., Munger W., , 2005 Post-field data quality control. Springer Netherlands Dordrecht pp 181–208

García-Nava H., Ocampo-Torres F. J., Hwang P. A., Osuna P., Reduction of wind stress due to swell at high wind conditions, Journal of Geophysical Research: Oceans, 2012, vol. 117, p. n/a

García-Nava H., Ocampo-Torres F. J., Osuna P., Donelan M. A., Wind stress in the presence of swell under moderate to strong wind conditions, Journal of Geophysical Research: Oceans, 2009, vol. 114, p. n/a

Garratt J. R., Review of drag coefficients over oceans and continents, Monthly Weather Review, 1977, vol. 105, p. 915

Garratt J. R., The atmospheric boundary layer. Cambridge University Press, 1994, 316

Gaube P., Chelton D. B., Samelson R. M., Schlax M. G., O'Neill L. W., Satellite observations of mesoscale eddy-induced Ekman pumping, Journal of Physical Oceanography, 2015, vol. 45, p. 104

Hackerott J. A., Bakhoday Paskyabi M., Reuder J., de Oliveira A. P., Kral S. T., Marques Filho E. P., Mesquita M. d. S., Camargo R., A surface-layer study of the transport and dissipation of turbulent kinetic energy and the variances of temperature, humidity and CO_2, Boundary-Layer Meteorology, 2017

Hartogensis O. K., Bruin H. A. R. D., Monin-Obukhov similarity functions of the structure parameter of temperature and turbulent kinetic energy dissipation rate in the stable boundary layer, Boundary-Layer Meteorology, 2005, vol. 116, p. 253

Hill R. J., Implications of Monin-Obukhov similarity theory for scalar quantities, Journal of the Atmospheric Sciences, 1989, vol. 46, p. 2236

Hill R. J., Algorithms for obtaining Atmospheric Surface-Layer fluxes from scintillation measurements, Journal of Atmospheric and Oceanic Technology, 1997, vol. 14, p. 456

Högström U., Review of some basic characteristics of the atmospheric surface layer, Boundary-Layer Meteorology, 1996, vol. 78, p. 215

Hong S.-Y., Dudhia J., Chen S.-H., A revised approach to ice microphysical processes for the bulk parameterization of clouds and precipitation, Monthly Weather Review, 2004, vol. 132, p. 103

Hong S.-Y., Noh Y., Dudhia J., A new vertical diffusion package with an explicit treatment of entrainment processes, Monthly Weather Review, 2006, vol. 134, p. 2318

Hoskins B. J., Hodges K. I., A new perspective on Southern Hemisphere storm tracks, Journal of Climate, 2005, vol. 18, p. 4108

Huang Y., Song J., Fan C., A motion correction on direct estimations of air-sea fluxes from a buoy, Acta Oceanologica Sinica, 2013, vol. 32, p. 63

Iacono M. J., Delamere J. S., Mlawer E. J., Shephard M. W., Clough S. A., Collins W. D., Radiative forcing by long-lived greenhouse gases: Calculations with the AER radiative transfer models, Journal of Geophysical Research: Atmospheres, 2008, vol. 113

Iwata T., Yoshikawa K., Higuchi Y., Yamashita T., Kato S., Ohtaki E., The spectral density technique for the determination of CO2 flux over the ocean, Boundary-Layer Meteorology, 2005, vol. 117, p. 511

Janjić Z. I., The step-mountain Eta coordinate model: Further developments of the convection, viscous sublayer, and turbulence closure schemes, Monthly Weather Review, 1994, vol. 122, p. 927

Jensen D. D., Nadeau D. F., Hoch S. W., Pardyjak E. R., Observations of near-surface heat-flux and temperature profiles through the early evening transition over contrasting surfaces, Boundary-Layer Meteorology, 2016, vol. 159, p. 567

Kader B. A., Determination of turbulent momentum and heat fluxes by spectral methods, Boundary-Layer Meteorology, 1992, vol. 61, p. 323

Kahma K. K., Donelan M. A., Drennan W. M., Terray E. A., Evidence of energy and momentum flux from swell to wind, Journal of Physical Oceanography, 2016, vol. 46, p. 2143

Kaimal J. C., Gaynor J. E., The Boulder Atmospheric Observatory, Journal of Applied Meteorology and Climatology, 1983, vol. 22, p. 863

Kaimal J. C. J., Wyngaard J. C. J., Izumi Y., Coté O. R., Cote O. R., Spectral characteristics of Surface-Layer turbulence, Quarterly Journal of the Royal Meteorological Society, 1972, vol. 98, p. 563

Kain J. S., The Kain-Fritsch convective parameterization: An update, Journal of Applied Meteorology, 2004, vol. 43, p. 170

Kara A. B., Metzger E. J., Bourassa M. A., Ocean current and wave effects on wind stress drag coefficient over the global ocean, Geophysical Research Letters, 2007, vol. 34, p. n/a

Katul G. G., Hsieh C.-I., A note on the flux-variance similarity relationships for heat and water vapour in the unstable atmospheric surface layer, Boundary-Layer Meteorology, 1999, vol. 90, p. 327

Katul G. G., Sempreviva A. M., Cava D., The temperature-humidity covariance in the marine surface layer: a one-dimensional analytical model, Boundary-Layer Meteorology, 2008, vol. 126, p. 263

Kirkil G., Mirocha J., Bou-Zeid E., Chow F. K., Kosović B., Implementation and evaluation of dynamic subfilter-scale stress models for large-eddy simulation using WRF, Monthly Weather Review, 2012, vol. 140, p. 266

Kolmogorov A. N., Dissipation of energy in locally isotropic turbulence, Doklady Akademii Nauk SSSR, 1941, vol. 32, p. 16

Large W. G., Pond S., Open ocean momentum flux measurements in moderate to strong winds, Journal of Physical Oceanography, 1981, vol. 11, p. 324

Lee X., Finnigan J., Paw U K. T., , 2005 Coordinate systems and flux bias error. Springer Netherlands Dordrecht pp 33–66

Li M., Babel W., Tanaka K., Foken T., Note on the application of planar-fit rotation for non-omnidirectional sonic anemometers, Atmospheric Measurement Techniques, 2013, vol. 6, p. 221

Lothon M., Lohou F., Pino D., Couvreux F., Pardyjak E. R., Reuder J., Vilà-Guerau de Arellano J., Durand P., Hartogensis O., Legain D., Augustin P., Gioli B., Lenschow

D. H., Faloona I., Yagüe C., Alexander D. C., Angevine W. M., Bargain E., Barrié J., Bazile E., et al., The BLLAST field experiment: Boundary-Layer Late Afternoon and Sunset Turbulence, Atmospheric Chemistry and Physics, 2014, vol. 14, p. 10931

Ma Z., Fei J., Huang X., Cheng X., Sensitivity of tropical cyclone intensity and structure to vertical resolution in WRF, Asia-Pacific Journal of Atmospheric Sciences, 2012, vol. 48, p. 67

Ma Z., Fei J., Huang X., Cheng X., Impacts of the lowest model level height on tropical cyclone intensity and structure, Advances in Atmospheric Sciences, 2014, vol. 31, p. 421

Mendonça L. F., Souza R. B., Aseff C. R. C., Pezzi L. P., Möller O. O., Alves R. C. M., Regional modeling of the water masses and circulation annual variability at the Southern Brazilian Continental Shelf, Journal of Geophysical Research: Oceans, 2017, vol. 122, p. 1232

Miller S. D., Hristov T. S., Edson J. B., Friehe C. A., Platform motion effects on measurements of turbulence and air-sea exchange over the open ocean, Journal of Atmospheric and Oceanic Technology, 2008, vol. 25, p. 1683

Moeng C.-H., Dudhia J., Klemp J., Sullivan P., Examining two-way grid nesting for large eddy simulation of the PBL using the WRF model, Monthly Weather Review, 2007, vol. 135, p. 2295

Nakanishi M., Niino H., An improved Mellor-Yamada Level-3 model: its numerical stability and application to a regional prediction of advection fog, Boundary-Layer Meteorology, 2006, vol. 119, p. 397

Nilsson E., Lothon M., Lohou F., Pardyjak E., Hartogensis O., Darbieu C., Turbulence kinetic energy budget during the afternoon transition - Part 2: A simple TKE model, Atmospheric Chemistry and Physics, 2016, vol. 15, p. 29807

Niu G.-Y., Yang Z.-L., Mitchell K. E., Chen F., Ek M. B., Barlage M., Kumar A., Manning K., Niyogi D., Rosero E., Tewari M., Xia Y., The community Noah land surface model with multiparameterization options (Noah-MP): 1. Model description and evaluation with local-scale measurements, Journal of Geophysical Research: Atmospheres, 2011, vol. 116

Ohtaki E., On the similarity in atmospheric fluctuations of carbon dioxide, water vapor and temperature over vegetated fields, Boundary-Layer Meteorology, 1985, vol. 32, p. 25

O'Neill L. W., Chelton D. B., Esbensen S. K., The effects of SST-induced surface wind speed and direction gradients on midlatitude surface vorticity and divergence, Journal of Climate, 2010, vol. 23, p. 255

Pahlow M., Parlange M. B., Porté-Agel F., On Monin-Obukhov similarity in the stable Atmospheric Boundary Layer, Boundary-Layer Meteorology, 2001, vol. 99, p. 225

Pan J., Wang D. W., Hwang P. A., A study of wave effects on wind stress over the ocean in a fetch-limited case, Journal of Geophysical Research: Oceans, 2005, vol. 110, p. n/a

Pezzi L. P., de Souza R. B., Acevedo O., Wainer I., Mata M. M., Garcia C. A. E., Camargo R., Multiyear measurements of the oceanic and atmospheric boundary layers at the Brazil-Malvinas confluence region, Journal of Geophysical Research: Atmospheres, 2009, vol. 114, p. n/a

Pezzi L. P., Souza R. B., Dourado M. S., Garcia C. A. E., Mata M. M., Silva-Dias M. A. F., Ocean-atmosphere in situ observations at the Brazil-Malvinas Confluence region, Geophysical Research Letters, 2005, vol. 32, p. n/a

Pezzi L. P., Souza R. B., Farias P. C., Acevedo O., Miller A. J., Air-sea interaction at the Southern Brazilian Continental Shelf: In situ observations, Journal of Geophysical Research: Oceans, 2016, vol. 121, p. 6671

Piola A. R., Campos E. J. D., Möller O. O., Charo M., Martinez C., Subtropical shelf front off eastern South America, Journal of Geophysical Research: Oceans, 2000, vol. 105, p. 6565

Pleim J. E., A combined local and nonlocal closure model for the atmospheric boundary layer. Part I: model description and testing, Journal of Applied Meteorology and Climatology, 2007, vol. 46, p. 1383

Prytherch J., Yelland M. J., Brooks I. M., Tupman D. J., Pascal R. W., Moat B. I., Norris S. J., Motion-correlated flow distortion and wave-induced biases in air-sea flux measurements from ships, Atmospheric Chemistry and Physics, 2015, vol. 15, p. 10619

Rai R. K., Berg L. K., Kosović B., Mirocha J. D., Pekour M. S., Shaw W. J., Comparison of measured and numerically simulated turbulence statistics in a convective boundary layer over complex terrain, Boundary-Layer Meteorology, 2017, vol. 163, p. 69

Rannik Ü., On the surface layer similarity at a complex forest site, Journal of Geophysical Research, 1998, vol. 103, p. 8685

Rannik U., Peltola O., Mammarella I., Random uncertainties of flux measurements by the eddy covariance technique, Atmospheric Measurement Techniques, 2016, vol. 9, p. 5163

Reboita M. S., da Rocha R. P., Ambrizzi T., Sugahara S., South Atlantic Ocean cyclogenesis climatology simulated by regional climate model (RegCM3), Climate Dynamics, 2010, vol. 35, p. 1331

Ruppert J., Thomas C., Foken T., Scalar similarity for relaxed eddy accumulation methods, Boundary-Layer Meteorology, 2006, vol. 120, p. 39

Saha S., Moorthi S., Wu X., Wang J., Nadiga S., Tripp P., Behringer D., Hou Y.-T., ya Chuang H., Iredell M., Ek M., Meng J., Yang R., na Mendez M. P., van den Dool H., Zhang Q., Wang W., Chen M., Becker E., The NCEP Climate Forecast System Version 2, Journal of Climate, 2014, vol. 27, p. 2185

Shin H. H., Hong S.-Y., Dudhia J., Impacts of the lowest model level height on the performance of planetary boundary layer parameterizations, Monthly Weather Review, 2012, vol. 140, p. 664

Sjöblom A., Smedman A.-S., Vertical Structure in the Marine Atmospheric Boundary Layer and its Implication for the Inertial Dissipation Method, Boundary-Layer Meteorology, 2003, vol. 109, p. 1

Sjöblom A., Smedman A.-S., Comparison Between Eddy-Correlation and Inertial Dissipation Methods in the Marine Atmospheric Surface Layer, Boundary-Layer Meteorology, 2004, vol. 110, p. 141

Skamarock W. C., Klemp J. B., Dudhia J., Gill D. O., Barker D., Duda M. G., Huang X., Wang W., Powers J. G., A Description of the Advanced Research WRF Version 3. NCAR Tech. Note NCAR/TN-475+STR, 2008

Small R., deSzoeke S., Xie S., O'Neill L., Seo H., Song Q., Cornillon P., Spall M., Minobe S., Air-sea interaction over ocean fronts and eddies, Dynamics of Atmospheres and Oceans, 2008, vol. 45, p. 274

Sorbjan Z., Structure of the Atmospheric Boundary Layer. Prentice Hall advanced reference series: Physical and life sciences, Prentice Hall, 1989

Spall M. A., Midlatitude wind stress-sea surface temperature coupling in the vicinity of oceanic fronts, Journal of Climate, 2007, vol. 20, p. 3785

Stull R. B., An introduction to boundary layer meteorology. vol. 13, Springer Netherlands, 1988, 666

Sukoriansky S., Galperin B., Perov V., Application of a new spectral theory of stably stratified turbulence to the atmospheric boundary layer over sea ice, Boundary-Layer Meteorology, 2005, vol. 117, p. 231

Sun J., French J. R., Air-sea interactions in light of new understanding of air-land interactions, Journal of the Atmospheric Sciences, 2016, vol. 73, p. 3931

Talbot C., Bou-Zeid E., Smith J., Nested mesoscale large-eddy simulations with WRF: performance in real test cases, Journal of Hydrometeorology, 2012, vol. 13, p. 1421

Taylor P. K., Yelland M. J., The dependence of sea surface roughness on the height and steepness of the waves, Journal of Physical Oceanography, 2001, vol. 31, p. 572

van de Boer A., Moene A. F., Graf A., Schüttemeyer D., Simmer C., Detection of entrainment influences on Surface-Layer measurements and extension of Monin-Obukhov Similarity Theory, Boundary-Layer Meteorology, 2014, vol. 152, p. 19

Warner J. C., Armstrong B., He R., Zambon J. B., Development of a Coupled Ocean-Atmosphere-Wave-Sediment Transport (COAWST) modeling system, Ocean Modelling, 2010, vol. 35, p. 230

Williams C. A., Scanlon T. M., Albertson J. D., Influence of surface heterogeneity on scalar dissimilarity in the roughness sublayer, Boundary-Layer Meteorology, 2007, vol. 122, p. 149

Willis G. E., Deardorff J. W., On the use of Taylor's translation hypothesis for diffusion in the mixed layer, Quarterly Journal of the Royal Meteorological Society, 1976, vol. 102, p. 817

Wyngaard J. C., Coté O. R., Izumi Y., Local free convection, similarity, and the budgets of shear stress and heat flux, Journal of the Atmospheric Sciences, 1971, vol. 28, p. 1171

Wyszogrodzki A. A., Miao S., Chen F., Evaluation of the coupling between mesoscale-WRF and LES-EULAG models for simulating fine-scale urban dispersion, Atmospheric Research, 2012, vol. 118, p. 324

Xie S., Ghaisas N., Archer C. L., Sensitivity issues in finite-difference large-eddy simulations of the atmospheric boundary layer with dynamic subgrid-scale models, Boundary-Layer Meteorology, 2015, vol. 157, p. 421

Yelland M., Taylor P. K., Wind stress measurements from the open ocean, Journal of Physical Oceanography, 1996, vol. 26, p. 541

Zängl G., Gohm A., Obleitner F., The impact of the PBL scheme and the vertical distribution of model layers on simulations of Alpine foehn, Meteorology and Atmospheric Physics, 2008, vol. 99, p. 105